フェムト秒ポンプ・プローブ法による半導体の光励起状態のダイナミクスの研究

著者	舛本 泰章
year	1993-03
その他のタイトル	Dynamical Study of Photoexcited States in Semiconductors by Means of Femtosecond Pump-and-Probe Spectroscopy
URL	http://hdl.handle.net/2241/117060

フェムト秒ポンプ・プローブ法による
半導体の光励起状態のダイナミクスの研究

(研究課題番号　03402007)

平成4年度科学研究費補助金(一般研究(A))
研 究 成 果 報 告 書

平 成 5 年 3 月

研究代表者　舛 本 泰 章
(筑波大学物理学系教授)

フェムト秒ポンプ・プローブ法による半導体の光励起状態のダイナミクスの研究

（研究課題番号　03402007）

平成４年度科学研究費補助金（一般研究（Ａ））

研 究 成 果 報 告 書

平 成 5 年 3 月

研究代表者　　舛 本 泰 章

（筑波大学物理学系教授）

平成３年度科学研究費補助金（一般研究Ａ）

フェムト秒ポンプ・プローブ法による半導体の光励起状態のダイナミクスの研究

（研究課題番号　03402007）

研究組織

研究代表者　　舛本泰章　（筑波大学物理学系教授）

研究分担者　　三品具文　（筑波大学物理学系助手）

研究経費

平成３年度	１５，６００千円
平成４年度	１０，３００千円
計	２５，９００千円

≪はじめに≫

フェムト秒分光は、極めて安定なフェムト秒高出力光パルスが数kHzから数百kHzの高繰り返しで生成できる再生増幅器を含むＴｉ：サファイアレーザーシステムの開発により、新たな第４世代を迎えようとしている。本科学研究費補助金で推進された半導体のフェムト秒分光は、 第３世代の色素レーザーシステムによって行われたものであるが、
レーザー光パルスそのものに違いがありようもなく、固体、特に半導体の光励起状態の超高速ダイナミクスの解明に威力を発揮してきた。

主要なフェムト秒分光の研究対象として取り上げてきたのは、ＣｄＳｅ結晶薄膜を対象としたバンド間励起により高く強く励起された高密度電子・正孔系の非平衡分布とその緩和、タイプII型ＡｌGaＡｓ-ＡｌＡｓ多重量子井戸を対象とした空間分離した電子・正孔系のダイナミクス、スピンダイナミクス、また、BiI_3を対象としたコヒーレントフォノンの生成とその観測である。これらの研究を進めてくる上で強く感じてきたことは、フェムト秒分光は１０Ｈｚ程度の低繰り返しポンプ・プローブ法ではもはや勝負できなくなったという事である。 従って研究成果も初期のＣｄＳｅ薄膜の研究を除いては、数kHz～数ＭHzの高繰り返しフェムト秒レーザーが活躍してきた。また、この間米国アリゾナ大学光科学センターとの共同研究（科学研究費「国際学術研究」によるサポート）が有効であった。

一方、材料科学の面に目を転じると、半導体はナノメートル微細構造の研究が年を追って研究が盛んになっている。この線に沿った研究としてＣｕＣｌ，Ｇｅ，Ｓｉ，ＡｇＢｒのナノメートル微結晶の光物性研究を推進してきた。またII－VI族量子井戸構造の研究も行ってきた。フェムト秒分光の対象となりにくかったこれらの新材料も、基礎的な分光研究で得られた知見の上にやがてフェムト秒分光の新しい対象になっていくであろう。

この科学研究費補助金研究成果報告書は、私の研究グループのここ２年間の成果を報告し、現時点までの成果の反芻を行う事により今後の発展を期す為にまとめたものである。引き続き第４世代のフェムト秒分光により新現象の発見や解明をめざす決意である。

発 表 論 文 リ ス ト

1．原著論文

<CdSe>

1) Y.Masumoto and F.Sasaki:
"Intraband Energy Relaxation of Hot Carriers in CdSe"
J. Lumin. 48 & 49, 189 (1991).

2) F.Sasaki, T.Mishina, Y.Masumoto, B.Fluegel, K.Meissner and N.Peyghambarian:
"Nonequilibrium Distribution of Hot Carriers in a CdSe Thin Film"
Semicond. Sci. Technol. 7, B160 (1992); Proc. 7th Int. Conf. on Hot Carriers in Semiconductors.

3) Y.Masumoto, B.Fluegel, K.Meissner, S.W.Koch, R.Binder, A.Paul and N.Peyghambarian:
"Band Gap Renormalization and Optical Gain Formation in Highly Excited CdSe"
J. Crystal Growth 117, 732 (1992); Proc. 5th Int. Conf. on II-VI Compounds, (Tamano, 1991).//INVITED PAPER//

4) F.Sasaki, T.Mishina, Y.Masumoto, B.Fluegel, K.Meissner and N.Peyghambarian:
"Femtosecond Optical Nonlinearities under the Resonant Excitation of Excitons in CdSe"
J. Crystal Growth 117, 768 (1992); Proc. 5th Int. Conf. on II-VI Compounds, (Tamano, 1991).

5) F.Sasaki, T.Mishina and Y.Masumoto:
"Ultrafast Pump-and-Probe Spectroscopy in CdSe: Hot Carrier and Exciton Dynamics"
Phys. Rev. B 46, Sep.15 (1992).

6) B.D.Fluegel, A.Paul, K.Meissner, R.Binder, S.W.Koch, N.Peyghambarian, F.Sasaki, T.Mishina and Y.Masumoto:
"Experimental and Theoretical Investigation of Femtosecond Carrier Relaxation in CdSe"
Solid State Commun 83, 17 (1992).

<AlGaAs-AlAs>

7) T.Mishina and Y.Masumoto:
"Exciton-Hole Collision in Staggered Type-II $Al_{0.34}Ga_{0.66}As$/AlAs Multiple Quantum Wells"
Phys. Rev. B 44, 5664 (1991).

8) Y.Masumoto, T.Mishina and F.Sasaki:
"Dynamical Aspects of Interlayer Charge Transfer in Type II AlGaAs-AlAs Multiple-Quantum-Well Structures"
in "Optical Properties of Solids" ed. by K.C. Lee, P.M. Hui and T. Kushida (World Scientific, 1991) p.16-p.56: Proc. Taiwan-Japan Workshop on Solid State Optical Spectroscopy, (Dec. 1990, Chung-li).

9) T.Mishina, F.Sasaki and Y.Masumoto:
"Ultrafast Optical Nonlinearities in Type-II AlGaAs/AlAs Multiple Quantum-Well-Structures and Their Device Applicability"
Surf. Science 267, 634 (1992).

10) T.Mishina and Y.Masumoto:
"Picosecond Repetitive Optical Switching Using Type II Multiple Quantum Well Structures"
Jap. J. Appl. Phys. 31, L343 (1992).

11) T.Kawazoe, Y.Masumoto and T.Mishina:

"Spin Relaxation Process of Holes in Type II $Al_{0.34}Ga_{0.66}As$/AlAs Multiple Quantum Wells"
Phys. Rev. B47, April 15 (1993).

<BiI_3>

12) T.Mishina, Y.Masumoto, B.Fluegel, K.Meissner and N.Peyghambarian:
"Observation of Coherent Optical Phonons in BiI_3"
Phys. Rev. B46, 4229 (1992).

<II-VI semiconductor superlattices>

13) A.Yamamoto, Y.Yamada and Y.Masumoto:
"Biaxial Splitting of Optical Phonon Modes in ZnSe-ZnS Strained-Layer Superlattices"
Appl. Phys. Lett. 58, 2135 (1991).
14) Y.Yamada, Y.Masumoto, T.Taguchi and K.Takemura:
"Type Conversion under Hydrostatic Pressure in ZnSe-ZnS Strained-Layer Superlattices"
Phys. Rev. B 44, 1801 (1991).
15) Y.Yamada, Y.Masumoto and T.Taguchi:
"Hydrostatic Pressure Dependence of Two-Dimensional Exciton Luminescence in ZnSe/ZnS Strained-Layer Superlattices"
Surf. Science 267, 129 (1992).
16) Y.Yamada, Y.Masumoto and T.Taguchi:
"Hydrostatic-Pressure-Induced Type I - Type II Conversion in ZnSe-ZnS Strained-Layer Superlattices"
J. Crystal Growth 117, 484 (1992); Proc. 5th Int. Conf. on II-VI Compounds, (Tamano, 1991).
17) A.Yamamoto, Y.Yamada and Y.Masumoto:
"New Characterization Method of Biaxial Stress by Raman Scattering: Demonstration in ZnSe-ZnS Strained-Layer Superlattices"
J. Crystal Growth 117, 488 (1992); Proc. 5th Int. Conf. on II-VI Compounds, (Tamano, 1991).
18) Y.Kanemitsu, A.Yamamoto, Y.Masumoto, H.Nabeta, S.Yamaga, A.Yoshikawa, K.Yamanaka, Y.Nagata and T.Koda:
"Residual Strains and Disorder in ZnSSe Epitaxial Films on GaAs"
J. Crystal Growth 117, 316 (1992); Proc. 5th Int. Conf. on II-VI Compounds, (Tamano, 1991).
19) Y.Kanemitsu, A.Yamamoto, H.Matsue, Y.Masumoto, S.Yamaga and A.Yoshikawa:
"Raman Study of Disorder and Strain in Epitaxial ZnS_xSe_{1-x} Films on a GaAs Substrate"
Appl. Phys. Lett. 60, 1330 (1992).
20) Y.Yamada, Y.Masumoto, J.T.Mullins and T.Taguchi:
"Ultraviolet Stimulated Emission and Optical Gain Spectra in $Cd_xZn_{1-x}S$-ZnS Strained-Layer Superlattices"
Appl. Phys. Lett. 61, 2190 (1992).
21) A.Yamamoto, Y.Kanemitsu, Y.Masumoto, S.Yamaga and A.Yoshikawa:
"Higher Order Zone-Folded Modes in ZnSe-ZnS Strained-Layer Superlattices"
Appl. Phys. Lett. 61, 1700 (1992).

<CuCl nanocrystals>

22) Y.Masumoto, T.Wamura and T.Kawamura:
"Anomalous Change of Extinction Spectra of CuCl Microcrystals"
Appl. Phys. Lett. 58, 2270 (1991).
23) Y.Masumoto, T.Wamura and T.Kawamura:
"Size Selective Nonlinear Optical Spectroscopy of Excitons in CuCl Quantum Dots"
Surf. Science 267, 315 (1992).
24) T.Wamura, Y.Masumoto and T.Kawamura:
"Size-Dependent Homogeneous Linewidth of Z_3 Exciton Absorption Spectra in CuCl Microcrystals"
Appl. Phys. Lett. 59, 1758 (1991).
25) Y.Masumoto and T.Kawamura:
"Observation of Lasing in CuCl Quantum Dots"
in "Nonlinear Optics, Fundamentals, Materials and Devices", ed. S. Miyata (Elsevier, Amsterdam, 1992) p.393; Proc. 5th Toyota Conf. on Nonlinear Optical Materials, (Aichi-ken, 1991) p.393.
26) Y.Masumoto, T.Kawamura and K.Era:
"Biexciton Lasing in CuCl Quantum Dots"
Appl. Phys. Lett. 62, 225 (1993).

<Ge, Si and AgBr nanocrystals>

27) Y.Maeda, N.Tsukamoto, Y.Yazawa, Y.Kanemitsu and Y.Masumoto:
"Visible Photoluminescence of Ge Microcrystals Embedded in SiO_2 Glassy Matrices"
Appl. Phys. Lett. 59, 3168 (1991).
28) Y.Masumoto, T.Kawamura, T.Ohzeki and S.Urabe:
"Lifetime of Indirect Excitons in AgBr Quantum Dots"
Phys. Rev. B 46, 1827 (1992).
29) Y.Kanemitsu, K.Suzuki, Y.Nakayoshi and Y.Masumoto:
"Quantum Size Effects and Enhancement of the Oscillator Strength of Excitons in Chains of Silicon Atoms"
Phys. Rev. B 46, 3916 (1992).
30)* Y.Masumoto:
"Optical Properties and New Functionality of Semiconductor Microcrystals"
Solid State Physics (Kotai Butsuri) 27, 314 (1992).
31) Y.Kanemitsu, H.Uto, Y.Masumoto and Y.Maeda:
"On the Origin of Visible Photoluminescence in Nanometer-Size Ge Crystallites"
Appl. Phys. Lett. 61, 2187 (1992).
32) Y.Kanemitsu, K.Suzuki, H.Uto, Y.Masumoto, T.Matsumoto and H.Matsumoto:
"Visible Photoluminescence of Silicon-Based Nanostructures: Porous Silicon and Silicon-Based Clusters"
Appl. Phys. Lett. 61, 2446 (1992).
33) Y.Kanemitsu, K.Suzuki, H.Uto, Y.Masumoto and T.Matsumoto:
"Optical Properties of Porous Silicon and Small Silicon Clusters: Search for the Origin of Visible Photoluminescence of Porous Silicon"
Jpn. J. Appl. Phys. 32, No.1B (1993).
34) Y.Masumoto:
"Optical Properties and New Functionality of Nanocrystalline CuCl and Ge"
To be published in MRS Proceeding (1992 MRS Fall Meeting).

<Polymers>

35) Y.Kanemitsu, A.Yamamoto, H.Funada and Y.Masumoto:
"Photocarrier Generation in Metal-Free Phthalocyanines: Effect of the Stacking Habit of Molecules on the Photogeneration Efficiency"
J. Appl. Phys. 69, 7333 (1991).

36) Y.Kanemitsu, H.Funada and Y.Masumoto:
"Disorder-Induced Transition from Gaussian to Dispersive Carrier Transport in Molecularly Doped Polymers"
Appl. Phys. Lett. 59, 697 (1991).

37) Y.Kanemitsu, H.Funada and Y.Masumoto:
"Electric Field Dependence of the Hole Drift Mobility in Molecularly Doped Polymers: Importance of Disorder of Hopping Sites"
J. Appl. Phys. 71, 300 (1992).

<Others>

38) H.Nabeta, K.Yamanaka, Y.Nagata, T.Koda, Y.Kanemitsu and Y.Masumoto:
"Characterization of Multilayered Structures by Piezoelectric Photoacoustic Imaging"
Jap. J. Appl. Phys. 30, Suppl. 30-1, 289 (1991).

39) Y.Kanemitsu, H.Nabeta, H.Matsue, A.Yamamoto, Y.Nagata, K.Yamanaka, T.Koda and Y.Masumoto:
"Photoacoustic Characterization of Semiconductor Heterostructures"
Jap. J. Appl. Phys. 31, Suppl. 31-1, 29 (1992).

40) Y.Nakayoshi, Y.Kanemitsu and Y.Masumoto:
"Dynamical Aspects of Laser Induced Phase Transformations in Amorphous GeTe"
Proc. 14th Int. Conf. on Amorphous Semiconductors - Science and Technology - (Garmisch-Partenkirchen, 1991); J. Non-Cryst. Solids 137 & 138, 1005 (1991).

41) Y.Nakayoshi, Y.Kanemitsu, Y.Masumoto and Y.Maeda:
"Dynamics of Rapid Phase Transformations in Amorphous GeTe Induced by Nanosecond Laser Pulses"
Jap. J. Appl. Phys. 31, 471 (1992).

* Publications in Japanese

2．口答発表

A．国際会議

(1) Y.Masumoto: "Optical Properties and New Functionality of Nanocrystalline CuCl and Ge", 1992 MRS Fall Meeting, Boston (Nov. 30, 1992). 〈Invited〉

B．その他の研究集会

(1)山本愛士、舛本泰章、金光義彦、中川清和："Ｓｉ－Ｇｅヘテロ構造の断面顕微ラマン分光"、日本物理学会年会(1991年9月28日).

(2)舛本泰章："ＺｎＳｅ/ＺｎＳ超格子の光物性"、日本物理学会年会(1991年9月28日).

(3)三品具文、川添忠、舛本泰章、B. Fluegel、K. Meissner、N. Peyghambarian："層状物質におけるコヒーレントフォノン効果"、日本物理学会年会(1991年9月28日).

(4)仲吉良彰、佐々木史雄、舛本泰章："CdSe薄膜における励起子共鳴励起下での超高速分光II"、日本物理学会年会(1991年9月28日).

(5)川添忠、三品具文、舛本泰章："AlGaAs/AlAsタイプII型超格子中の電子スピン緩和"、日本物理学会年会(1991年9月30日).

(6)山田陽一、舛本泰章、田口常正："超高純度ＺｎＳｅバルク結晶中の励起子分子の発光寿命、日本物理学会年会(1991年9月30日).

(7)佐々木史雄、舛本泰章、楊桓、藤安洋："Γ点タイプII型多重量子井戸ＺｎＴｅ－ＺｎＳｅの時間分解分光"、日本物理学会年会(1991年9月30日).

(8)河村智弘、舛本泰章、江良皓："CuCl微結晶間のエネルギー移動過程"、日本物理学会年会(1991年9月30日).

(9)舛本泰章、河村智弘、大関智弘、占部茂治："ＡｇＢｒ量子点の励起子の発光寿命"、日本物理学会年会(1991年9月30日).

(10)山田陽一、舛本泰章、田口常正："CdZnS-ZnS歪超格子の高密度励起効果"、応用物理学会(1991年10月9日).

(11)松江仁、山本愛士、金光義彦、舛本泰章、山賀重来、吉川明彦："格子不整合半導体ヘテロ構造の断面顕微ラマン分光による評価"、応用物理学会(1991年10月10日).

(12)江良皓、河村智弘、三島修、舛本泰章："cBNの構造付きスペクトルを示す紫外発光"、応用物理学会(1991年10月12日).

(13)前田佳均、塚本信夫、矢沢義昭、金光義彦、舛本泰章："SiO_2ガラス中のGe微結晶の可視波長フォトルミネッセンス"、応用物理学会(1991年10月12日).

(14)川添忠、三品具文、舛本泰章："AlGaAs/AlAsタイプII型超格子中の電子スピン緩和(II)"、日本物理学会年会(1992年3月28日).

(15)河村智弘、片柳智志、舛本泰章、江良皓："CuCl微結晶のレーザー発振と光学利得"、日本物理学会年会(1992年3月28日).

(16)金光義彦、鈴木克紀、仲吉良彰、舛本泰章："Ｓｉクラスターの光物性"、日本物理学会年会(1992年3月27日).

(17)片柳智志、川畑香苗、河村智弘、舛本泰章："Ｘ線小角散乱によるCuCl微結晶の構造評価と光スペクトル"、日本物理学会年会(1992年3月28日).

(18)山本愛士、金光義彦、舛本泰章："Si-Geヘテロ構造における歪と発光"、日本物理学会年会(1992年3月28日).

(19)三品具文、舛本泰章："$Ti:Al_2O_3$レーザーを用いたフェムト秒コヒーレント分光" 日本物理学会年会(1992年3月30日).

(20)山田陽一、舛本泰章、田口常正："CdZnS-ZnS歪超格子の光学利得"、日本物理学会年会(1992年3月28日).

(21)舛本泰章、河村智弘、片柳智志："CuCl量子点のレーザー発振とその特性"、応用物理学会年会(1992年3月31日).

(22)舛本泰章："半導体における静水圧と歪の効果"、応用物理学会(1992年3月29日).

(23)金光義彦、鈴木克紀、仲吉良彰、舛本泰章、松本英之、久新荘一郎、触木正伸："Siクラスターの光物性：量子サイズ効果"、応用物理学会年会(1992年3月31日).

(24)宇都裕士、金光義彦、舛本泰章、前田佳均："Ge微結晶の可視波長フォトルミネッセンスと発光機構"、応用物理学会年会(1992年３月31日).

(25)山田陽一、舛本泰章、田口常正："CdZnS-ZnS歪超格子のバンド構造"、応用物理学会年会(1992年３月29日).

(26) 片柳智志、岡本慎二、川畑香苗、Lev Zimin、舛本泰章、江良晧："CuCl微結晶の励起子・励起子分子反転分布と光学利得Ⅰ"，日本物理学会分科会(1992年9月25日).

(27) 岡本慎二、片柳智志、Lev Zimin、舛本泰章："CuCl微結晶の励起子・励起子分子反転分布と光学利得Ⅱ"，日本物理学会分科会(1992年9月25日).

(28)直江和彦、山田陽一、三品具文、Lev Zimin、舛本泰章："CdZnS-ZnS歪超格子の２光子吸収分光"，日本物理学会分科会(1992年9月26日).

(29)川添忠、三品具文、舛本泰章："AlGaAs/AlAsタイプⅡ型超格子中の電子スピン緩和Ⅲ" 日本物理学会分科会(1992年9月28日).

(30)山田陽一、舛本泰章、田口常正："CdZnS-ZnS歪超格子の光学利得Ⅱ"，日本物理学会分科会(1992年9月28日).

(31)山本愛士、金光義彦、舛本泰章："Si及びGe微粒子のラマン散乱"，日本物理学会分科会(1992年9月25日).

(32)金光義彦、宇都裕士、舛本泰章、松本貴裕、仁木登史郎、三村秀典："ポーラスSiの発光メカニズム：表面構造"，日本物理学会分科会(1992年9月25日).

(33)金光義彦、宇都裕士、舛本泰章："ナノ結晶Geの可視波長フォトルミネセンスと発光機構"，日本物理学会分科会(1992年9月25日).

(34)金光義彦、鈴木克紀、舛本泰章、小松徹、佐藤浩太、久新荘一郎、松本英之："Siクラスターの光物性Ⅱ：シート状クラスター"，日本物理学会分科会(1992年9月25日)

(35)舛本泰章："GeとAgBrの微結晶 —— サイズ効果"，応用物理学会(1992年10月16日).

(36)山田陽一、舛本泰章、田口常正："CdZnS-ZnS量子井戸と光励起紫外レーザー"，応用物理学会(1992年10月18日).

(37)山本愛士、金光義彦、舛本泰章、山賀重來、吉川明彦："ラマン散乱によるZnSe-ZnS歪超格子の高次の折り返しモード"，応用物理学会(1992年10月16日).

(38)鈴木克紀、金光義彦、舛本泰章、白石洋太郎、黒田晶美："共役系高分子を用いた擬一次元量子構造の光物性"，応用物理学会(1992年10月17日).

(39)宇都裕士、金光義彦、舛本泰章Ⅰ、松本貴裕、仁木登史郎、三村秀典："ポーラスSiの可視波長フォトルミネセンスと表面構造"，応用物理学会(1992年10月18日).

(40)金光義彦、鈴木克紀、舛本泰章、佐藤浩太、小松徹、松本英之、久新荘一郎："Siク

スターの光物性(Ⅱ)：シート状クラスター"，応用物理学会(1992年10月19日)．

(41)川添忠、三品具文、舛本泰章："AlGaAs/AlAsタイプⅡ型超格子のスピン選択光学非線形性"，日本物理学会年会(1993年3月29日)．

(42)直江和彦、山田陽一、三品具文、Lev Zimin、舛本泰章："CdZnS-ZnS歪超格子の２光子吸収分光Ⅱ"，日本物理学会年会(1993年4月1日)．

(43)片柳智志、Lev Zimin、舛本泰章："CuCl微結晶の励起子・励起子分子反転分布と光学得の精密測定"，日本物理学会年会(1993年3月30日)．

(44)仲吉良彰、川畑香苗、Lev Zimin、舛本泰章："CuCl微結晶における励起子分子発光の時間分解"，日本物理学会年会(1993年3月30日)．

(45)岡本慎二、Lev Zimin、舛本泰章："CuCl微結晶の励起子・励起子分子反転分布と光学利得スペクトル"，日本物理学会年会(1993年3月30日)．

(46)山田陽一、舛本泰章、田口常正："CdZnS-ZnS歪超格子の光学利得Ⅲ"，日本物理学会年会(1993年4月1日)．

(47)金光義彦、舛本泰章、武田京三郎、白石賢二、小川哲生："Si微結晶の可視発光と表面効果"，日本物理学会年会(1993年3月30日)．

(48)鈴木克紀、金光義彦、舛本泰章、久新荘一郎、松本英之："擬一次元ポリシランの光物性：主鎖分岐とラダー構造"，日本物理学会年会(1993年3月29日)．

(49)山本愛士、金光義彦、舛本泰章："Si微結晶のラマン散乱"，日本物理学会年会(1993年3月30日)．

(50)宇都裕士、金光義彦、舛本泰章、松本貴裕、三村秀典、仁木登史郎："ポーラスシリコンの微結晶サイズと光学特性"，日本物理学会年会(1993年3月30日)

(51)三品具文、舛本泰章："ZnP_2におけるフェムト秒時間分解分光"，日本物理学会年会(1993年3月30日)．

(52)山田陽一、舛本泰章、田口常正："CdZnS-ZnS歪量子井戸構造における光学利得の生成機構"，応用物理学会(1993年4月1日)．

(53)川添忠、三品具文、舛本泰章："AlGaAs/AlAsタイプⅡ型量子井戸を用いた円偏光光スウィッチ"，応用物理学会(1993年4月1日)．

(54)鈴木克紀、金光義彦、舛本泰章、白石洋太郎、富内芳昌、黒田昌美："共役系高分子を用いた擬一次元量子構造の光物性(Ⅱ)"，応用物理学会(1993年3月31日)．

３．著書・総説等

(1)Y.Masumoto, T.Mishina and F.Sasaki: "Dynamical Aspects of Interlayer Charge Transfer in Type II AlGaAs-AlAs Multiple-Quantum-Well Structures", in "Optical Properties of Solids" ed. by K.C.Lee, P.M.Hui and T.Kushida (World Scientific, 1991) pp.16-56 (分担執筆)．

(2)舛本泰章："半導体微結晶の光物性と新機能性"，固体物理，Vol.27，No.4，pp.314－319．

以降は、発表論文リストの原著論文 1),3),5),6),7),10),11)～14),19)～22),24),26)～29),31),32),36)から構成されていますが、一部(下記 4 件)、著作権者(出版社、学会等)の許諾を得ていないため、筑波大学では電子化・公開しておりません。

なお、電子ジャーナルとして出版社から公開されており、契約している場合は全文を読むことができますので、下記のリンク先でご覧ください。

論文 1) http://dx.doi.org/10.1016/0022-2313(91)90102-2

論文 3) http://dx.doi.org/10.1016/0022-0248(92)90846-B

論文 6) http://dx.doi.org/10.1016/0038-1098(92)90005-T

論文 10) https://www.jstage.jst.go.jp/article/jjap1962/31pt2/3B/31pt2_3B_L343/_article

Ultrafast pump-and-probe spectroscopy in CdSe: Hot-carrier and exciton dynamics

Fumio Sasaki, Tomobumi Mishina, and Yasuaki Masumoto
Institute of Physics, University of Tsukuba, Tsukuba, Ibaraki 305, Japan
(Received 30 December 1991)

An extensive study by means of femtosecond pump-and-probe spectroscopy has clarified the ultrafast dynamics of photogenerated carriers in a CdSe thin film. Under band-to-band excitation, a nonthermalized hot-carrier distribution was observed immediately upon excitation. This distribution was observed in a 200-meV broad energy range extending from the pump energy to its low-energy side. Its low-energy tail indicates that carrier-LO-phonon scattering competes with carrier-carrier scattering in the thermalization process. From the ratio of nonthermalized to the total carriers, the thermalization time was estimated to be 20–40 fs. In the wake of thermalization, cooling of photogenerated carriers was observed. With an increase of the excitation density up to 10^{19} cm^{-3}, the carrier cooling rate was slower. The cooling rate observed at 4.2 K was comparable to that at room temperature. The observed cooling rate was slower than that predicted by a theoretical calculation which took into account screening of the carrier-phonon interaction. This is ascribed to hot-phonon effects of LO phonons and TO phonons. Under resonant excitation of the *A* exciton, a 42-meV energy broadening of the *B*-exciton structure was observed. This broadening is caused by collisions between the *A* exciton and the *B* exciton. This is an example of the scattering process between different kinds of excitons. Analysis indicates that the *A*-exciton–*B*-exciton scattering time is 31 fs. This time is well explained by a simple theory based on the rigid-sphere scattering model. The broadening decreases with a time constant on the order of hundreds of picoseconds. This time constant is well explained by the lifetime of the excitons. Under resonant excitation of the *B* exciton, a fast recovery of the bleaching was observed at the *B* exciton. The recovery time of 0.9 ps is explained as the transformation time of *B* excitons into *A* excitons by LO-phonon emission. The obtained time constant agrees with the calculated scattering time based on the Fröhlich interaction within an order of magnitude.

I. INTRODUCTION

With recent advances in ultrafast laser spectroscopy, we can observe dynamical processes of carriers in semiconductors. The hot-carrier effect in semiconductors is one of the most important subjects in these studies. From a fundamental point of view, we can directly observe the dynamical carrier distribution and study the relaxation processes in semiconductors. Hot-carrier phenomena are determined primarily by band structures and carrier-phonon scattering processes. Therefore, studies of hot-carrier phenomena provide important information about carrier-phonon interactions. On the other hand, hot-carrier physics regulates the behavior of ultrafast, ultrasmall semiconductor devices operating at high electric fields. Therefore, a study of hot-carrier effects is important in understanding such devices.[1]

Up to now, hot-carrier systems have been extensively studied by means of transport experiments and luminescence spectroscopy around the fundamental gap of semiconductors. With advances in ultrafast laser spectroscopy, time-resolved absorption experiments have been adopted to study this subject. These studies have clarified the dynamics of hot carriers as follows.

Initially, photoexcited carriers are distributed at the energy of the pump pulse. Transient spectral hole burning has been experimentally observed in three-dimensional (3D),[2,3] two-dimensional,[4,5] and zero-dimensional[6] systems. The transient spectral hole diminishes in several tens or hundreds of femtoseconds depending on the excitation photon energy and density. After the transient hole diminishes, only bleaching below the pump photon energy is observed. The bleaching profile shows the carrier distribution. Generally, photoexcited carriers are thermalized by carrier-carrier scattering. The scattering time is found to be on the order of a few or a few tens of femtoseconds by means of femtosecond photon echo in GaAs.[7] In the studies of the thermalization process, experiments have dealt with the carrier-carrier scattering process. However, high-energy carriers can emit optical phonons. In this case, carrier-carrier scattering competes with optical-phonon emission. Therefore, the study of high-energy carriers enables us to observe the competition between the two processes.

Recently, one of the carrier scattering processes, an intervalley scattering process, has been extensively studied.[3] If the conduction or the valence bands have a valley minimum other than the Γ point and photoexcited carriers have enough excess energy, they can scatter to that valley. Through recent studies of GaAs and $Al_xGa_{1-x}As$ systems, the Γ-X or the Γ-L scattering is observed and it is found that the scattering time is several tens of femtoseconds. The study of the multivalley scattering mechanism is very interesting and important in itself, but such a scattering mechanism makes it difficult to study high-energy carrier distributions in GaAs systems. Unlike GaAs systems, CdSe does not suffer from intervalley scattering and, therefore, is ideal for the study

of high-energy carrier distributions.

In the succeeding time region, photoexcited carriers emit phonons and lose their energy. The cooling rate depends strongly on the carrier-phonon scattering rate. There are three types of carrier-phonon interaction mechanisms: the Fröhlich interaction, the piezoelectric interaction, and the deformation-potential interaction. If a photoexcited carrier has excess energy larger than the LO-phonon energy, carrier-LO-phonon scattering is the fastest of the three processes. If not, the other two scattering processes are the main channels of energy transfer from the carrier system to the lattice.[9,10] In order to clarify the carrier cooling mechanism, we must consider the other effects that modify the carrier-phonon interaction. One is a screening of the carrier-LO-phonon interaction by highly excited carriers.[11–13] The other is a nonequilibrium phonon distribution effect, called a hot-phonon effect.[1,12–15] Both effects make the carrier cooling very slow. In recent studies, the latter effect is found to be the dominant mechanism of slow carrier cooling in the GaAs system.[15] The fastest carrier-phonon interaction, the carrier-polar-optical-phonon scattering takes place in the region of tens or hundreds of femtoseconds. Therefore, femtosecond spectroscopy is a powerful tool to study the hot-phonon effect.

From the above-mentioned considerations, we have studied hot-carrier effects in a thin CdSe film by femtosecond pump-and-probe spectroscopy under high-energy excitation. Since CdSe has no multivalley in the conduction or valence band under 4-eV photoexcitation, we consider only scattering mechanisms in the Γ valley. Therefore, we can study a dynamical carrier distribution confined to the Γ valley at high-energy excitation. As a result, a nonequilibrium distribution was observed immediately upon excitation. The nonthermalized distribution extended from the pump energy to its low-energy side. This feature shows the competition between carrier-carrier scattering and carrier-LO-phonon scattering.

One of the other interests in femtosecond spectroscopy is to clarify dynamics or optical nonlinearities of excitons in semiconductors.[16] Studies of exciton-exciton scattering processes and exciton-phonon scattering processes reveal the origin of the large optical nonlinearity of excitons. Therefore, these studies are necessary for the design and fabrication of optoelectronic devices. In CdSe, A-exciton and B-exciton peaks are observed near the fundamental absorption edge. The energy splitting between the A exciton and the B exciton is comparable to the LO-phonon energy. This situation is suitable for the study of collisions between A excitons and B excitons or exciton-LO-phonon scattering.

In Sec. II, the experimental condition of the pump-and-probe experiments is described. In Sec. III, discussions about hot-carrier systems under band-to-band excitation are given. In Sec. IV, we discuss the dynamics of excitons under resonant excitation.

II. EXPERIMENTS

In this study, two short-pulse laser sources were utilized. The first laser source consists of a cw mode-locked Nd^{3+}:YAG (YAG denotes yttrium aluminum garnet) laser, the first-stage fiber compressor, a second-harmonic generator, a synchronously pumped cavity-dumped dye laser, the second-stage fiber compressor, and a dye amplifier pumped by a Q-switched Nd^{3+}:YAG laser. In this case, the pump-phonon energy was 2.12 eV and pulse energy was about 400 μJ with a 260-fs pulse width. The laser pulses were split into two beams. One beam was focused on a water cell and generated white continuum-femtosecond pulses. The white-light beam was used as a probe beam and the desired spectral range was selected with color filters. The pump beam was sent through an optical delay. The excitation and probe beam power were varied by using rotational neutral-density filters that produce no change in the time delay or in the dispersion. The diameters of the spot and overlap of the two beams were checked with a microscope.

The second laser source was based on a colliding-pulse mode-locked dye laser and a multipass amplifier pumped by a Cu-vapor laser. This laser system is operational in the Optical Sciences Center of the University of Arizona and was used for some of the experiment reported in this paper. The amplified beam was focused on an ethyleneglycol jet and generated a white-light continuum. Part of the white light was used as a weak probe beam. The remaining part was sent through an interferential filter with a band width of about 10 nm. This beam was amplified using another multipass amplifier and used as the pump. With this system, we can tune the pump-photon energy to the A-exciton and B-exciton resonances. The pump pulse width was between 110 and 130 fs, depending on the photon energy. To reduce the scattered pump light, especially in the case of resonant pump experiments, the pump-and-probe beams were polarized orthogonally and an analyzer in the detection system selected only the probe light.

In femtosecond experiments, one difficulty comes from dispersion compensation. If we want to observe a wide-range spectrum, we must suppress the dispersion of the optics as far as possible. The temporal dispersion of the probe in these systems was less than 10 fs/nm. Taking into account the second-order term in the dispersion, a least-squares fit of the experimental dispersion was done. The agreement between the experimental results and the fit was very good, and the maximum deviation of the data from the fitting curve was smaller than 10 fs. Based on this fit, the time delays of the probe spectra were given a wavelength-dependent correction. In this way, time-resolved spectra were obtained in a wide energy range.

The sample was a 0.65-μm-thick CdSe thin film grown on a mica substrate by means of hot-wall epitaxy. The crystal c axis was perpendicular to the mica substrate. A mica substrate is suitable for the absorption experiment because it is transparent to visible light. Moreover, mica is a layered compound and its interlayer interaction comes from van der Waals force. Therefore, the strain between a mica substrate and a CdSe crystal is considered to be much smaller than other systems. Typical transmissivity at the pump photon energy was about 5% in this sample.

Four experiments were conducted: (1) pump at 2.12

eV with a pulse width of 260 fs at 4.2 K, (2) pump at 2.12 eV with a pulse width of 260 fs at room temperature, (3) pump at 1.86 eV with a pulse width of 110 fs at 10 K, and (4) pump at 1.82 eV with a pulse width of 130 fs at 10 K. Experiments (1) and (2) correspond to band-to-band excitation. Experiments (3) and (4) correspond to resonant excitation of the B exciton and A exciton, respectively. The data acquisition was done using an optical multichannel analyzer and a 25-cm spectrometer with low dispersive gratings (300 or 600 groves/mm) to obtain a wide-energy-range spectrum.

III. EXPERIMENTAL RESULTS UNDER BAND-TO-BAND EXCITATION AND DISCUSSIONS

A. Nonequilibrium distribution of photoexcited carriers

Under band-to-band excitation, a large number of free carriers is generated with kinetic energy greater than the optical-phonon energy by an intense optical pulse. The kinetic energy per carrier was on the order of 100 meV, which depends on the difference between the band gap and the excitation photon energy. The estimated carrier density was on the order of $10^{19}\,\mathrm{cm}^{-3}$.

Figures 1 and 2 show time-resolved absorption spectra under experimental conditions (1) and (2). Condition (1) corresponds to the 2.12-eV excitation at 4.2 K and condition (2) to the same excitation at room temperature. The excitation densities were 900 and 600 $\mu\mathrm{J\,cm}^{-2}$, respectively. The absorption spectra denoted "NO PUMP" were obtained from probe transmission in the absence of the pump pulses. Structures of the A exciton and the B exciton are clearly observed in Fig. 1. In Fig. 2, the A-exciton structure is observed as a kink around 1.76 eV. The spectrum at 0 ps shows a broad spectral dip around 2.0 eV in Fig. 1. There seems to be a broader spectral dip around 1.9 eV in Fig. 2. These features are due to a non-

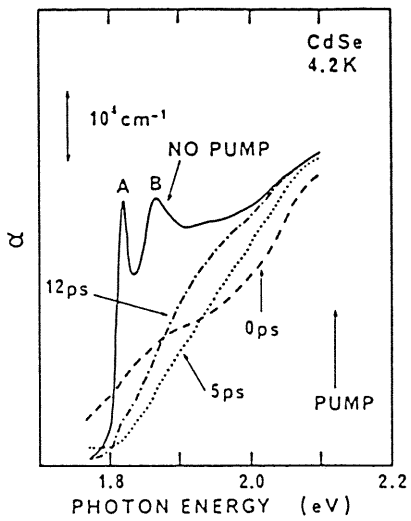

FIG. 1. Time-resolved absorption spectra of CdSe observed under 2.12-eV excitation at 4.2 K. The solid line denoted by "NO PUMP" shows the spectrum without the pump. Pump-and-probe spectra at 0-, 5-, and 12-ps time delays are shown.

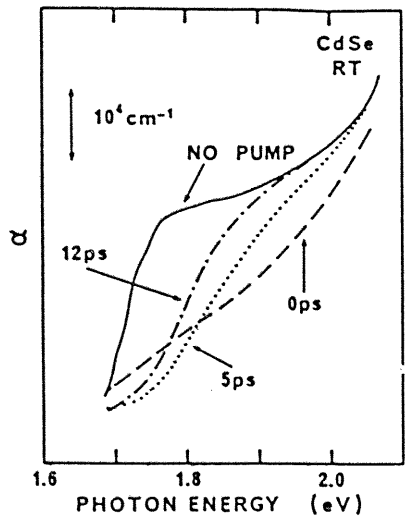

FIG. 2. Time-resolved absorption spectra of CdSe observed under 2.12-eV excitation at room temperature. The solid line denoted by "NO PUMP" shows the spectrum without the pump. Pump-and-probe spectra at 0-, 5-, and 12-ps time delays are shown.

thermalized distribution of hot carriers. In order to see the carrier distribution clearly, we plotted the time-resolved absorption spectra in the form of $-\Delta\alpha/\alpha$, where α and $\Delta\alpha$ denote the absorption coefficient and the change of α induced by the optical pumping, respectively. Figures 3 and 4 show these spectra under experimental conditions (1) and (2), respectively.

The relation between $-\Delta\alpha/\alpha$ and an electron (hole) distribution function $f_e(E_e)\,[f_h(E_h)]$ is expressed by[17]

$$-\Delta\alpha/\alpha = f_e(E_e) + f_h(E_h)\,. \tag{3.1}$$

Here, E_e and E_h denote the kinetic energy of electrons and holes, respectively. The kinetic energies of an electron and a hole are represented by

$$E_i = (\mu/m_i)(E - E_g) \quad (i = e,h)\,, \tag{3.2}$$

where μ, m_i, E, and E_g denote the reduced mass of an electron and a hole, an effective mass, the probe photon energy, and the band gap, respectively. In this analysis, one may take into account the anisotropy in the A-hole band. This simple expression (3.1) is then modified.[18] In order to estimate the anisotropy effect in the absorption spectrum, a calculation with and without the anisotropy was done. The calculation method is outlined in the Appendix. Figure 13 in the Appendix shows that the anisotropy effect is small. Therefore, we have neglected it for simplicity.

Further, we approximately replaced the right-hand side of Eq. (3.1) at the high-energy tail by the larger term. Because both $f_e(E_e)$ and $f_h(E_h)$ are the exponentially decaying functions at the high-energy tail, the smaller term is considered to be negligible compared with the larger term. Then, analysis procedures become simple as follows.[19]

We analyzed the $-\Delta\alpha/\alpha$ spectra by fitting the single

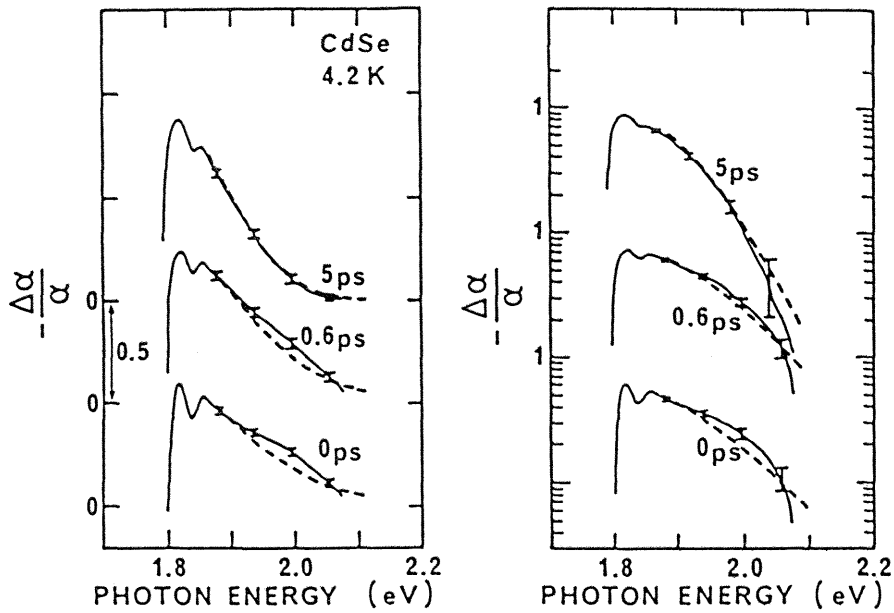

FIG. 3. The change in the absorption coefficient divided by the unperturbed absorption coefficient $-\Delta\alpha/\alpha$ observed under 2.12-eV excitation at 4.2 K. The left-hand part shows $-\Delta\alpha/\alpha$ in the linear scale, and the right-hand part shows $-\Delta\alpha/\alpha$ in the logarithmic scale. The effective temperature of hot carriers, T_c, is estimated from the fitting shown by dashed lines. Values of T_c for spectra at 0, 0.6, and 5 ps are 970, 850, and 540 K, respectively.

Fermi distribution function

$$f_c(E)=1/\{\exp[(E-E_F)/k_BT_c]+1\}\ ,$$

where E_F, T_c, and k_B denote the chemical potential, the effective temperature of hot carriers, and the Boltzmann constant, respectively. Almost all the spectra can be well fitted by a single Fermi distribution function except the spectra around the time origin. The spectra at 5 ps are well fitted by a single Fermi distribution function as shown in Figs. 3 and 4. However, the spectra observed at 0 ps cannot be fitted. Moreover, the spectrum shows a convex part around 2.0 eV in Fig. 3. In Fig. 4, the spectrum observed around 1.9 eV is not concave upward.

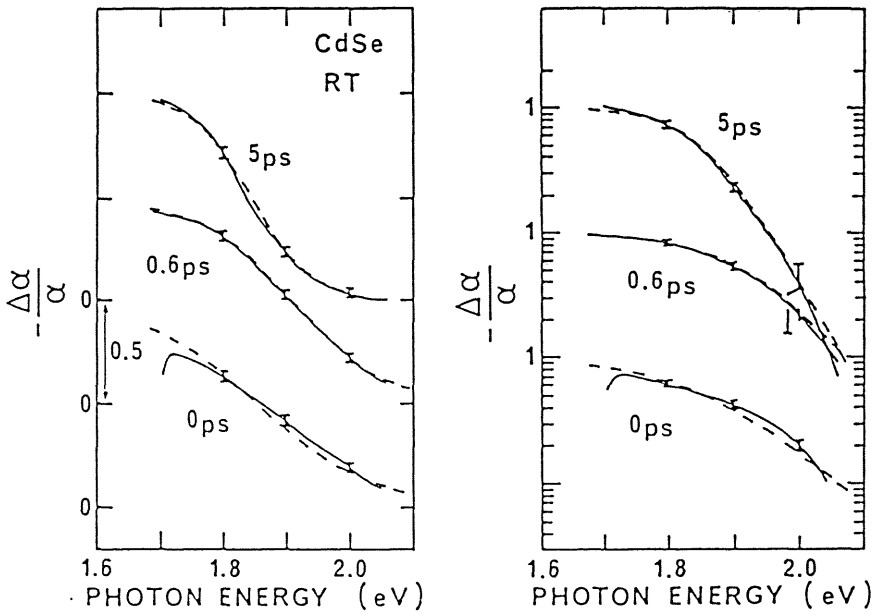

FIG. 4. The change in the absorption coefficient divided by the unperturbed absorption coefficient $-\Delta\alpha/\alpha$ observed under 2.12-eV excitation at room temperature. The left-hand part shows $-\Delta\alpha/\alpha$ in the linear scale and the right-hand part shows $-\Delta\alpha/\alpha$ in the logarithmic scale. The effective temperature of the hot carriers, T_c, is estimated from the fitting shown by dashed lines. Values of T_c for spectra at 0, 0.6, and 5 ps are 1100, 860, and 560 K, respectively.

The Fermi distribution function is concave upward below its value of 0.5. Therefore, the spectra observed around 2.0 eV in Fig. 3 and 1.9 eV in Fig. 4 indicate a nonthermalized distribution of hot carriers.

This nonequilibrium distribution of hot carriers was thermalized before the end of the pump pulse by carrier-carrier scattering. So far, the thermalization time has been estimated in 3D GaAs by means of femtosecond pump-and-probe spectroscopy.[2] In that experiment, carriers had small excess energy and were not able to emit an LO phonon. However in our experiment, carriers had enough excess energy to scatter and emit LO phonons. Therefore, the nonthermalized distribution observed in this experiment spread over a 200-meV-broad energy range. The low-energy tail of the nonthermalized distribution indicates that the carrier-LO-phonon scattering process competes with the carrier-carrier scattering process.

The thermalization time could not be observed in the time trace because of the limited time resolution, but we estimated the thermalization time from the spectra at 0 ps. A simple rate equation is written by

$$dn/dt = g(t) - n/\tau_d \,, \tag{3.3}$$

where n, $g(t)$, and τ_d denote the carrier density, the generation rate of the photoexcited carriers, and the decay rate, respectively. We can neglect the decay term because of the fairly long lifetime of carriers. We separate the nonthermalized carrier density n^n from the equilibrium carrier density n^e. Then, Eq. (3.3) becomes

$$dn^n/dt = g(t) - n^n/\tau \,, \quad dn^e/dt = n^n/\tau \,, \tag{3.4}$$

where τ denotes the thermalization time constant. If the generation rate is constant within the experimental time resolution δt, the nonthermalized carrier density at time

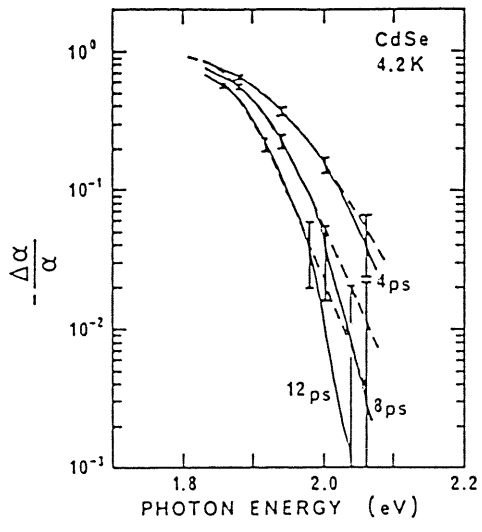

FIG. 5. The change in the absorption coefficient divided by the unperturbed absorption coefficient $-\Delta\alpha/\alpha$ observed under 2.12-eV excitation at 4.2 K (solid lines). The vertical scale is logarithmic. The fitted Fermi distribution functions are shown by dashed lines. Values of the estimated temperature for spectra at 4, 8, and 12 ps are 530, 440, and 390 K, respectively.

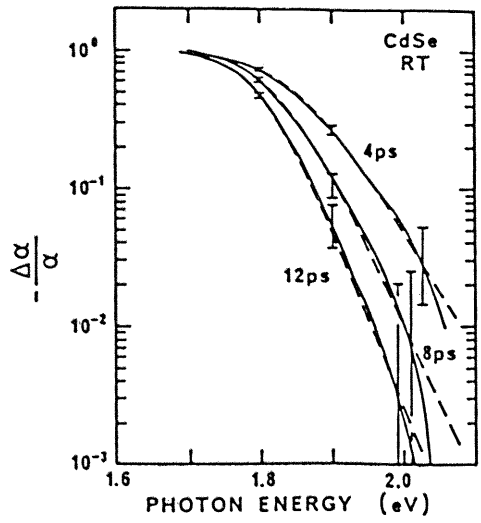

FIG. 6. The change in the absorption coefficient divided by the unperturbed absorption coefficient $-\Delta\alpha/\alpha$ observed under 2.12-eV excitation at room temperature (solid lines). The vertical scale is logarithmic. The fitted Fermi distribution functions are shown by dashed lines. Values of the estimated temperature for spectra at 4, 8, and 12 ps are 590, 460, and 400 K, respectively.

δt is represented by

$$n^n(\delta t) = \int_{-\infty}^{\delta t} \frac{\delta n}{\delta t} \exp[(t' - \delta t)/\tau] dt' = \frac{\delta n}{\delta t}\tau \,. \tag{3.5}$$

Here, δn denotes the total carrier density generated within the time resolution. Equation (3.5) shows that the thermalization time τ is estimated to be $(n^n/\delta n)\delta t$.

From the experimental results shown in Figs. 3 and 4, the ratios of the nonthermalized distribution to the total one were obtained as 10% for the spectrum at 0 ps in 4.2

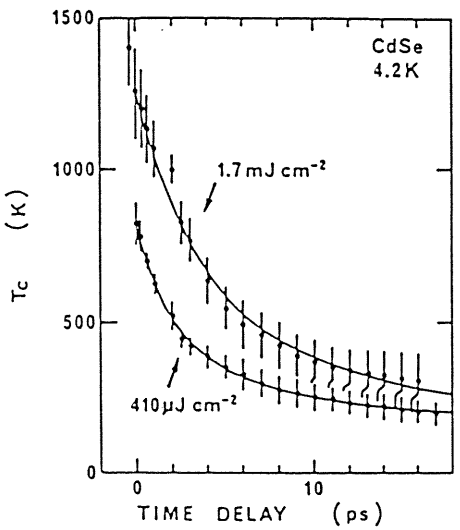

FIG. 7. Temporal change of the estimated temperature, T_c, observed at 4.2 K. Solid circles show experimentally estimated temperatures. Solid lines are the numerically fitted result. Upper and lower curves show the data obtained under 1.7-mJ cm^{-2} and 410-μJ cm^{-2} excitation, respectively.

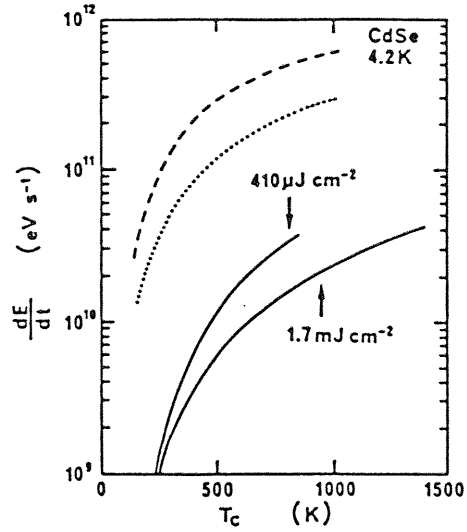

FIG. 8. Solid lines show the energy-loss rate of hot carriers observed at 410-μJ cm^{-2} and 1.7-mJ cm^{-2} excitation. Dashed and dotted lines show the calculated energy-loss rate at carrier densities of 1×10^{19} and 6×10^{19} cm^{-3}, respectively.

K and 5% at room temperature. Therefore, approximately 5–10 % of the present time resolution of 400 fs roughly gives the thermalization time of 20–40 fs.

B. Cooling of hot carriers

Cooling of hot carriers was observed in the picosecond time regime. Figure 5 shows the data taken at 4.2 K and Fig. 6 shows the data taken at room temperature. In this time regime, the spectra are well described by a Fermi distribution as shown by the dashed line in Figs. 5 and 6. Therefore, cooling of the hot carriers is characterized by an effective temperature of the hot carriers. The fitted carrier temperatures at 4, 8, and 12 ps are 580, 440, and 390 K, respectively, in Fig. 5. In Fig. 6, those at 4, 8, and 12 ps are 590, 460, and 400 K, respectively. The fitted carrier temperature at 4.2 K is similar to that at room temperature. This fact indicates that the cooling rate observed at 4.2 K is comparable with that observed at room temperature, since the carrier temperature is much higher than the lattice temperature.

The temporal changes of T_c observed at different excitation densities are plotted in Fig. 7. The lower and upper curves show the results observed at the excitation density of 410 μJ cm^{-2} and 1.7 mJ cm^{-2}, respectively. The carrier densities estimated from the transmissivity of the pump pulse were 1×10^{19} and 6×10^{19} cm^{-3}, respectively. Solid circles are the fitted carrier temperature. Vertical bars are error bars of the fitting. In order to compare the observed carrier cooling rate with a calculated rate, we differentiated these curves by time. After fitting the experimental data by the solid lines shown in Fig. 7, we took the differential of the curves. The results are shown by solid lines in Fig. 8 as a function of T_c. This result shows that the carrier cooling rate slows with an increase of excitation density. The dashed and dotted curves show the calculated energy-loss rate based on screening of the carrier-phonon interaction.[12,13]

In this calculation, we took into account four carrier-phonon interactions: the carrier-LO-phonon scattering based on the Fröhlich interaction, the carrier-acoustic-phonon scattering based on the piezoelectric scattering, the carrier-TO-phonon scattering based on the optical deformation-potential scattering, and the carrier-acoustic-phonon scattering based on the deformation-potential scattering. The energy-loss-rate formula and parameters used in the calculations were those in Ref. 13.

As a result of the calculation, the dashed and dotted curves were obtained at carrier densities of 1×10^{19} and 6×10^{19} cm^{-3}, respectively. These densities are the values estimated from the experiment. The disagreement between the observed energy-loss rate and the calculated rate is probably due to the hot-phonon effect. At these high carrier densities, the screening of the Fröhlich interaction works more sensitively than that of the optical deformation-potential interaction, so that the energy-loss rate by LO-phonon emission is found to be comparable with that by TO-phonon emission. Therefore, the observed slow energy-loss rate is attributed to the hot-phonon effects of both LO and TO phonons.

IV. EXPERIMENTAL RESULTS UNDER RESONANT EXCITATION OF EXCITONS AND DISCUSSIONS

A. A-exciton resonant excitation

Figure 9 shows the change in the absorption spectra $-\Delta\alpha$ under resonant excitation of the A exciton. The bleaching has peaks at both the A-exciton and B-exciton resonances. Initially, induced absorption is observed around the A-exciton resonance. The induced absorption observed at the low-energy side of the A exciton diminishes with time. As this occurs, the induced absorption at the high-energy side of the B exciton grows. Such a

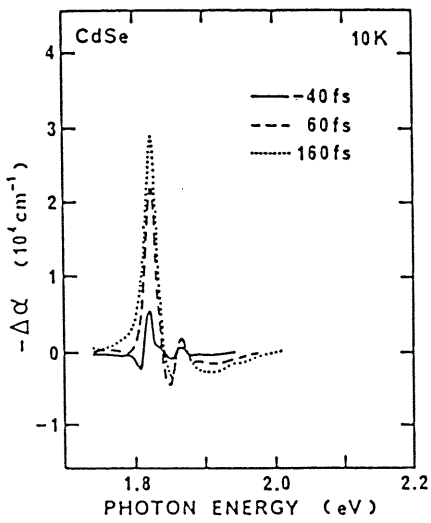

FIG. 9. Time-resolved absorption change $-\Delta\alpha$ observed under resonant excitation of the A exciton at 10 K around the time origin.

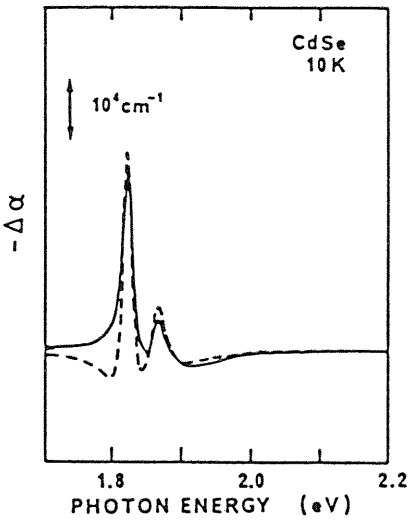

FIG. 10. Fitting of line broadening. The solid line shows an experimental spectrum observed under A-exciton resonant excitation at 560 fs. The dashed line shows a calculated spectrum based on the broadening of two Lorentzian functions.

spectral change is interpreted as a broadening of both the absorption lines. We ascribe this energy broadening of each absorption line to collisional broadening of excitons.

The collisional broadening of excitons in GaAs was previously observed in Figs. 1 and 2 of Ref. 4 by femtosecond pump-and-probe experiments. In that experiment, excitons collide with free carriers. In our experiment, A excitons were initially excited at 10 K, which is too low a temperature to ionize the exciton. Therefore, the energy broadening of the B-exciton resonance is caused by mutual collisions between A excitons and B excitons. This is an example of collisions among different kinds of excitons. Another example of collisions between different kinds of excitons was recently reported for magnetoexcitons in GaAs quantum wells.[20]

The broadening of the exciton line yields the scattering time of the excitons. The spectral shape of an absorption line caused by collisional broadening is represented by a Lorentzian function. In this case, the relation between the energy width (full width at half maximum) ΔE and the mean scattering time τ_s is expressed by $\Delta E\tau_s \sim 2\hbar$. From this relation, we can estimate the exciton-exciton scattering time. In order to obtain the energy broadening ΔE, we fitted the calculated spectrum to the experimental spectrum $-\Delta\alpha$, as shown in Fig. 10. In this fitting, we used two Lorentzian functions. The solid and dashed lines show the experimental spectrum observed at 560 fs and the fitted spectrum. The induced absorption observed at the high-energy side of the B exciton is well fitted.

Initially, broadening of the A exciton is observed below the A-exciton peak, as shown in Fig. 9. The broadening below the A exciton disappears as soon as the bleaching become large. The bleaching caused by phase-space filling is observed at the low-energy side of the A exciton and balances the effects of the broadening. However, the broadening observed above the A exciton remains and is not masked by the bleaching.

The fitting showed the energy broadening of the B exciton and the A exciton to be about 42 and 27 meV, respectively. Inserting these values into the equation $\Delta E\tau_s \sim 2\hbar$, we obtain a scattering time of 31 fs between the B excitons and the A excitons. We also obtain a mean scattering time of 49 fs between the A excitons and the A excitons.

The exciton-exciton scattering rate was experimentally determined using time-resolved degenerate four-wave mixing,[21] and was theoretically calculated by Manzke, Henneberger, and May.[22] However, these studies only dealt with collisions between the same excitons or between excitons and free carriers. It is difficult to model the collision processes between different kinds of excitons taking into account the many-particle problems. Therefore, we estimate the collision rate from a simple theory. Since excitons have no charge, we use a model of rigid-sphere scattering as the scattering mechanism of excitons. We assume that the photoexcited A excitons obey the Boltzmann distribution at the lattice temperature T_L. The B excitons generated by a probe pulse collide with the A excitons. In this case, the A exciton and B exciton mutual scattering rate $1/\tau_{A\text{-}B}$ is represented by

$$1/\tau_{A\text{-}B} = 2n_{ex}(a_A + a_B)^2(2\pi k_B T_L / M_{AB})^{1/2} , \quad (4.1)$$

where n_{ex}, M_{AB}, a_A, and a_B denote the A-exciton density, the reduced mass between the A exciton ($0.93m_0$) and the B exciton ($1.03m_0$), the Bohr radius of the A exciton (5.3 nm), and that of the B exciton (4.9 nm), respectively. Here, m_0 denotes the bare electron mass. In the experiments, the values of n_{ex} and T_L were 3×10^{18} cm^{-3} and 10 K, respectively. The calculated scattering time is 36 fs. The agreement between the observed 31 fs and estimated 36 fs is very good. Utilizing this model, the broadening of the B-exciton resonance is well explained by the A-exciton–B-exciton collisional broadening.

The energy broadening of both excitons is found to increase consistently with the excitation density. This fact also supports this model. In this simple model, however, the A-exciton–A-exciton collision time $\tau_{A\text{-}A}$ is 34 fs, which is comparable with the A-exciton–B-exciton collision time. The difference between $\tau_{A\text{-}A}$ and $\tau_{A\text{-}B}$ obtained from the experiment cannot be explained by this model. This may be due to the Pauli exclusion between the A exciton and another A exciton.

B. B-exciton resonant excitation

Figure 11 shows the results of resonant excitation of the B exciton. The left-hand part of this figure shows the spectra around the time origin and the right-hand part shows the spectra in the picosecond regime. Initially, the bleaching of both the A exciton and the B exciton increases at the same time. However, the bleaching at the B exciton decreases more rapidly than that at the A exciton, as shown in the right-hand part of Fig. 11. The time dependence of the bleaching at the B exciton is plotted in Fig. 12. The solid line shows the experimental result and the dashed line shows the fit to a double-exponentially decaying function. From the fitting, the time constants of

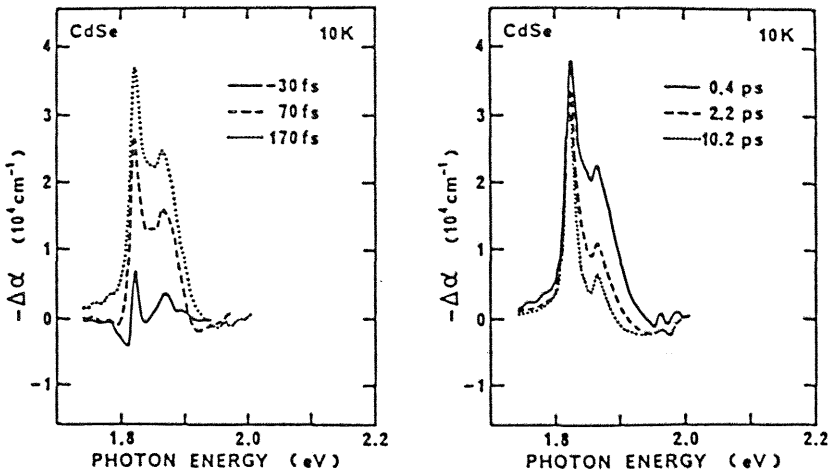

FIG. 11. Time-resolved absorption change $-\Delta\alpha$ observed under resonant excitation of the B exciton. The left-hand part shows spectra around the time origin and the right-hand part shows spectra in the picosecond regime.

the fast component and the slow component were found to be 0.9 and 53 ps, respectively.

Here, we discuss the fast recovery component. The recovery time of the B exciton's bleaching is much faster under B-exciton resonant excitation than under either A-exciton resonant excitation or band-to-band excitation. This is explained by a fast-scattering process from the B exciton to the A exciton.

The energy splitting between the A-hole band and the B-hole band, ΔE_{AB}, is 41 meV, as shown in Fig. 1.[23] Therefore, the photoexcited B exciton can emit a LO phonon and be transformed into an A exciton. The scattering time of the B exciton with the LO phonon, $1/\tau_{\rm LO}^{\rm ex}$, is estimated by using the Fröhlich interaction.[9,24] This process is the fastest among the exciton-phonon interactions. The scattering rate of the B exciton is obtained by integration of the square of the matrix element. As a result, $1/\tau_{\rm LO}^{\rm ex}$ is represented by

$$1/\tau_{\rm LO}^{\rm ex}=\frac{e^2\hbar\omega_{\rm LO}\mu_B}{4\pi\varepsilon_{\rm vac}\hbar^2}\left[\frac{1}{\varepsilon_\infty}-\frac{1}{\varepsilon_0}\right]\frac{N_{\rm LO}(T_L)+1}{\hbar k_A}\times\int\frac{(q_e-q_h)^2}{q}dq\ . \tag{4.2}$$

Here, $\hbar\omega_{\rm LO}$, μ_B, $\varepsilon_{\rm vac}$, ε_∞, ε_0, $N_{\rm LO}$, and k_A denote the LO-phonon energy, the reduced mass of the B exciton ($0.11m_0$), the dielectric constant of vacuum, the optical and static dielectric constants of CdSe, the LO-phonon occupation number, and the A-exciton wave vector, respectively. The range of integration is written by the inequality

$$k_A\left|1-\left|1-\frac{2\mu_A}{\hbar^2k_A^2}(\Delta E_{AB}-\hbar\omega_{\rm LO})\right|^{1/2}\right|<q<k_A\left|1+\left|1+\frac{2\mu_A}{\hbar^2k_A^2}(\Delta E_{AB}-\hbar\omega_{\rm LO})\right|^{1/2}\right|\ . \tag{4.3}$$

In Eq. (4.2), q_e and q_h denote the Fourier transform of the electron and hole charge-distribution functions that are represented by[24]

$$q_e=\left[1+\left[\frac{m_h}{m_e+m_h}\frac{qa_B}{2}\right]^2\right]^{-2},\qquad q_h=\left[1+\left[\frac{m_e}{m_e+m_h}\frac{qa_B}{2}\right]^2\right]^{-2}. \tag{4.4}$$

Inserting Eq. (4.4) into (4.2), we obtain a scattering time of 0.2 ps. The experimental value agrees with the calculated one within one order of magnitude. The disagreement between the experimental scattering time and the calculated scattering time may come from the hot-phonon effect of LO phonons.

Recently, a time-resolved reflection measurement was adopted to this study and a transition time of 0.9 ps was measured.[25] The time constant obtained by our experiment agrees with this value. However, in this reflection

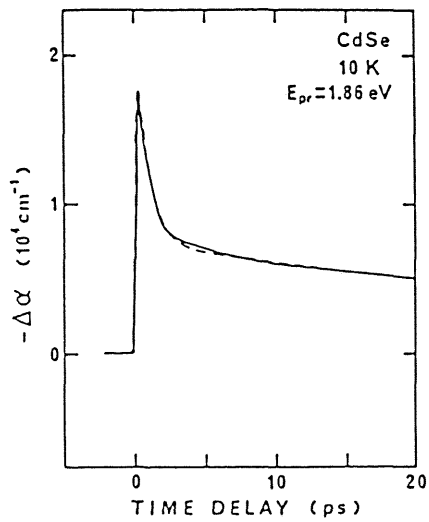

FIG. 12. The time dependence of bleaching observed at the B exciton. The solid line shows the experimental result. The dashed line shows the fit to a double-exponentially decaying function.

experiment, the time resolution (~0.6-ps pulse width) was comparable with the observed transition time. In our experiment, the time resolution was 110 fs, so that the recovery-time constant is measured with enough accuracy.

Another merit of this experiment is to observe the whole spectrum around the band edge, as shown in Fig. 11. As already mentioned, the B-exciton bleaching drastically decreases in the picosecond regime. We ascribed the fast recovery of this bleaching to the $B \rightarrow A$ transformation. Therefore, the population of the B exciton is expected to decrease. In contrast, the population of the A exciton is expected to increase. Both the populations modify the bleaching observed at the A exciton. From the experimental result, the bleaching observed at the A exciton decreases in the picosecond regime, as shown in the right-hand part of Fig. 11. The recovery of this bleaching is small but is found to have a fast component. The recovery-time constant observed at the A exciton is comparable with that observed at the B exciton. In our experimental condition, free carriers are also excited from the A-hole band. Therefore, the small recovery of the bleaching observed at the A exciton may come from the reduction of the free carriers or the B-exciton population.

V. CONCLUSIONS

In this work, ultrafast pump-and-white-continuum-probe spectroscopy was adopted to study the dynamical behavior of photogenerated carriers in a CdSe thin film. As a result, dynamics of photogenerated carriers in CdSe are clarified as follows.

Under band-to-band excitation, a nonthermalized hot-carrier distribution was observed during the pump pulse. The nonthermalized distribution was observed not only at the pump energy, but also on the low-energy side of the pump energy. This is due to the fast carrier-LO-phonon scattering process. The thermalization time could not be resolved in the experiment, but the ratio of the nonthermalized to the total carriers gave the thermalization time of 20–40 fs.

In the cooling process of photogenerated hot carriers, the carriers lose their excess energy by emitting phonons while maintaining a thermalized distribution. The observed slow carrier cooling rate is not explained by screening of the carrier-phonon interaction. This is probably explained by hot-phonon effects of both LO and TO phonons.

Under resonant excitation of the A exciton, broadening of the B exciton was observed. The observed broadening gave the A-exciton–B-exciton scattering time of 31 fs. This value is well explained by a rigid-sphere scattering model. This is an example of the interaction among different kinds of excitons.

Under resonant excitation of the B exciton, a fast recovery of the bleaching was observed at the B exciton. This fast recovery with a 0.9-ps time constant is well explained by transformation of the B exciton to the A exciton with emission of an LO phonon through the Fröhlich interaction.

ACKNOWLEDGMENTS

The authors are grateful to Professor H. Fujiyasu and Professor A. Ishida and their co-workers at Shizuoka University for the kind guidance regarding hot-wall epitaxy, and to S. Koide for the sample preparation. They also acknowledge Professor N. Peyghambarian, B. Fluegel, and K. Missner for critical reading of this manuscript. The measurements with resonant excitation of excitons were performed at the Optical Sciences Center, University of Arizona. This work was supported by the International Science Research Program No. 02044021 and the Scientific Research Grant-in-Aid No. 02952058 from the Ministry of Education, Science and Culture of Japan (MESC).

APPENDIX: ANISOTROPY OF THE BAND STRUCTURE

The absorption spectrum is proportional to the imaginary part of the susceptibility, expressed as[18]

$$\mathrm{Im}\chi(E) \propto \left[\frac{2\mu}{\hbar^2}\right]^{3/2} (E-E_g)^{1/2}\theta(E-E_g)N(E-E_g) . \tag{A1}$$

Here, E, μ, and E_g represent the photon energy, a reduced mass between an electron and a hole, and the energy gap, respectively. The step function $\theta(E-E_g)$ precludes absorption below the band gap. The phase space filling effect is taken into account in the term $N(E-E_g)$, which is represented by

$$N(E)=1-f(\alpha_e E-E_e^F)-f(\alpha_h E-E_h^F) . \tag{A2}$$

Here, E_e^F and E_h^F represent the electron and hole quasi-Fermi energies. The prefactors α_e and α_h mean μ/m_e and μ/m_h, respectively. The anisotropy in the band structure changes μ and $N(E-E_g)$. By using the aniso-

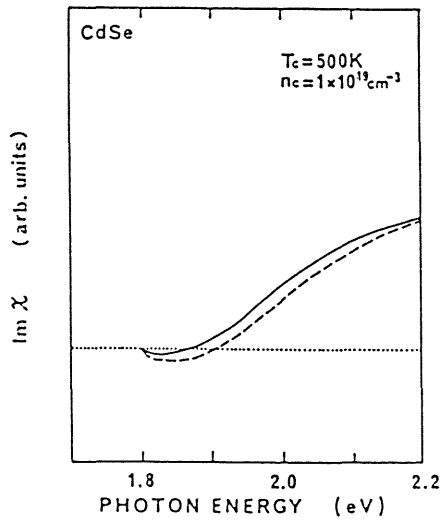

FIG. 13. The calculated imaginary part of the susceptibility. The solid line shows the anisotropic case and the dashed line shows the isotropic case.

tropic masses of the electron ($m_e^{\perp}$ and $m_e^{\parallel}$) and the hole ($m_h^{\perp}$ and $m_h^{\parallel}$), $N(E-E_g)$ is represented by[18]

$$N(E-E_g)=\int_0^1 ds\{1-f([\gamma+\eta s^2]E-E_e^F) -f([1-\gamma-\eta s^2]E-E_h^F)\}\ , \tag{A3}$$

$$\gamma=\frac{m_h^{\perp}}{m_e^{\perp}+m_h^{\perp}}\ ,\quad \eta=\frac{m_h^{\parallel}}{m_e^{\parallel}+m_h^{\parallel}}\ .$$

The effective masses of the electron and the hole are replaced by averaged values, $m_e=(m_e^{\perp 2}m_e^{\parallel})^{1/3}$ and $m_h=(m_h^{\perp 2}m_h^{\parallel})^{1/3}$. The anisotropic masses in CdSe were chosen as $m_e^{\perp}=m_e^{\parallel}=0.13m_0$, $m_h^{\perp}=0.45m_0$, and $m_h^{\parallel}=2.5m_0$, where m_0 denotes a bare electron mass.

Inserting Eq. (A3) into (A1), we obtained the imaginary part of the susceptibility, including the anisotropy of the hole band. Figure 13 shows the result obtained under a carrier temperature of 500 K and density of 1×10^{19} cm^{-3}. The band gap was fixed at 1.8 eV in both cases. The difference with and without the anisotropy is about 10% around 2.1 eV. Therefore, it is acceptable to neglect the anisotropy in the A-hole band.

[1]For a recent review, see J. Shah, IEEE J. Quantum Electron. QE-22, 1728 (1986); D. H. Auston, Phys. Today 43 (2), 46 (1990).

[2]J. L. Ouder, D. Hulin, A. Migus, A. Antonetti, and F. Alexandre, Phys. Rev. Lett. 55, 2074 (1985).

[3]W. Z. Lin, R. W. Schoenlein, S. D. Brorson, J. G. Fujimoto, and E. P. Ippen, in *XV International Quantum Electronics Technical Digest Series* [Opt. Soc. Am. 21, 82 (1987)]; C. H. Brito-Cruz, R. L. Fork, and C. V. Shank, *ibid.*

[4]W. H. Knox, C. Hirlimann, D. A. B. Miller, J. Shah, D. S. Chemla, and C. V. Shank, Phys. Rev. Lett. 56, 1191 (1986).

[5]W. H. Knox, D. S. Chemla, G. Livescu, J. E. Cunningham, and J. E. Henry, Phys. Rev. Lett. 61, 1290 (1988).

[6]N. Peyghambarian and S. W. Koch, Rev. Phys. Appl. 22, 1711 (1987).

[7]P. C. Becker, H. L. Fragnito, C. H. Brito Cruz, R. L. Fork, J. E. Cunningham, J. E. Henry, and C. V. Shank, Phys. Rev. Lett. 61, 1647 (1988); J.-Y. Bigot, M. T. Portella, R. W. Schoenlein, C. V. Shank, and J. E. Cunningham, in *Ultrafast Phenomena VII*, edited by C. B. Harris, E. P. Ippen, G. A. Mourou, and A. H. Zewail (Springer, Berlin, 1990), p. 239.

[8]M. J. Rosker, F. W. Wise, and C. L. Tang, Appl. Phys. Lett. 49, 1726 (1986); W. Z. Lin, J. G. Fujimoto, E. P. Ippen, and R. A. Logan, *ibid.* 50, 124 (1987); W. Z. Lin, J. G. Fujimoto, E. P. Ippen, and R. A. Logan, *ibid.* 51, 161 (1987); P. C. Becker, H. L. Fragnito, C. H. Brito-Cruz, J. Shah, R. L. Fork, J. E. Cunningham, J. E. Henry, and C. V. Shank, *ibid.* 53, 2089 (1988); W. Z. Lin, R. W. Schoenlein, J. G. Fujimoto, and E. P. Ippen, IEEE J. Quantum Electron. QE-24, 267 (1988).

[9]E. M. Conwell, in *Solid State Physics*, edited by F. Seitz, D. Turnbull, and H. Ehrenreich (Academic, New York, 1967), Suppl. 9.

[10]R. Ulbrich, Phys. Rev. B 8, 5719 (1973).

[11]E. J. Yoffa, Phys. Rev. B 23, 1909 (1981).

[12]S. M. Kogan, Fiz. Tverd. Tela (Leningrad) 4, 2474 (1963) [Sov. Phys. Solid State 4, 1813 (1963)].

[13]M. Pugnet, J. Collet, and A. Cornet, Solid State Commun. 38, 531 (1981).

[14]J. Collet, A. Cornet, M. Pugnet, and T. Amand, Solid State Commun. 42, 883 (1982); W. Potz and P. Kocevar, Phys. Rev. B 28, 7040 (1982); P. Kocevar, Physica 134B, 155 (1985); S. A. Lyon, J. Lumin. 35, 121 (1986); K. Leo, W. W. Ruhle, and K. Ploog, Phys. Rev. B 38, 1947 (1988).

[15]J. Shah, A. Pinczuk, A. C. Gossard, and W. Wiegmann, Phys. Rev. Lett. 54, 2045 (1985).

[16]*Optical Nonlinearities and Instabilities in Semiconductors*, edited by H. Haug (Academic, New York, 1988).

[17]J. Shah, R. F. Leheny, and C. Lin, Solid State Commun. 18, 1035 (1976); D. H. Auston, S. McAfee, C. V. Shank, E. P. Ippen, and O. Teschke, Solid-State Electron. 21, 147 (1978).

[18]R. Zimmermann, *Many-Particle Theory of Highly Excited Semiconductors* (Teubner, Leipzig, 1988).

[19]Y. Masumoto and F. Sasaki, J. Lumin. 48/49, 189 (1991).

[20]J. B. Stark, W. H. Knox, D. S. Chemla, W. Schäfer, S. Schmitt-Rink, and C. Stafford, Phys. Rev. Lett. 65, 3033 (1990).

[21]L. Schultheis, J. Kuhl, A. Honold, and C. W. Tu, Phys. Rev. Lett. 57, 1635 (1986); L. Schultheis, A. Honold, J. Kuhl, K. Kohler, and C. W. Tu, Phys. Rev. B 34, 9027 (1986); A. Honold, L. Schultheis, J. Kuhl, and C. W. Tu, *ibid.* 40, 6442 (1989).

[22]G. Manzke, K. Henneberger, and V. May, Phys. Status Solidi B 139, 233 (1987).

[23]The energy splitting between the A exciton and B exciton in CdSe is usually about 25 meV. In our sample, energy shifts of both excitons were observed. We consider that the energy shifts are caused by strain between the mica substrate and the CdSe sample.

[24]C. Weisbuch and R. G. Ulbrich, in *Light Scattering in Solid III*, edited by M. Cardona and G. Güntherodt (Springer, Berlin, 1982), Chap. 7.

[25]D. Braun, W. W. Rühle, and J. Collet, in *Ultrafast Phenomena VII* (Ref. 7), p. 271.

Exciton-hole collision in staggered type-II $Al_{0.34}Ga_{0.66}As$/AlAs multiple quantum wells

Tomobumi Mishina and Yasuaki Masumoto
Institute of Physics, University of Tsukuba, Tsukuba, Ibaraki 305, Japan
(Received 6 December 1990; revised manuscript received 19 March 1991)

We report the phase relaxation of Γ-Γ direct excitons in staggered type-II $Al_{0.34}Ga_{0.66}As$/AlAs multiple quantum wells by means of the time-resolved degenerate four-wave mixing. The dephasing rate increases with the increase in the excitation density. Its excitation density dependence sharply changes at a critical density of 0.2 $\mu J/cm^2$. The dependence agrees with the excitation density dependence of the long-lived Γ-hole density studied by means of the pump-and-probe experiment. The long-lived hole density saturates at the same excitation density of 0.2 $\mu J/cm^2$. These facts definitely indicate that the phase relaxation rate of Γ-Γ excitons is dominated by the collision between the excitons and long-lived holes.

Recently, active studies have been carried out on carrier scattering processes in semiconductors by means of ultrafast spectroscopy.[1-3] Above all, the carrier-carrier scattering process in the semiconductor confined system is particularly interesting, because new kinds of boundary conditions are given to the carrier scattering.[2-6] In type-I quantum wells where electrons, holes, and excitons are confined in the same well layer, the collision rates of an exciton with an incoherent exciton and a free carrier (an electron and a hole) were extensively studied. The exciton–free-carrier collision rate was found to be about 8 times larger than the exciton-exciton collision rate.[3,6]

On the other hand, the exciton collision mechanism in the staggered type-II system has not been well studied yet.[7] In staggered type-II $Al_xGa_{1-x}As$/AlAs multiple quantum wells, the conditions are very unique as a result of the interlayer Γ-X scattering process.[8-10] The main feature of the carrier dynamics in the staggered type-II multiple quantum wells is characterized by the rapid Γ-X interlayer scattering and the slow indirect Γ-X recombination.[9-13] The Γ-electron state in the $Al_xGa_{1-x}As$ well layer is located at higher energy than the X-electron state in the AlAs barrier layer. Thus, photoexcited Γ electrons in the well layer are quickly scattered into the X state in the barrier layer within a few picoseconds.[7,9,10-13] The recombination process of Γ holes in the well layer and X electrons in the barrier layer takes place in a microsecond time scale, because of the indirect nature in both the real and momentum space.[10,14-16] The long-lived Γ holes may contribute to the phase relaxation of the Γ-Γ direct excitons in the well.

In this work, we observed the exciton collision process in staggered type-II multiple quantum wells by means of the time-resolved degenerate four-wave mixing. The phase relaxation rate of the Γ-Γ direct excitons increases with the increase in the excitation density and the repetition rates of laser pulses. The excitation density dependence of the phase relaxation rate is represented by a couple of straight lines with a bend at a certain excitation density. The dependence is the same as the excitation density dependence of the long-lived hole density measured by the pump-and-probe transient absorption experiment. The bends are attributable to the saturation of the long-lived hole density. These facts definitely indicate that the collision of the excitons with the long-lived holes generated by the preceding laser pulses is the major collision mechanism.

The samples studied in this experiment were 100 alternate layers of 9.2-nm $Al_{0.34}Ga_{0.66}As$ and 2.7-nm AlAs. The sample was directly immersed in superfluid liquid helium at 2 K. Absorption and luminescence spectra of the sample are shown in our previous paper.[8,10] The lowest-energy heavy-hole exciton peaks at 2.034 eV and is inhomogeneously broadened. The time-resolved degenerate-four-wave-mixing experiment was carried out by using a subpicosecond cavity-dumped dye laser. The photon energy of the laser pulses was resonantly tuned to the absorption peak position of the lowest exciton, 2.034 eV. The spectral width and the temporal width of the laser pulses were about 6 meV and 500 fs, respectively. It is known that the time resolution of the time-resolved four-wave mixing is determined by the inverse of the spectral width.[17] Therefore, our time resolution is about 300 fs corresponding to the laser spectral width of 6 meV. To avoid experimental difficulties keeping the good signal-to-noise ratio, we used the two-pulse configuration in the standard forward-scattering geometry. The arrangement of the experiment is displayed in the inset of Fig. 1. Two laser pulses propagating in the direction of $\mathbf{k}_1$ and $\mathbf{k}_2$, which are parallel polarized to each other, interfere in the sample and generate a grating as long as their time delay $\tau=t_2-t_1$ is of the order of the exciton dephasing time T_2. The second pulse was diffracted by the grating and the signal was generated in the direction $\mathbf{k}_3=2\mathbf{k}_2-\mathbf{k}_1$. In the inhomogeneously broadened two-level system, the optical coherence time T_2 of the system is given by 4τ, where τ is the decay time constant of the time-resolved degenerate-four-wave-mixing signal.[18] In this way, we obtained T_2 of the excitons by measuring the decay time constant τ. The coherence relaxation rate of excitons is an inverse of T_2. When the T_2 is dominated by the lifetime T_1, T_2 is given by $2T_1$. The intensity

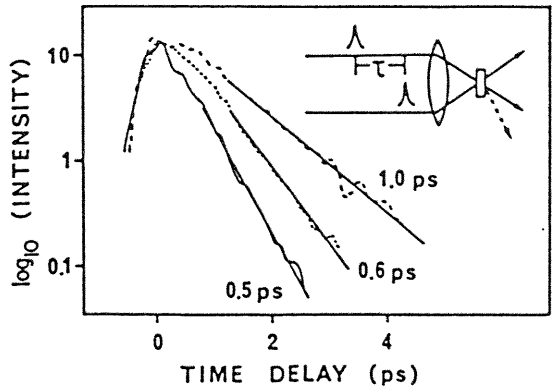

FIG. 1. Typical time traces of the degenerate four-wave mixing at the Γ-Γ exciton transition in $Al_{0.34}Ga_{0.66}As/AlAs$ multiple quantum wells. The repetition rate of the laser pulses is 4.1 MHz. Traces shown by a dashed line, a dotted line, and a solid line correspond to three excitation densities 0.07, 0.22, and 0.63 $\mu J/cm^2$, respectively. Note that the decay time constant becomes short with the increase in the excitation density.

of the second refocusing pulse was always kept at the quarter of the first pulse intensity. The intensities of the two pulses were changed simultaneously. Hereafter, we mean that the excitation density is that of the first pulse.

The typical time traces of the degenerate four-wave mixing for three excitation densities are shown in Fig. 1. The repetition rate of the laser pulses is 4.1 MHz. The excitation densities shown in the figure caption are those of the first pulse. The decay of the signal is single exponential decay. The best fits of the decay curves give the decay time constant of 1.0, 0.6, and 0.5 ps for the traces corresponding to the densities of 0.07, 0.22, and 0.63 $\mu J/cm^2$, respectively. The decay time becomes shorter as the excitation density increases.

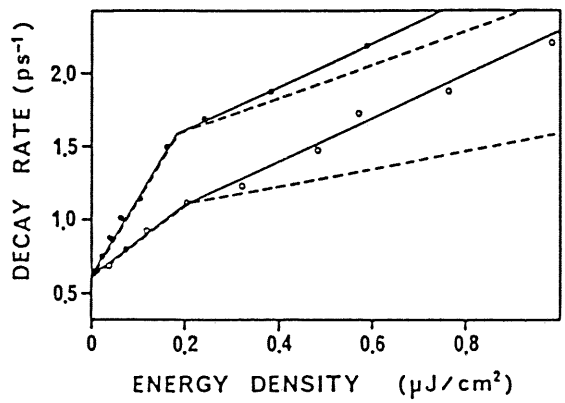

FIG. 2. The plot of the decay rate $1/\tau$ of the degenerate-four-wave-mixing signal vs the excitation density. The vertical scale is equal to $4/T_2$. Closed and open circles correspond to the pulse repetition rates of 4.1 and 0.82 MHz, respectively. There are bends around the excitation density of 0.2 $\mu J/cm^2$. Note that the slopes of the two solid lines are different below the bends and become equal to each other above the bends. Dashed lines are the contribution of the exciton–"old"-hole collision described in the text.

The plots of the decay rate of the signal $1/\tau$ versus the excitation density are displayed in Fig. 2. Two kinds of marks show the data taken at two kinds of repetition rates, 4.1 and 0.82 MHz. They agree with each other at the low-density limit. The low-density limit of the relaxation time is 1.6 ps, which is close to twice that of the Γ-X interlayer scattering time of 1.2 ps.[9] The excitation density dependence of the relaxation rate is represented by a couple of straight solid lines. There are bends around the excitation density of 0.2 $\mu J/cm^2$. Below the bends, the slopes for the two repetition rates are different from each other, while they are equal to each other above the bends. At larger excitation intensity than 0.6 $\mu J/cm^2$, the decay curves of the signal seem to show double exponential decays. In this region, we adopt tentatively the first rapid component as the decay constant. The slow component grows as the excitation density is raised.

To inspect the temporal change of carrier density and its kind, we performed the pump-and-probe transient absorption experiment using the same experimental setup that is used for the time-resolved four-wave mixing. The details of the transient absorption experiment are given in our previous paper.[10] The typical time trace of the transient absorption is shown in Fig. 3. The observed bleaching is attributable to the hole state saturation except at the time origin.[10] The base appearing at the negative time delay is due to the long recombination lifetime of

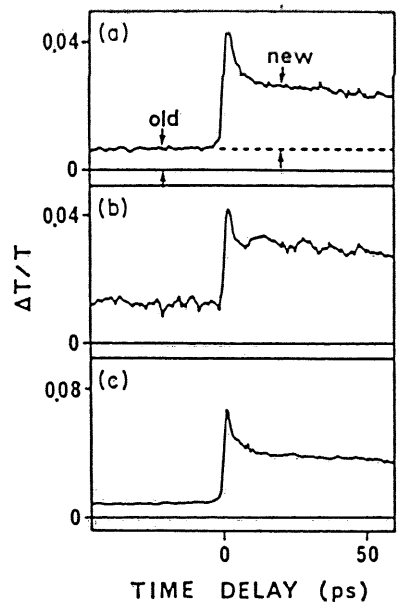

FIG. 3. Typical time traces of the absorption bleaching of the Γ-Γ direct exciton. The energy densities corresponding to (a), (b), and (c) are 0.33, 0.31, and 0.57 $\mu J/cm^2$, respectively. The repetition rates of laser pulses used for (a), (b), and (c) are 0.82, 4.1, and 0.82 MHz, respectively. These bleachings are due to the hole-state saturation and are proportional to the hole density in the well layer as well as the X-electron density in the barrier layer. In (a), "old" and "new" are used to identify the saturation due to the long-lived holes and the saturation due to the holes generated by a single excitation pulse. The rapid decay around the time origin is caused by the fast Γ-X interlayer scattering of electrons.

the X-Γ electron-hole pairs. The lifetime is longer than the present pulse-repetition intervals, 240 ns and 1.2 μs. It is not ascribed to the Γ-Γ exciton population, because the lifetime of the Γ-Γ exciton is less than 10 ps. Therefore, the base is proportional to the unrecombined long-lived hole density created by the preceding pulses.[10] We call the long-lived hole the "old" hole. The transient absorption shows a peak and a fast decay around the zero time delay. The peak is simply ascribed to the Γ-Γ exciton bleaching due to the creation of the Γ-Γ excitons. The fast decay corresponds to the interlayer Γ-X scattering of electrons.[9,10] The transient absorption shows a plateau after the fast decay finishes. It is ascribed to the newly created hole density generated as a result of the dissociation of excitons and the interlayer Γ-X scattering of electrons. We call these holes "new" holes.

Figure 3 shows that the "old" hole density increases with the increase in the excitation density and the repetition rate of laser pulses. The plot of the "old" hole density and the "new" hole density versus the excitation density is depicted in Fig. 4. Again, we plotted the data taken at two kinds of laser repetition rates, 4.1 and 0.82 MHz. With the increase in the excitation density, the "old" hole density increases with sharp bends around the critical excitation density of 0.2 μJ/cm^2. The "old" hole density almost saturates under the excitation density of 0.2 μJ/cm^2. The saturated value for the 4.1-MHz repetition rate is larger than that for the 0.82-MHz repetition rate. The difference is ascribed to the slow recombination of Γ holes and X electrons. The slopes are different below the critical density. The difference means that the "old" hole density decreases during 960 ns, which is equal to 1.2 μs$-$240 ns. On the other hand, the "new" hole density increases nearly in proportion to the excitation density regardless of the laser repetition rate.

Excitation intensity dependence of the dephasing rate of Γ-Γ excitons and that of the "old" hole density are well related to each other. The change appears at the same excitation density of 0.2 μJ/cm^2, as shown in Figs. 2 and 4. The similar excitation density dependence definitely indicates that the excitons dephase mainly through the collision between excitons and "old" holes. As a result of the interlayer Γ-X scattering, Γ-Γ excitons are dissociated into the X electrons in the barrier layer and the Γ holes in the well layer. The Γ holes are alive for a long time. They collide strongly with newly generated excitons. This is the main dephasing mechanism of the Γ-Γ excitons. One may consider that "new" holes should contribute to the exciton-hole collision process. However, "new" holes are created as a result of the dissociation of excitons. Therefore "new" holes have little chance to collide with excitons.

The bends that appeared around the excitation density of 0.2 μJ/cm^2 are explained by the saturation of the density of long-lived holes. The saturation of the long-lived "old" holes does not mean the saturation of the X-state or the inhibition of the Γ-X scattering, because "new" holes do not saturate. The recombination of Γ holes and X electrons is nonexponential, and some electron-hole pairs can recombine rapidly depending on the pair density. Therefore, the long-lived "old" hole density can be saturated without the saturation of "new" hole density. The density-dependent carrier diffusion may also contribute to the saturation of the long-lived "old" hole density.

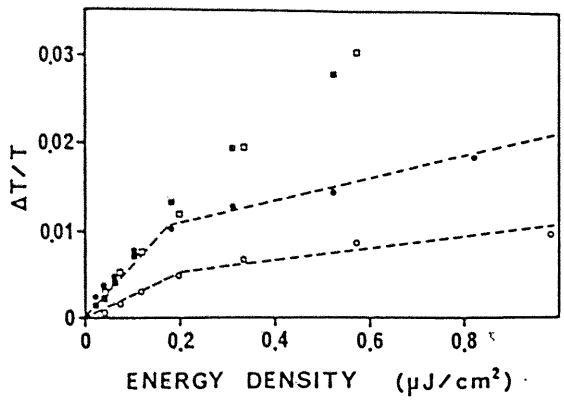

FIG. 4. The plot of the bleaching ascribed to the hole density vs the excitation density. Closed and open circles show the bleaching due to the "old" holes and correspond to the pulse repetition rates of 4.1 and 0.82 MHz, respectively. Closed and open squares are the saturations due to the "new" holes and correspond to the pulse repetition rates of 4.1 and 0.82 MHz, respectively. There is a saturation point for the "old" hole density around the excitation density of 0.2 μJ/cm^2.

It is useful to compare our result for the type-II system with the result for the type-I system. The experimental result reported by Honold *et al.* for a type-I GaAs single quantum well is as follows.[6] The excitation density dependence of the dephasing rate of the lowest-energy exciton is determined by the exciton–free-carrier and exciton-exciton collisions. The dephasing rate is written by $1/T_2 = A + B\,N$, where A is a constant independent of the carrier density, N is a density of excitons or free carriers in units of 10^{10} cm^{-2}, and B is 0.087 ps^{-1} for the exciton-exciton collision or 0.67 ps^{-1} for the exciton–free-carrier collision. To compare our result with the result mentioned above, we estimated the created exciton density. The excitation density of 1 μJ/cm^2 corresponds to the sheet exciton density of 2.6×10^{10} cm^{-2} by using the optical density of 0.82 at the exciton absorption peak. Figure 4 informs us of the excitation density dependence of "old" and "new" hole densities, because an exciton is converted to a "new" hole and because a "new" hole and an "old" hole contribute to the same amount of absorption bleaching. Using the value of $B = 0.51$ ps^{-1} for the exciton–"old"-hole collision, we estimated the contribution of the exciton–"old"-hole collision to the observed decay rate, shown by dashed lines in Fig. 2. We can explain the data of Fig. 2. The value of B for the exciton–"old"-hole collision almost agrees with that for the exciton–free-carrier collision in the type-I system. However, the additional collision mechanism must be taken into account above the bends. The value of B for the additional collision is 0.033–0.084 ps^{-1}. It is probably the exciton-exciton collision or the exciton–"new"-hole collision. If the exciton-exciton collision works, the value of B almost agrees with that for the exciton-exciton collision in the type-I system. The

growth of the slow component in the degenerate-four-wave-mixing signal under the higher excitation density may be explained in this picture.

In conclusion, we studied the exciton collision processes in type-II multiple quantum wells by means of the time-resolved four-wave mixing and the pump-and-probe transient absorption. The exciton dephasing rate increases with the increase in the excitation density and the repetition rate of laser pulses. We found that the collision rate of the Γ-Γ exciton strongly depends on the dissociated long-lived hole density created by the preceding laser pulses. This result indicates that the dephasing of the Γ-Γ exciton is dominated by the collision between excitons and long-lived holes.

[1]P. C. Becker, H. L. Fragnito, C. H. Brito Cruz, R. L. Fork, J. E. Cunningham, J. E. Henry, and C. V. Shank, Phys. Rev. Lett. 61, 1647 (1988).

[2]W. H. Knox, D. S. Chemla, G. Livescu, J. E. Cunningham, and J. E. Henry, Phys. Rev. Lett. 61, 1290 (1988).

[3]L. Schultheis, J. Kuhl, A. Honold, and C. W. Tu, Phys. Rev. Lett. 57, 1635 (1986).

[4]K. Leo, M. Wegener, J. Shah, D. S. Chemla, E. O. Göbel, T. C. Damen, S. Schmitt-Rink, and W. Schäfer, Phys. Rev. Lett. 65, 1340 (1990).

[5]L. Schultheis, A. Honold, J. Kuhl, K. Köhler, and C. W. Tu, Phys. Rev. B 34, 9027 (1986).

[6]A. Honold, L. Schultheis, J. Kuhl, and C. W. Tu, Phys. Rev. B 40, 6442 (1989).

[7]T. Mishina, F. Sasaki, and Y. Masumoto, *Ultrafast Phenomena VII* (Springer, Berlin, 1990), p. 268.

[8]Y. Masumoto and T. Tsuchiya, J. Phys. Soc. Jpn. 57, 4403 (1988).

[9]Yasuaki Masumoto, Tomobumi Mishina, Fumio Sasaki, and Mitsuhiro Adachi, Phys. Rev. B 40, 8581 (1989).

[10]T. Mishina, F. Sasaki, and Y. Masumoto, J. Phys. Soc. Jpn. 59, 2635 (1990).

[11]P. Saeta, J. F. Federici, R. J. Fischer, B. I. Greene, L. Pfeiffer, R. C. Spitzer, and B. A. Wilson, Appl. Phys. Lett. 54, 1681 (1989).

[12]J. Feldmann, R. Sattmann, E. O. Göbel, J. Kuhl, J. Hebling, K. Ploog, R. Muralidharan, P. Dawson, and C. T. Foxon, Phys. Rev. Lett. 62, 1892 (1989).

[13]J. Feldmann, J. Nunnenkamp, G. Peter, E. Göbel, J. Kuhl, K. Ploog, P. Dawson, and C. T. Foxon, Phys. Rev. B 42, 5809 (1990).

[14]E. Finkman, M. D. Sturge, M.-H. Meynadier, R. E. Nahory, M. C. Tamargo, D. M. Hwang, and C. C. Chang, J. Lumin. 39, 57 (1987).

[15]F. Minami, K. Hirata, K. Era, T. Yao, and Y. Masumoto, Phys. Rev. B 36, 2875 (1987).

[16]B. A. Wilson, C. E. Bonner, R. C. Spitzer, R. Fischer, P. Dawson, K. J. Moore, C. T. Foxon, and G.W. 't Hooft, Phys. Rev. B 40, 1825 (1989).

[17]S. Asaka, H. Nakatsuka, M. Fujiwara, and M. Matsuoka, Phys. Rev. A 29, 2286 (1984).

[18]T. Yajima and Y. Taira, J. Phys. Soc. Jpn. 47, 1620 (1979).

Spin-relaxation process of holes in type-II $Al_{0.34}Ga_{0.66}As/AlAs$ multiple quantum wells

Tadashi Kawazoe, Yasuaki Masumoto, and Tomobumi Mishina
Institute of Physics, University of Tsukuba, Tsukuba, Ibaraki 305, Japan
(Received 24 August 1992)

We have measured the spin memory and the spin-relaxation times of holes in type-II quantum wells by means of pump-and-probe methods. The fast Γ-X interlayer scattering which is characteristic of type-II multiple quantum wells allows us to observe directly the hole spin-relaxation process. The hole spin relaxation is described by two decay components. The faster decay time ranges from 20 to 100 ps and depends on the number density of "antiparallel-spin" holes. This indicates that the scattering between up-spin holes and down-spin holes is the major spin-relaxation process of holes. The slower time component is about 20 ns, which is probably ascribed to the spin relaxation of localized holes in the well layers.
PACS number(s): 73.20.Dx, 78.66.Fd, 78.47.+p

The spin-relaxation process of carriers in semiconductors has been extensively studied by means of static luminescence polarization measurements. Such measurements have informed us of spin-relaxation mechanisms of carriers in bulk semiconductors.[1] Today, ultrafast laser spectroscopy is used to observe directly the time-resolved polarization.[2–10] Recently the time-resolved polarization measurement is often applied to GaAs quantum wells.[2–4,7–10] In quantum wells, two-dimensionality splits the degenerate valence bands into heavy- and light-hole bands whose total angular momenta are $\frac{3}{2}$ and $\frac{1}{2}$, respectively. As a result of the nondegeneracy, spin-relaxation processes of holes in quantum wells are quite different from those in bulk crystals and are studied intensively.[11,12]

Time-resolved luminescence polarization experiments were done in type-II as well as type-I GaAs quantum wells. Kohl *et al.* observed that the electron spin-relaxation time is 150 ps in good quality type-I GaAs $Al_xGa_{1-x}As$ quantum wells at 10 K.[7] In short-period type-II GaAs/AlAs quantum wells, van der Poel *et al.* reported that hole spin memory remains longer than the lifetime of carriers, 7 μs, at 1.7 K.[2,3] The polarized luminescence comes from the radiative recombination of spin-polarized electrons and holes. Therefore, it is not clear which are polarized, electrons or holes. To overcome this difficulty, Damen *et al.* measured the spin-relaxation time of electrons and holes individually by using p- and n-doped $GaAs/Al_{0.3}Ga_{0.7}As$ type-I multiple quantum wells.[9] The obtained spin-relaxation times of electrons and holes are 150 and 4 ps, respectively. The pump-and-probe technique is also applied to the time-resolved studies of spin relaxation of electrons and holes. Bar-Ad and Bar-Joseph measured the spin relaxation of carriers in the $GaAs/Al_xGa_{1-x}As$ type-I quantum wells.[10] They observed two decay times, 120 and 50 ps. They ascribed 120 ps to the spin-relaxation time of electrons and 50 ps to that of holes.

We measured the spin-relaxation processes of holes in type-II $Al_{0.34}Ga_{0.66}As/AlAs$ multiple quantum wells by means of the pump-and-probe method. In a type-II sample, photogenerated electrons are quickly scattered to the barriers, so that holes alone remain in the wells.[13–17] The pump-and-probe method is applicable to the observation of hole states. In fact, the experimental results give unique information about the hole spin relaxation. We can observe how to relax the spin polarization of the nondegenerate holes in this two-dimensional system in detail. The hole spin-relaxation time ranges from 20 to 100 ps, depending on the excitation intensity. We also observed that 10% spin memory is still conserved for an order of a nanosecond.

We can observe directly the spin relaxation of holes in type-II quantum-well structures. Figure 1(a) shows the electronic energy levels of the $Al_{0.34}Ga_{0.66}As/AlAs$ type-II quantum-well structures. Both the bottom of the con-

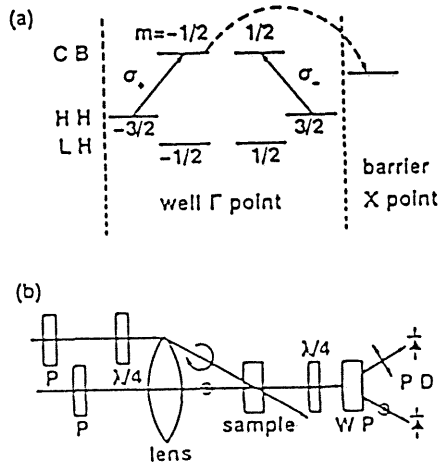

FIG. 1. (a) Optical transitions and interlayer electron transfer for type-II $Al_{0.34}Ga_{0.66}As/AlAs$ quantum wells with circularly polarized light. σ_+ and σ_- stand for right and left circularly polarized light, respectively. Electrons at Γ points in wells transfer to the X points in barriers. As a result, holes alone remain in the wells. (b) Experimental setup of the pump-and-probe method: P, polarizer; $\lambda/4$, quarter-wave plate; WP, Wollaston prism; PD, photodiode. Arrows denote polarization of light.

duction and the top of the valence band in the $Al_{0.34}Ga_{0.66}As$ well are at the Γ point in the Brillouin zone. The Γ-point bottom of the conduction band is linked to the X point in the AlAs barrier by the interlayer intervalley scattering of electrons. σ_+ and σ_- denote right circularly polarized light and left circularly polarized light, respectively. The arrows in Fig. 1(a) indicate the allowed transitions induced by σ_+ and σ_-.

When the right circularly polarized light hits the heavy-hole absorption edge, the electrons at the $-\frac{1}{2}$ state and the holes at the $-\frac{3}{2}$ state are generated. As a result of the Γ-X interlayer scattering, Γ electrons whose spin angular momentum is $-\frac{1}{2}$ are scattered to the X point in the barriers. The mean scattering time is less than a few picoseconds.[13] After electrons at the $-\frac{1}{2}$ state are scattered to the X point in barriers, holes at the $-\frac{3}{2}$ state alone are left in the well. Therefore, we can measure the spin relaxation of holes by observing the hole density at the states $-\frac{3}{2}$ and $\frac{3}{2}$ which are probed by right and left circularly polarized light, respectively.

Figure 1(b) shows the experimental setup. A quarter-wave plate transforms the linearly polarized pump beam into circularly polarized light. The probe beam is the linearly polarized light which is the sum of an equal amount of right circularly polarized light and left circularly polarized light. The probe beam transmitted through the sample goes through another quarter-wave plate. The right circularly polarized light component turns to the vertically linearly polarized light and the left circularly polarized light to the horizontally linearly polarized light. Two linearly polarized lights are separated by a Wollaston prism and are detected by two photodiodes whose sensitivities are equal to each other. The obtained signals, I_+ and I_-, are proportional to the differential transmittance of the right and the left circularly polarized light, respectively. Namely, I_+ is proportional to the hole density at the $-\frac{3}{2}$ state and I_- is proportional to that at the $\frac{3}{2}$ state. In addition, a simple differential electronic circuit is used to obtain the signal $I_+ - I_-$ corresponding to the spin polarization. In this way, we can take very weak spin memory signals that are not usually detectable. A detectable degree of polarization is as small as 0.1%. The advantage of this method comes from the cancellation of the temporal fluctuations of laser power, because I_+ and I_- are measured simultaneously.

The sample used in this investigation is 100 periods of 9.2-nm $Al_{0.34}Ga_{0.66}As$ and 2.7-nm AlAs layers which form type-II ternary alloy multiple-quantum-well structures. A fundamental optical characterization of the sample and its ultrafast laser spectroscopy were reported in our previous publications.[13,17,13] The sample was directly immersed in superfluid helium and was measured at 2 K. We used the same cavity-dumped synchronously pumped dye laser system that was used in our previous study.[13-20] The temporal width of laser pulses was 1 ps. The repetition rate was varied to be 406 kHz, 812 kHz, and 4.06 MHz.

Figure 2 shows an experimental result. The excitation density is 0.07 $\mu J/cm^2$ corresponding to the sheet carrier density of $2.1\times10^9/cm^2$. The laser repetition rate is 812 kHz. The inset shows the excitation photon energy and the absorption spectrum of the sample, indicating that the excitation photon energy corresponds to the absorption edge of the heavy-hole exciton. Both I_+ and I_- signals show a sharp structure at the beginning. The initial sharp structure in the I_- signal is ascribed to the coherent artifact. The initial sharp structure in the I_+ signal is the exciton bleaching plus the coherent artifact. As a result of interlayer intervalley scattering of electrons, exciton bleaching decays at a time constant of 2.5 ps and hole bleaching remains for a long time. After 10 ps, I_- decreases slowly, while I_+ increases at almost the same rate. This means that the holes created at the state $-\frac{3}{2}$ relax to the state $\frac{3}{2}$. Even after 1 μs, the I_+ signal is not zero but is equal to I_-. Because the hole lifetime in this sample is an order of a microsecond,[18] and because the pulse-to-pulse interval is 1.2 μs, the absorption bleaching still remains at the negative time delay. The result shows that the spin memory is completely lost in μs, while the holes still remained in the wells. This means that the hole lifetime is much longer than the spin-relaxation time.

Figure 2(b) shows the logarithmic plot of $I_+ - I_-$. We can consider that $I_+ - I_-$ is proportional to degree of polarization because the relaxation time of $I_+ + I_-$ is of μs order. After 10 ps, the signal decays exponentially at a time constant of 67 ps. At this time region, there are

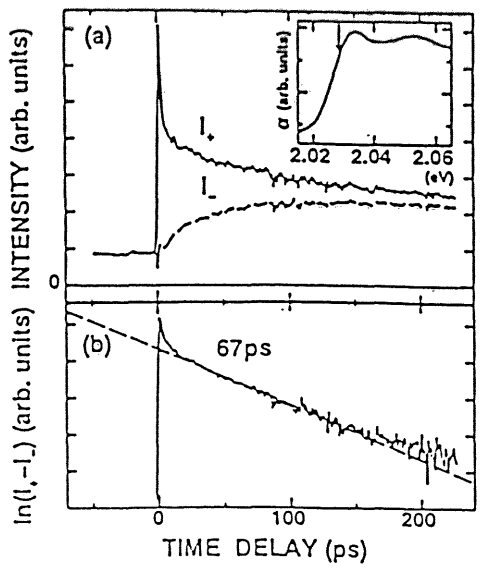

FIG. 2. (a) The differential transmission signals observed under the pump of the right circularly polarized light. The pump density is 0.07 $\mu J/cm^2$. The laser repetition rate is 812 kHz. The solid line shows the differential transmission signal of the right circularly polarized probe light. The dashed line shows the differential transmission signal of the left circularly polarized probe light. The inset shows the absorption spectrum of the $Al_{0.34}Ga_{0.66}As$/AlAs multiple quantum wells with arrowed excitation photon energy. (b) The logarithmic plot of $I_+ - I_-$. The decay of $I_+ - I_-$ is fitted by single exponential decay (dashed line).

no electrons in the well as a result of the Γ-X interlayer scattering. Therefore, the time constant of 67 ps means the spin-relaxation time of holes. Furthermore, we observed the dependence of the relaxation time of holes on the excitation density.

The hole spin-relaxation time depends upon the excitation density and ranges from 20 to 100 ps. Figure 3 shows the temporal change of $I_+ - I_-$ at three excitation densities. The relaxation time becomes shorter with an increase in excitation density. The hole spin-relaxation time becomes faster as the excitation density increases. We also measured $I_+ - I_-$ for the long-time scale. We observed that a 10% spin memory is still conserved for an order of a nanosecond. The results show that spin relaxation has another slow decay time component whose time constant is about 20 ns. Similar slow decay is observed in the Γ-X luminescence of short-period type-II GaAs/AlAs quantum wells by van der Poel *et al.*[2,3]

The fast decay component depends not only on the excitation density but also on the repetition rate of the laser pulses. In a previous work, we clarified that the lifetime of holes in the well layer is as long as an order of a microsecond in a type-II $Al_{0.34}Ga_{0.66}As$/AlAs sample.[18] The long lifetime of holes forms a base signal at the negative time delay in the temporal trace of the pump-and-probe experiment, which is proportional to the number density of accumulated holes. When the right circularly polarized light hits the heavy-hole absorption edge, the electrons at the $-\frac{1}{2}$ state and the holes at the $-\frac{3}{2}$ state are generated. After the photoexcitation, generated holes coexist with holes generated by the previous pulses, because the inverse of the repetition rate of the laser is comparable to the lifetime of holes. Holes generated by the previous pulses lose the spin memory completely and half of them are at the $\frac{3}{2}$ state. We call the holes at the $\frac{3}{2}$ state "antiparallel-spin" holes. We also call the holes at the $-\frac{3}{2}$ state "parallel-spin" holes.

We plotted the spin-relaxation rate of holes as a function of number density of antiparallel-spin holes. The number density of antiparallel-spin holes is proportional to the bleaching signal taken by left circularly polarized light. Differential transmittance of 1% due to the bleaching of the hole state corresponds to the hole number density of $2.2\times10^9/cm^2$ which is calibrated at the excitation density of 0.1 $\mu J/cm^2$. Therefore, the number densities of antiparallel-spin holes are obtained from the bleaching signal of I_- at 10 ps. The result is shown in Fig. 4. Data include the results taken at three different repetition rates, 406 kHz, 812 kHz, and 4.06 MHz. Changing the repetition rate corresponds to changing the equal number densities of "parallel-spin" holes and "antiparallel-spin" holes, while changing the excitation density corresponds to changing mainly the number density of parallel-spin holes.

The relation is well written by a straight line, that is, $1/\tau = A + BN$, where $1/\tau$ is the spin-relaxation rate, A is 0.0054 ps^{-1}, B is 0.084×10^{-10} $ps^{-1}cm^2$ and N is the sheet number density of antiparallel-spin holes. The spin-relaxation rate of holes is proportional to the number density of holes which have an opposite spin. Another plot of the spin-relaxation rate of holes as a function of total number density of holes gives the scattering of data. The experimental result definitely shows that the hole-hole collision dominates the spin-relaxation mechanism of holes and that up-spin holes selectively collide with down-spin holes.

Collisions of two identical particles are discussed in quantum mechanics.[21] The identity of the particles leads to the symmetric or antisymmetric orbital wave function of the system, according to whether their spins are antiparallel or parallel to each other. The scattering cross section of two holes are represented by $d\sigma_\pm = |f(\theta) \pm f(\pi-\theta)|^2 d\sigma$, when the spins of the holes are antiparallel to each other. Here, $f(\theta)$ is a part of the outgoing wave function $f(\theta)e^{ikr}/r$ from the scattering center, and $d\sigma$ is an element of the solid angle. On the

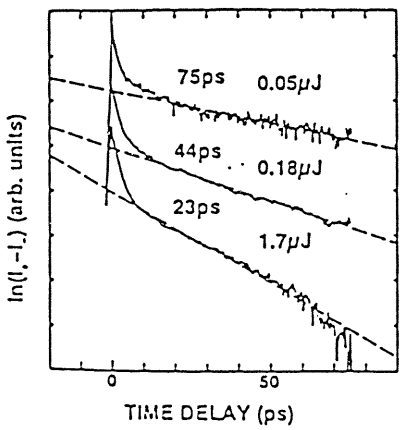

FIG. 3. The logarithmic plot of $I_+ - I_-$ for three excitation densities. Three decay curves of $I_+ - I_-$ are fitted by single exponential decay (dashed lines).

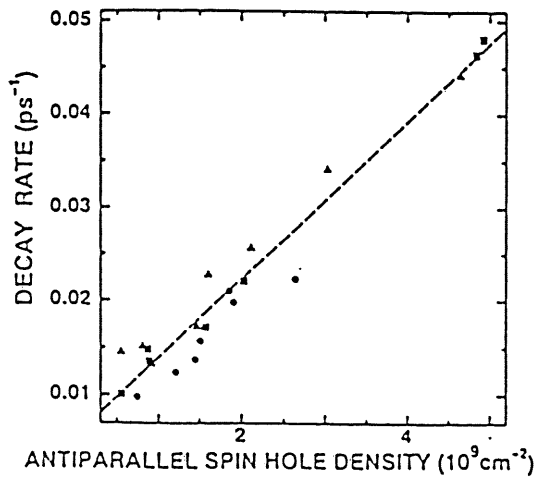

FIG. 4. The plot of the hole spin-relaxation rate as a function of the "antiparallel-spin" hole density. A dashed line is the fitted line $1/\tau = A + BN$; N is a sheet number density of "antiparallel-spin" hole, A is 0.0054 ps^{-1}, and B is 0.084×10^{-10} $ps^{-1}cm^2$. The solid squares, solid triangles, and solid circles correspond to the data taken at the repetition rates of 406 kHz, 812 kHz, and 4.06 MHz, respectively.

other hand, the scattering cross section of two holes is described by $d\sigma_a=|f(\theta)-f(\pi-\theta)|^2\,d\sigma$, when the spins of the holes are parallel to each other. The two-dimensional Coulomb scattering cross section is analytically obtained.[22] However, we cannot find that $d\sigma_s$ is much larger than $d\sigma_a$.[23] If hole wave vector is small compared with the radius of action of the scattering potential, $f(\theta)$ is constant.[21] This situation corresponds to the scattering of rigid spheres. Then, $d\sigma_a$ is zero, but $d\sigma_s$ is finite. This means that antiparallel-spin holes are scattered to each other, but that parallel-spin holes are not scattered to each other. The two-dimensional screened Coulomb potential is proportional to $1/r^3$ and the condition of slow particle scattering can be satisfied in this case.[21,24] Therefore, the two-dimensional screened Coulomb scattering may explain the reason why antiparallel-spin holes are mutually scattered much more than parallel-spin holes. Further theoretical investigation is needed to explain the experimental results.

In III-V semiconductors, valence-hole states are characterized by mixture of orbital angular momentum of $j=1$ and spin angular momentum of $s=\frac{1}{2}$. In quantum wells, subband mixing takes place further. As a result, spin is not the good quantum number. Therefore, change in the wave vector of holes caused by hole scattering brings about the change in the spin state.[11,12] In the slower time domain, holes are considered to be localized at the interface fluctuation. Holes scarcely collide with each other. The spin-relaxation time then becomes slower. We think localization of holes is responsible for this slow spin-relaxation time of 20 ns.

In summary, we measured the spin-relaxation time of holes in type-II $Al_{0.66}Ga_{0.34}As/AlAs$ multiple quantum wells by means of the pump-and-probe technique. Spin relaxation of holes is described by fast and slow relaxation rates. The fast spin-relaxation time of holes ranges from 20 to 100 ps and depends on the antiparallel-spin hole density. The fast spin relaxation of holes is caused by hole-hole collision. The slow spin-relaxation time of holes is about 20 ns. Slow spin relaxation is probably ascribed to the localization of holes.

This work was supported by a Scientific Research Grant-in-Aid No. 04228202 for Scientific Research on a Priority Area—Ultrafast and Ultraparallel Optoelectronics—by the Ministry of Education, Science and Culture of Japan.

[1] *Optical Orientation*, edited by F. Meier and B. P. Zakharchenya (North Holland, Amsterdam, 1984).
[2] W. A. J. A. van der Poel, A. L. G. J. Severens, H. W. van Kesteren, and C. T. Foxon, Phys. Rev. B 39, 8552 (1989).
[3] W. A. J. A. van der Poel, A. L. G. J. Severens, H. W. van Kesteren, and C. T. Foxon, Superlatt. Microstruc. 5, 115 (1989).
[4] A. Tackeuchi, S. Muto, T. Inata, and T. Fujii, Appl. Phys. Lett. 56, 2213 (1990).
[5] M. R. Freeman, D. D. Awschalom, J. M. Hong, and L. L. Chang, Phys. Rev. Lett. 64, 2430 (1990).
[6] M. R. Freeman and D. D. Awschalom, J. Appl. Phys. 67, 5102 (1990).
[7] M. Kohl, M. R. Freeman, D. D. Awschalom, and J. M. Hong, Phys. Rev. B 44, 5923 (1991).
[8] T. C. Damen, Karl Leo, Jagdeep Shah, and J. E. Cunningham, Appl. Phys. Lett. 58, 1902 (1991).
[9] T. C. Damen, Luis Viña, J. E. Cunningham, Jagdeep Shah, and L. J. Sham, Phys. Rev. Lett. 67, 3432 (1991).
[10] S. Bar-Ad and I. Bar-Joseph, Phys. Rev. Lett. 68, 349 (1992).
[11] T. Uenoyama and L. J. Sham, Phys. Rev. Lett. 64, 3070 (1990).
[12] T. Uenoyama and L. J. Sham, Phys. Rev. B 42, 7114 (1990).
[13] Y. Masumoto, T. Mishina, F. Sasaki, and M. Adachi, Phys. Rev. B 40, 8581 (1989).
[14] J. Feldmann, R. Sattmann, E. O. Göbel, J. Kuhl, J. Hebling, K. Ploog, R. Muralidharan, P. Dawson, and C. T. Foxon, Phys. Rev. Lett. 62, 1892 (1989).
[15] J. Feldmann, J. Nunnenkamp, G. Peter, E. Göbel, J. Kuhl, K. Ploog, P. Dawson, and C. T. Foxon, Phys. Rev. B 42, 5809 (1990).
[16] P. Saeta, J. F. Federici, R. J. Fischer, B. I. Greene, L. Pfeiffer, R. C. Spitzer, and B. A. Wilson, Appl. Phys. Lett. 54, 1681 (1989).
[17] Y. Masumoto and T. Tsuchiya, J. Phys. Soc. Jpn. 57, 4403 (1988).
[18] T. Mishina, F. Sasaki, and Y. Masumoto, J. Phys. Soc. Jpn. 59, 2635 (1990).
[19] T. Mishina and Y. Masumoto, Phys. Rev. B 44, 5664 (1991).
[20] T. Mishina and Y. Masumoto, Jpn. J. Appl. Phys. 31, L343 (1992).
[21] L. D. Landau and E. M. Lifshitz, *Quantum Mechanics (Non-relativistic Theory)* (Pergamon, Oxford, 1977).
[22] F. Stern and W. E. Howard, Phys. Rev. 163, 816 (1967).
[23] Two-dimensional Coulomb scattering cross section for identical holes is derived as $\sigma_s=(G/2k)\tanh(\pi G)(1/\sin^2(\theta/2)+\cos^2(\theta/2)+\cos[2G\ln[\tan(\theta/2)]]/\sin(\theta/2)\cos(\theta/2))$ and $\sigma_a=(G/2k)\tanh(\pi G)(1/\sin^2(\theta/2)+1/\cos^2(\theta/2)-\cos[2G\ln[\tan(\theta/2)]]/\sin(\theta/2)\cos(\theta/2))$, where G is defined by $1/a^*k$. Here a^* is the effective Bohr radius and k is the wave vector of holes.
[24] T. Ando, A. B. Fowler, and F. Stern, Rev. Mod. Phys. 54, 437 (1982).

Observation of coherent optical phonons in BiI_3

T. Mishina and Y. Masumoto
Institute of Physics, University of Tsukuba, Tsukuba, Ibaraki 305, Japan

B. Fluegel, K. Meissner, and N. Peyghambarian
Optical Sciences Center, University of Arizona, Tuscon, Arizona 85721
(Received 29 October 1991; revised manuscript received 11 March 1992)

Resonant coherent lattice vibrations in the vicinity of the indirect absorption edge in a BiI_3 layered crystal are observed in a femtosecond pump-probe experiment. Coherent optical phonons that are impulsively excited by femtosecond pump pulses modulate the phase of probe pulses, causing oscillation of the probe spectrum in time. This oscillation, which has a period given by the period of the oscillation, continues for more than 100 cycles. We speculate that the coherent phonon-assisted indirect exciton transitions also contribute to the data.

Progress in ultrafast laser techniques has enabled direct observation of the coherent response of phonons and excitons. Coherent phonons can be impulsively generated by laser pulses whose temporal widths are shorter than the period of phonon oscillation.[1] The coherent phonon state is a coherent superposition of various number states of the relevant phonon mode. As excess numbers of phonons are populated in particular modes, the coherent phonon state is far from thermal equilibrium. By using ultrafast time-resolved techniques, coherent lattice vibrations and their damping have been directly observed in various materials.[1-4]

In this paper, we report the observation of ultrafast phase modulation caused by coherent phonon excitation in layered BiI_3. BiI_3 belongs to a family of layered metal halides[5] consisting of strongly bonded two-dimensional layers with weak Van der Waals interlayer coupling. The structure gives the rigid-layer mode of lattice vibration,[6] which is expected to continue for a long time because of its low-energy oscillation and small damping. The optical-absorption edge of BiI_3 is characterized by phonon-assisted indirect exciton transitions and very sharp exciton peaks, called the direct R, S, and T excitons, due to stacking disorders in the crystal.[5-8] The indirect transition is that from the Γ point of the valence band to the Z point at the zone boundary of the conduction band. Both the direct as well as the indirect optical transitions may be affected by the coherent phonon oscillation. Thus, BiI_3 is a unique material for studying the interaction between coherent lattice vibrations and excitonic transitions. The R, S, T, and the indirect exciton energies are located around 2 eV and are easily excited by available femtosecond dye lasers.

Our sample, with a thickness of $\simeq 10$ μm, was grown by the sublimation method, under conditions of excess iodine in the gas phase. Figure 1 shows the absorption spectrum of the sample at 10 K. The R, S, and T exciton absorption lines appear close to the fundamental absorption edge, as expected. The energy position of the indirect exciton is labeled E_{gx}^{i} in Fig. 1.

The Arizona laser system used in the experiment is composed of a balance colliding-pulse mode-locked laser and a six-pass dye amplifier pumped by a copper-vapor laser operating at 8.4 kHz. The temporal width of amplified output pulses was 64 fs after compensation of group-velocity dispersion by a double prism pair. The spectrum of the amplified pulses is centered at 1.99 eV and entirely covers the absorption lines of the R, S, and T stacking-fault excitons, as shown in Fig. 1. The orthogonally polarized pump and probe pulses cross at the sample at an angle of about 20°.

In Fig. 2 the temporal traces of the absorption change at 10 K for four spectral positions are shown. The energy density of the pump pulses is about 850 μJ/cm^2, 30% of which is absorbed by the sample. Traces for the R, S, and T excitons all show a rise at negative time delays and temporal oscillatory structure superimposed on the long-lasting bleaching component. The trace taken at the

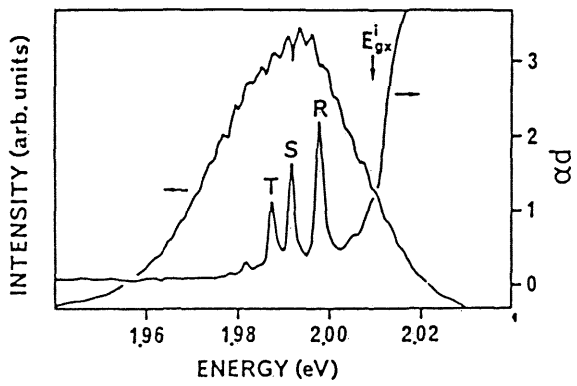

FIG. 1. Absorption spectrum of the BiI_3 sample and the spectrum of the amplified laser pulses are shown. αd denotes the absorption coefficient α multiplied by sample thickness d. The laser spectrum entirely covers the R, S, and T exciton lines and the indirect exciton region. The indirect exciton energy is denoted by E_{gx}^{i}.

transparent region of the sample (1.97 eV) shows the temporal oscillation without bleaching. Furthermore, there is a phase shift between the oscillation observed in the four traces of Fig. 2, as evidenced by the vertical lines labeled *a* and *b*. The transmitted probe spectra taken for two time delays, shown by *a* and *b*, are displayed in the inset of Fig. 2. The spectral positions for the four temporal traces of Fig. 2 are marked by the arrows in the inset of Fig. 2. The transmission minima in the inset correspond to the *R*, *S*, and *T* excitons. While the exciton positions show no shift, the envelope of the transmitted spectrum clearly exhibits temporal oscillation. The oscillations of the probe spectrum are unambiguously seen in the temporal behavior of the differential signal in the transparent region (1.97 eV).

The negative time-delay signals observed for excitons in Fig. 2 are related to the optical coherence time T_2 of the excitons.[9] It can be simply explained by noting that the transmitted intensity of the probe pulse is detected by a time-integrating detector. The polarization generated by the probe pulse in the sample persists for the optical coherence time T_2 and is affected by the pump pulse that arrives at the sample after the probe pulse.

Figure 3(a) shows absorption changes at several negative time delays where the well-known spectral oscillatory structures around the *R*, *S*, and *T* excitons are observed.[9]

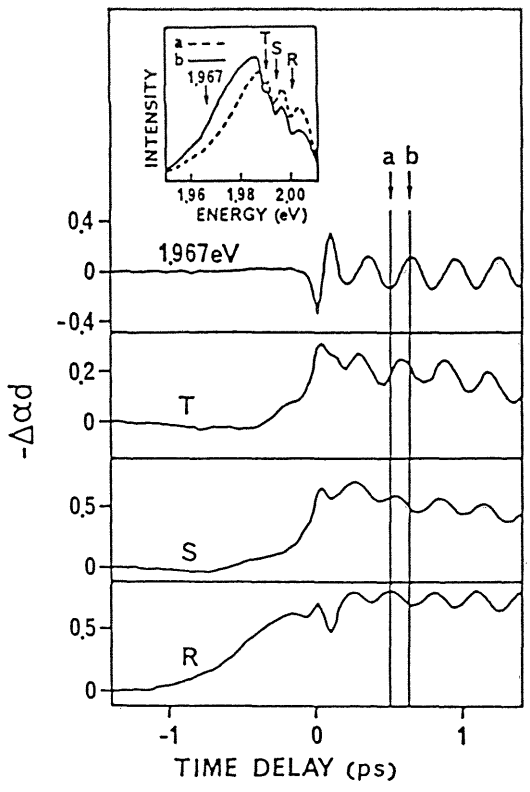

FIG. 2. Temporal traces of absorption change at four spectral positions, the *R*, *S*, and *T* excitons and transparent region 1.97 eV. The spectrum of the transmitted probe beam at two time delays *a* and *b* are displayed in the inset. Apparent spectral shift can be seen.

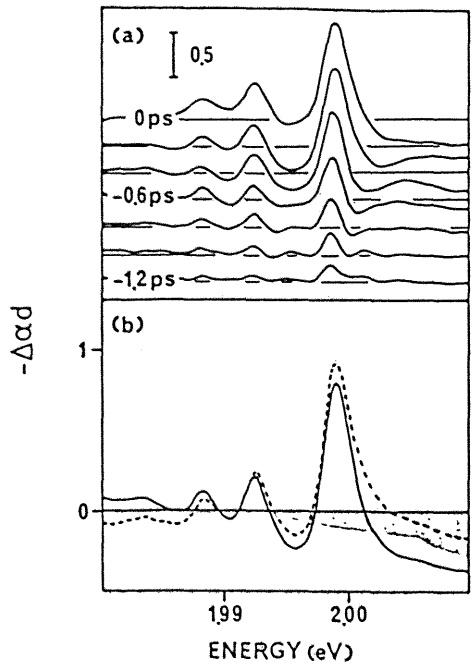

FIG. 3. (a) Absorption changes at several negative time delays. (b) Differential transmission spectra at two time delays. The shaded region corresponds to the one-phonon-assisted indirect transition. The spectral shape of the region is expressed by $(E-E^i_{gx}+E^A_{op})^{1/2}+(E-E^i_{gx}+E^C_{op})^{1/2}$, where E is the photon energy, E^i_{gx} is the indirect exciton energy, and E^A_{op} and E^C_{op} are the energies of $A(Z)$ and $C(Z)$ optical phonons, respectively.

As expected at positive time delays, the transient spectral oscillatory structures have vanished. In Fig. 3(b), where the differential transmission spectra for two time delays are plotted, we again observe that the entire spectral region covering the *R*, *S*, and *T* excitons and the transparency region oscillate in time. As we will show later in this paper, this temporal oscillation does not originate from an absorption change, but results from a refractive-index change. Also, an induced absorption region (where the $-\Delta\alpha d$ signal is negative), as displayed by the shaded area, is seen to coincide with the one-phonon-assisted indirect excitonic transition region. The absorption spectrum due to the thermal-phonon-assisted indirect transition has been extensively studied by Kaifu and Komatsu.[5] The induced absorption region is built up quickly at 0 fs and decays slowly. The *R*, *S*, and *T* lines show small broadening with no detectable energy shift as can be seen from Fig. 3(b). These observations cannot be explained by a temperature rise induced by the laser irradiation since such a temperature rise would be expected to cause an energy shift of the *R*, *S*, and *T* lines in addition to their broadening.[8]

Figure 4 shows the dynamics of the $-\Delta\alpha d$ signal at the *R* exciton for longer time delays, and its power spectrum obtained by numerical Fourier transformation after baseline subtraction. Two prominent peaks positioned at 0.6 and 3.4 THz, labeled *A* and *C*, appear in the spec-

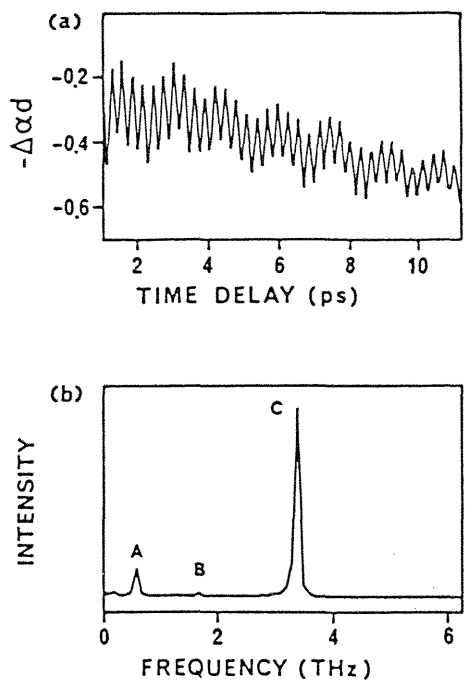

FIG. 4. Long-period temporal oscillation at the R exciton and its power spectrum obtained by the numerical Fourier transformation. The inclined baseline is subtracted from the temporal trace before the transformation. Three peaks appearing in the power spectrum are assigned to the phonon modes of A_g symmetry.

trum. An additional peak at 1.8 THz, labeled B, is also present with a much reduced strength. Raman-scattering experiments have revealed[6,7] three prominent Raman peaks with energy shifts of 22.8, 58.5, and 113.3 cm^{-1}, corresponding to the phonon frequencies of 0.68, 1.75, and 3.40 THz, and being referred to as zone-center phonons $A(\Gamma)$, $B(\Gamma)$, and $C(\Gamma)$, respectively.[6,7] The peaks are assigned to Raman-active modes at the Γ point belonging to the irreducible representation A_g. We also observed these peaks in the Raman spectrum of our sample, confirming prior measurements. Also, resonant Raman scattering, where the resonance is with respect to the indirect exciton energy, E_{gx}^{i} (with the incident photon energy being at E_{gx}^{i} plus the phonon energy), have shown the participation of the zone-boundary Z phonons.[6] The Z phonon energies are very close to the Γ phonon energies, being 20.8, 56.7, and 110.2 cm^{-1} for the $A(Z)$, $B(Z)$, and $C(Z)$ phonons, respectively. As shown in Fig. 1, our laser spectrum covers not only the R, S, and T excitons, but also the energy spectrum in the vicinity of the indirect exciton. Therefore, we expect that both Γ and Z phonons are coherently generated.

The observed temporal oscillations result from the time-dependent refractive index change induced by the strong incident femtosecond light pulses, impulsively generating coherent phonons. The coherent phonons modulate the refractive index. The phase of the light field after passing through the transparent material with time-dependent refractive index $n(t)$ is written as

$$\phi_{out}=\phi_{in}+n(t)d\omega_{in}/c \ , \tag{1}$$

where d is the thickness of the material, ϕ_{in} and ω_{in} are the phase and frequency of input light field, and c is the speed of light in vacuum. We assume $n(t)$ oscillates continuously with a single frequency, given by

$$n(t)=n_0+\Delta n \sin\Omega t \ , \tag{2}$$

where n_0 is the linear refractive index, Δn is an oscillation amplitude of the refractive index, and Ω is the frequency of oscillation. The frequency is given by a time derivative of the phase. Therefore, frequency of output light field ω_{out} is written as

$$\omega_{out}=\omega_{in}(1+d\Delta n\,\Omega\cos\Omega t/c) \ . \tag{3}$$

The oscillation amplitude of the transmitted spectrum is $\simeq 4$ meV from Fig. 2. Using the experimental parameters in Eq. (3), a value of $\Delta n=3\times10^{-3}$ is obtained. The energy density of the pump pulses absorbed by the sample is 255 $\mu J/cm^2$.

The probe spectral shift is proportional to the time differential of the phonon-modified refractive index. Thus, the Fourier transform of the time-domain data gives the phonon spectrum. The effect of propagation delay is reasonably omitted—since the pump and probe pulses travel in the same direction, they require the same time delay to reach a respective layer. Therefore, relative timing of the pump and probe pulses is the same at every layer.

In Fig. 5, we show the dynamics of the $-\Delta\alpha d$ signals for the transparency region of the sample at 1.967 eV for various time domains, including the very long times, exhibiting the damping of the induced oscillations. The dominant oscillation with a ~300-fs period is clearly observed to continue for more than one hundred periods.

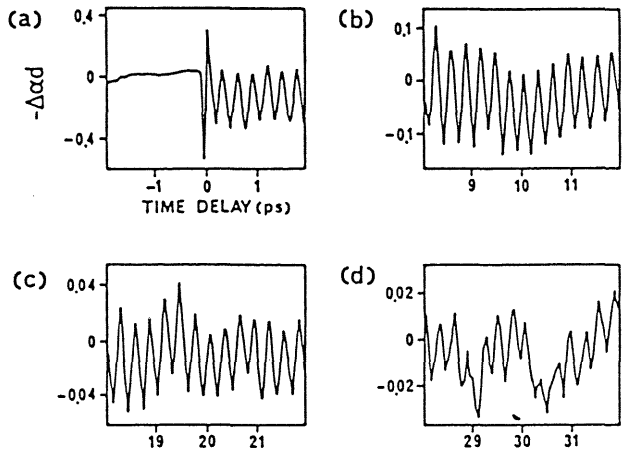

FIG. 5. The relaxation of coherent phonon oscillation at transparent region. The dominant oscillation (~300-fs period) continues for more than one hundred periods. At longer time delay, the slow but long-lived oscillation (1.5-ps period) becomes dominant.

In addition, we have seen a slower but long-lived oscillation with a period of ~ 1.5 ps. This long-lived 1.5-ps-period oscillation was seen in Raman-scattering experiments and has been assigned to the rigid layer mode by Komatsu, Karasawa, and Kaifu.[6]

In the presence of coherent phonons, the R, S, and T lines show a small broadening, but no detectable shift and no phonon side bands. In this sense, the stacking-fault direct excitons are affected only slightly by the generated coherent optical phonons. On the other hand, a prominent induced absorption band, which is observed above the energy of indirect exciton minus the Z point phonon energies of 20.8 and 110 cm^{-1}, implies that the indirect transitions are strongly coupled with coherent phonons. We speculate that this induced absorption is associated with a strong coherent phonon-assisted transition. It is noted that the position of the laser frequency with respect to the absorption edge of the BiI_3 is also important for the efficient coherent phonon effect. Since our laser spectrum covers the absorption edge, we think that resonant enhancement contributes to both generation and detection of coherent phonons. A detailed study in both theoretical and experimental aspects is needed to clarify these interactions further.

In conclusion, coherent phonon oscillation is observed in a layered compound BiI_3 by a femtosecond pump and probe technique. Coherent phonons cause ultrafast phase modulation through the change in refractive index. A distinct spectral shift of the transmitted probe pulses was observed. The coherent phonon oscillation continues for more than one hundred periods. The Fourier analysis of the temporal trace reveals three frequency components that correspond to the Raman-active optical phonons. The interaction of coherent phonons with indirect excitons appears to cause an induced absorption.

This work was supported by the NEDO (New Energy and Industrial Technology Development Organization) of Japan, and the International Science Research Program (Grant No. 02044021) from the Ministry of Education, Science and Culture, Japan (MESC). The Arizona group was also supported by the United States National Science Foundation and the United States Army Research Office.

[1]S. De Silvestri, J. G. Fujimoto, E. P. Ippen, E. B. Gamble, Jr., L. R. Williams, and K. A. Nelson, Chem. Phys. Lett. 116, 146 (1985).

[2]W. E. Bron, J. Kuhl, and B. K. Rhee, Phys. Rev. B 34, 6961 (1986).

[3]G. C. Cho, W. Kütt, and H. Kurz, Phys. Rev. Lett. 65, 764 (1990).

[4]J. M. Chwalek, C. Uher, J. F. Whitaker, G. A. Mourou, and J. A. Agostinelli, Appl. Phys. Lett. 58, 980 (1991).

[5]Y. Kaifu and T. Komatsu, J. Phys. Soc. Jpn. 40, 1377 (1976); see also Y. Kaifu, J. Lumin. 42, 61 (1988).

[6]T. Karasawa, T. Komatsu, and Y. Kaifu, Solid State Commun. 44, 323 (1982); see also T. Komatsu, T. Karasawa, T. Iida, K. Miyata, and Y. Kaifu, J. Limin. 24&25, 679 (1981); see also T. Karasawa, T. Iida, M. Sasaki, T. Komatsu, and Y. Kaifu, J. Phys. C 18, 4043 (1985).

[7]Y. Petroff, P. Y. Yu, and Y. R. Shen, Phys. Status Solidi B 61, 419 (1974).

[8]K. Watanabe, T. Karasawa, T. Komatsu, and Y. Kaifu, J. Phys. Soc. Jpn. 55, 897 (1986).

[9]B. Bluegel, N. Peyghambarian, G. Olbright, M. Lindberg, S. W. Koch, M. Joffre, D. Hulin, A. Migus, and A. Antonetti, Phys. Rev. Lett. 59, 2588 (1987); see also M. Joffre, D. Hulin, A. Migus, A. Antonetti, C. Benoit a la Guillaume, N. Peyghambarian, M. Lindberg, and S. W. Koch, Opt. Lett. 13, 276 (1988); see also M. Lindberg and S. W. Koch, Phys. Rev. B 38, 7607 (1988); see also J. P. Sokoloff, M. Joffre, B. Fleugel, D. Hulin, M. Lindberg, S. W. Koch, A. Migus, A. Antonetti, and N. Peyghambarian, *ibid.* 38, 7615 (1988).

Biaxial splitting of optical phonon modes in ZnSe-ZnS strained-layer superlattices

Aishi Yamamoto, Yoichi Yamada, and Yasuaki Masumoto
Institute of Physics, University of Tsukuba, Tsukuba, Ibaraki 305, Japan

(Received 26 November 1990; accepted for publication 16 February 1991)

Raman scattering studies were performed on ZnSe-ZnS strained-layer superlattices with the incident light parallel as well as perpendicular to the interface plane. We found for the first time that the optical phonon modes split into two types, that is a singlet and a doublet, by the built-in biaxial stress. A new method to characterize the directional stress is demonstrated.

Recently, much attention has been paid to the various kinds of semiconductor heterojunctions. This is because they have novel electrical and optical properties applicable to many kinds of devices. However, most of them have inherent stress at the heterojunction interface due to the lattice mismatch. For example, the lattice mismatch in ZnSe-ZnS superlattices is about 4.5%. They become strained-layer superlattices (SLSs) within the critical thicknesses.[1] There exists a stress lying in the plane parallel to the interface. In this sense they have quasi-two-dimensional structures.

These strains induce a change in the band structure, and then affect the optical properties.[2] Therefore, it is essentially important to measure the strains in SLSs. Many researchers have estimated the strains in the SLSs by means of Raman scattering.[3–8] All of the previous Raman studies of the strains measured the peak shifts of longitudinal optical (LO) phonons from bulk energies in a backscattering configuration with the incident light perpendicular to the interface plane. In this configuration, however, we cannot observe the directional stress directly. The biaxial stress may induce the biaxial splitting of optical phonons. In order to find the biaxial splitting of the phonon modes, we newly measured Raman scattering with the incident light parallel as well as perpendicular to the interface plane. As a result, we were able to observe two types of phonon modes, that is a singlet and a doublet, for the first time.

The unstrained lattice constants of bulk ZnSe and ZnS are 5.6687 Å (a_{ZnSe}) and 5.4093 Å (a_{ZnS}), respectively. Thus ZnSe layers are under biaxial compressive stress, while ZnS layers are under biaxial tensile stress. The lattice constant of the strained layers in the plane parallel to the interface ($a_{\parallel}$) is given by the following equation:[9]

$$a_{\parallel}=a_{ZnSe}\left(1-\frac{fG_{ZnSe}L_{ZnSe}}{G_{ZnS}L_{ZnS}+G_{ZnSe}L_{ZnSe}}\right), \tag{1}$$

where L_{ZnSe} and L_{ZnS} are the thicknesses of ZnSe and ZnS, f is the lattice mismatch of the unstrained ZnSe and ZnS layers defined by the equation, $f=(a_{ZnSe}-a_{ZnS})/a_{ZnS}$, G_{ZnSe} and G_{ZnS} are shear moduli of ZnSe and ZnS, respectively.

The components of strain-tensor parallel to the interface plane are given by

$$\epsilon_{xx}=\epsilon_{yy}=(a_{\parallel}-a)/a=(S_{11}+S_{12})/X, \tag{2}$$

where S_{11} and S_{12} are elastic compliance constants and X is the strength of the stress. Following Cerdeira *et al.*,[10] we can obtain two types of the energy deviations from the energy of bulk modes (ω_0) under biaxial stress in the (001) plane:

$$\Delta\Omega_s=[pS_{12}+q(S_{11}+S_{12})]X/\omega_0, \tag{3a}$$

$$\Delta\Omega_d=[p(S_{11}+S_{12})+q(S_{11}+3S_{12})]X/2\omega_0, \tag{3b}$$

where p and q are parameters proportional to the changes of the spring constant induced by the strain. In Eq. (3), $\Delta\Omega_s$ indicates the shift of the singlet-type mode vibrating parallel to the ⟨001⟩ axis, while $\Delta\Omega_d$ indicates the shift of doublet-type modes vibrating perpendicular to the ⟨001⟩ axis. This splitting occurs because the biaxial stress makes the sample quasi-two-dimensional. Using the parameters listed in Table I and Eq. (3), we can derive the relation $|\Delta\Omega_s|>|\Delta\Omega_d|$, for both ZnSe and ZnS.

When incident and backscattered light are parallel to the ⟨001⟩ axis (case-I), the LO mode corresponds to the displacement of the atoms along the ⟨001⟩ direction. Therefore, it will shift as the singlet type. On the other hand, the TO modes correspond to the displacement in the plane parallel to the interface. Therefore, it will shift as the doublet type. Thus in this experimental configuration, Eq. (3) indicates the energy deviations of the LO and TO modes as

$$\Delta\Omega_s^{LO}=[pS_{12}+q(S_{11}+S_{12})]X/\omega_0^{LO}, \tag{4a}$$

$$\Delta\Omega_d^{TO}=[p(S_{11}+S_{12})+q(S_{11}+3S_{12})]X/2\omega_0^{TO}. \tag{4b}$$

We consider next the case where the incident and backscattered light are parallel to the ⟨110⟩ axis (case-II). In this configuration, we can expect the LO mode will shift as the doublet type and the TO modes will split into the singlet and doublet types. From Eq. (3) we can obtain

$$\Delta\Omega_d^{LO}=[p(S_{11}+S_{12})+q(S_{11}+3S_{12})]X/2\omega_0^{LO}, \tag{5a}$$

$$\Delta\Omega_s^{TO}=[pS_{12}+q(S_{11}+S_{12})]X/\omega_0^{TO}, \tag{5b}$$

$$\Delta\Omega_d^{TO}=[p(S_{11}+S_{12})+q(S_{11}+3S_{12})]X/2\omega_0^{TO}. \tag{5c}$$

To summarize the above mentioned expectation,[11] (i) we will observe two types of shifts, a singlet and a

 0003-6951/91/192135-03$02.00

TABLE I. Parameters for ZnSe and ZnS used in the calculation.

	ZnSe	ZnS
LO mode (cm^{-1})	252[a]	349[a]
TO mode (cm^{-1})	205[a]	271[d]
S_{11} (10^{-12} dyn^{-1} cm^2)	2.11[b]	1.89[c]
S_{12} (10^{-12} dyn^{-1} cm^2)	−0.78[b]	−0.72[c]
p (10^{28})	−0.41[c]	−0.39[c]
q (10^{28})	−0.59[c]	−0.99[c]

[a]Present work.
[b]In Landolt–Börnstein—Numerical Data and Functional Relationships in Science and Technology, Vol. 17b (Semiconductors—Physics of II-IV and I-VII Compounds, Semimagnetic Semiconductors), edited by O. Madelung, M. Schulz, and H. Weiss (Springer, Berlin, 1982), p. 145.
[c]Reference 10.
[d]W. G. Nilsen, Phys. Rev. 182, 838 (1969).
[e]Reference 7.

doublet, of each of the LO and TO modes, corresponding to the two cases of the scattering configuration, and (ii) we will observe the singlet-type mode shifts larger than the doublet-type mode.

In the present work we used three samples grown by low-pressure metalorganic chemical vapor deposition (MOCVD)[12] on (001)GaAs substrates. All the samples have the same thickness of ZnS layers (40 Å) and consist of 150 periods of the superlattice, but the thickness of ZnSe layers are different [(a) 15 Å, (b) 20 Å, (c) 25 Å]. We used a (110) cleavage plane for the case-II configuration measurements.

For the case-I experiments, a quasi-backscattering configuration was used. Raman scattering measurements were performed at room temperature with the 4880 Å line of an Ar ion laser. The scattered light was analyzed by a double monochromator (Spex; 1403). For the case-II configuration, we used a Raman microprobe measurement system (Japan Spectroscopic Co., Ltd.; R-MPS-11) with a 25 cm filter double monochromator and a 1 m monochromator. Measurements were done at room temperature with the 5145 Å line of an Ar ion laser.

Figure 1 shows Raman spectra of samples (a), (b), and (c) in the case-I configuration. Strong peaks of TO and LO modes of a GaAs substrate are observed at about 268 and 291 cm^{-1}. The dashed lines indicate the positions of the unstrained bulk ZnSe and ZnS LO modes. Very weak ZnSe TO modes are observed at about 210 cm^{-1}, although they are forbidden in this experimental configuration. As seen in the figure, ZnSe LO modes shift toward the higher energies, while ZnS LO modes shift toward the lower energies. This is because the ZnSe layers are under compressive stress and the ZnS layers are under tensile

TABLE II. Observed energy deviation of the LO and TO modes from the energy of the bulk mode for the sample (c).

		ZnSe (cm^{-1})	ZnS (cm^{-1})
LO	singlet	+7.5	−14.0
	doublet	+2.5	−21.4
TO	singlet	+14.5	−35.8
	doublet	+6.7	···

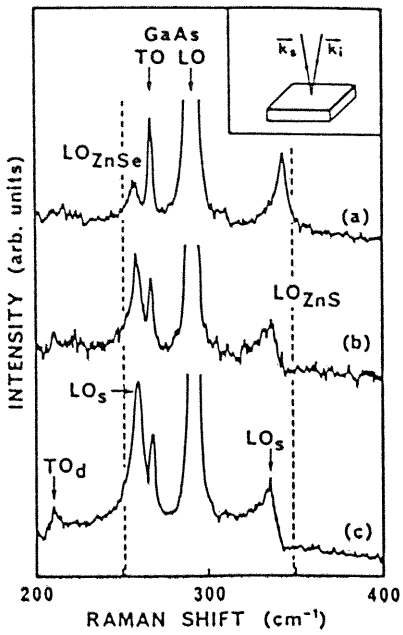

FIG. 1. Raman spectra of ZnSe-ZnS SLSs with a fixed ZnS layer thickness (40 Å) and various ZnSe ones: (a) 15 Å, (b) 20 Å, (c) 25 Å. The dashed lines show the unstrained bulk frequencies. The inset shows schematically the experimental configuration: the incident light is parallel to the ⟨001⟩ axis (case-I). The subscripts of s and d denote a singlet and a doublet, respectively.

stress. Although the shift of the ZnSe LO mode in three samples does not differ from each other, the shift of the ZnS LO mode decreases with increasing ZnSe thickness. These observations are consistent with the previous works.[3–8] As mentioned above, in the case-I configuration, we can regard the shift of LO modes as the singlet type and that of TO modes as the doublet type.

Raman spectra in the case-II configuration are shown in Figs. 2 and 3. The incident light was polarized perpendicular or parallel to the ⟨001⟩ axis. The doublet TO mode is allowed for both polarizations, while the singlet TO mode is allowed only for the perpendicular polarization. Taking into account this selection rule, we identified the peaks of 210 and 240 cm^{-1} as doublet TO(ZnSe) and singlet TO(ZnS), respectively. Very weak peaks of about 255 cm^{-1} are identified as the forbidden ZnSe LO(doublet) mode. We can see small peaks at about 220 cm^{-1} in Fig. 3. We identified them as the forbidden singlet TO(ZnSe) mode. It is allowed for the perpendicular polarization. However, it is not observed in Fig. 2. This is because the singlet TO(ZnSe) mode is superposed on the singlet TO(ZnS) mode. This identification is justified by the following reasons. First of all, the intensity of the 220 cm^{-1} mode increases with the increase in thickness of the ZnSe layer. Thus the mode is of ZnSe. Second, because of the selection rule, the intensity of the mode is weaker than that of the doublet TO(ZnSe) mode.

Based on the above-mentioned identification, we can summarize the energy deviation of all the modes in Table II. Table II shows the energy deviation from the energy of the bulk mode for sample (c). As for ZnSe modes, we can

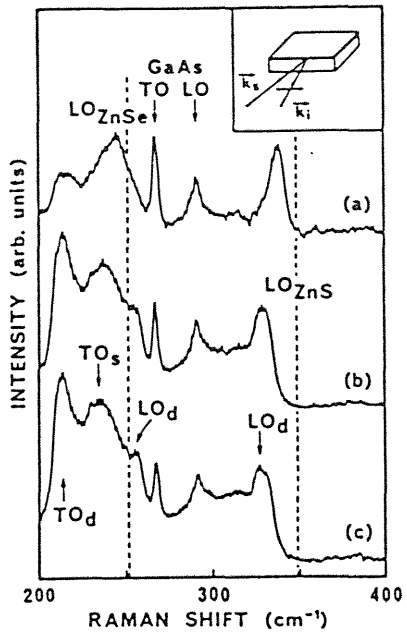

FIG. 2. Raman spectra of ZnSe-ZnS SLSs with a fixed ZnS layer thickness (40 Å) and various ZnSe ones: (a) 15 Å, (b) 20 Å, (c) 25 Å. The dashed lines show the unstrained bulk frequencies. The inset shows schematically the experimental configuration: the incident light is perpendicular to the ⟨001⟩ axis (case-II) and is polarized perpendicular to the ⟨001⟩ axis. The subscripts of *s* and *d* denote a singlet and a doublet, respectively.

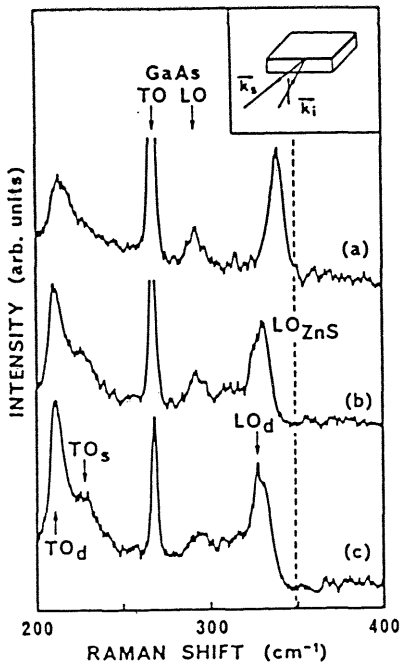

FIG. 3. Raman spectra of ZnSe-ZnS SLSs with a fixed ZnS layer thickness (40 Å) and various ZnSe ones: (a) 15 Å, (b) 20 Å, (c) 25 Å. The dashed line shows the unstrained ZnS energy. The inset shows schematically the experimental configuration: the incident light is perpendicular to the ⟨001⟩ axis (case-II) and is polarized parallel to the ⟨001⟩ axis. The subscripts of *s* and *d* denote a singlet and a doublet, respectively.

observe the singlet-type and doublet-type shifts for both LO and TO modes induced by the biaxial stress. The singlet-type mode shifts larger than the doublet-type one as was expected. On the other hand, for ZnS modes, we can also observe the singlet-type and doublet-type LO modes. However, the shift of the singlet type is not larger than that of the doublet type. This strange behavior may be explained by the following model. The dielectric continuum model[13] shows that the optical phonon mode, which propagates in the layer plane, can appear at new energy level. The energy deviation varies with change in the relative thickness of the two different dielectric layers. These effects enhance the energy deviation of the doublet-type LO(ZnS) mode. For this reason, the doublet-type LO(ZnS) mode can shift larger than the singlet-type one.

In conclusion, we studied Raman scattering of ZnSe-ZnS strained-layer superlattices with the incident light perpendicular and parallel to the interface plane. We observed for the first time two types of the optical phonon shift, a singlet and a doublet, induced by the biaxial stress. We obtained reasonable relations between the stress and the direction of the shift and between the layer thickness and the shift. The singlet-type mode shifts larger than the doublet-type mode for the ZnSe optical phonon modes. Not only strained-layer superlattices, but there are many systems having directional stress in semiconductor devices. The method of this work will become a new characterization tool for measuring the directional stress in these systems.

This work was supported in part by Scientific Research Grant-in-Aid No. 02205016 for Scientific Research on Priority Areas, New Functionality Materials—Design, Preparation and Control—by the Ministry of Education, Science and Culture of Japan. This work was done at the Cryogenic Center, University of Tsukuba.

[1] G. C. Osbourn, IEEE J. Quantum Electron. QE-22, 1677 (1986).
[2] T. Taguchi and Y. Yamada, Mater. Res. Soc. Symp. Proc. 161, 199 (1990).
[3] M. Nakayama, K. Kubota, H. Kato, and N. Sato, Solid State Commun. 51, 343 (1984).
[4] F. Cerdeira, A. Pinczuk, J. C. Bean, B. Batlogg, and B. A. Wilson, Appl. Phys. Lett. 45, 1138 (1984).
[5] B. Jusserand, P. Voisin, M. Voos, L. L. Chang, E. E. Mendez, and L. Esaki, Appl. Phys. Lett. 46, 678 (1985).
[6] S. Nakashima, Y. Nakakura, H. Fujiyasu, and K. Mochizuki, Appl. Phys. Lett. 48, 236 (1986).
[7] L. H. Shon, K. Inoue, K. Murase, H. Fujiyasu, and Y. Yamazaki, Solid State Commun. 62, 621 (1987).
[8] L. H. Shon, K. Inoue, O. Matsuda, K. Murase, T. Yokogawa, and M. Ogura, Solid State Commun. 67, 779 (1988).
[9] J. W. Matthews and A. E. Blakeslee, J. Cryst. Growth 32, 265 (1976).
[10] F. Cerdeira, C. J. Buchenauer, F. H. Pollak, and M. Cardona, Phys. Rev. B 5, 580 (1972).
[11] In Eq. (3), ω_0 may be the bare optical phonon energy due to spring constants only. But in Refs. 3 and 5–8, ω_0 has been treated conventionally as ω_{LO} or ω_{TO} in the calculation of each energy shift. We followed the conventional treatment in Eqs. (4) and (5). Anyhow, our conclusion is not influenced at all, whichever values are used.
[12] Y. Yamada and T. Taguchi, Tech. Rep. Osaka Univ. 39, 211 (1989).
[13] C. Colvard, T. A. Gant, M. V. Klein, R. Merlin, R. Fischer, H. Morkoc, and A. C. Gossard, Phys. Rev. B 31, 2080 (1985).

Type conversion under hydrostatic pressure in ZnSe-ZnS strained-layer superlattices

Yoichi Yamada and Yasuaki Masumoto
Institute of Physics, University of Tsukuba, Tsukuba, Ibaraki 305, Japan

Tsunemasa Taguchi
Department of Electrical Engineering, Faculty of Engineering, Osaka University, Suita, Osaka 565, Japan

Kenichi Takemura
National Institute for Research in Inorganic Materials, Tsukuba, Ibaraki 305, Japan
(Received 2 January 1991; revised manuscript received 26 March 1991)

A conversion from type-I to type-II in a ZnSe-ZnS strained-layer superlattice under hydrostatic pressure is observed. The hydrostatic-pressure dependence of the integrated intensity and the linewidth of the $n=1$ heavy-hole exciton emission spectra is represented by a couple of straight lines with a clear kink at about 31 kbar. Moreover, the emission peaks appear below the band-gap energy of the ZnSe well layers above 31 kbar. All of these features are well explained by the type conversion associated with the Γ-Γ conduction-band crossover between the ZnSe well and ZnS barrier layers.

In recent years, there has been much work on the effects of the external modulations in semiconductor superlattices and multiple-quantum-well structures. Hydrostatic-pressure studies[1-3] and electric-field studies[4] have enabled us to understand the fundamental electronic structures in GaAs-based quantum-well structures through the interlayer Γ-X crossover. Magnetic-field studies have also clarified the band structures in diluted magnetic semiconductor quantum-well structures such as ZnSe-$Zn_{1-x}Fe_xSe$ (Ref. 5) and CdTe-$Cd_{1-x}Mn_xTe$ (Ref. 6) through the Zeeman splitting of the valence band.

We present here the first evidence of a conversion from type I to type II under hydrostatic pressure in wide-band-gap ZnSe-ZnS strained-layer superlattices (SLS's). This type conversion results from a Γ-point crossover of the ZnSe well and ZnS barrier conduction bands. One of the most characteristic aspects of this SLS is that the conduction-band offset is much smaller than the valence-band offset. This aspect has been suggested by the model-solid theory.[7] Our recent studies by photoluminescence excitation (PLE) spectroscopy have shown that type-I ZnSe-ZnS SLS's have no electron quantum state higher than $n=2$ in the conduction-band wells.[8] The conduction-band offset was estimated to be less than 150 meV on the basis of Kronig-Penney analysis. Judging from the differences in the conduction-band deformation-potential constant and the bulk modulus of ZnSe well and ZnS barrier layers, one can expect that a conduction-band crossover between these layers occurs at a moderate value of hydrostatic pressure. This article presents the evidence of the crossover. It is clearly observed in the changes in the integrated intensity, the linewidth, and the peak energy of the $n=1$ heavy-hole exciton emission spectra.

ZnSe-ZnS SLS's were grown on (100)-oriented GaAs substrates at 350 °C without buffer layers by a low-pressure metal-organic chemical-vapor deposition (MOCVD) method with all gaseous sources. The sample used in this study consists of 150 periods of 2.0-nm-thick ZnSe well layers separated by 4.0-nm-thick ZnS barrier layers. The GaAs substrate was thinned to about 50 μm. A small piece of the thinned sample was placed in a Merrill-Bassett diamond-anvil cell with liquid nitrogen as the pressure transmitting fluid. The energy shift of the R_1 luminescence line from a ruby crystal was used to calibrate the pressure. The cell was directly immersed in liquid nitrogen. Photoluminescence (PL) spectra were measured using a conventional lock-in detection technique in conjunction with a 75-cm single grating monochromator. The excitation source was a 350-nm line of a continuous-wave argon-ion laser.

Figure 1 shows the schematic hydrostatic-pressure dependence of the conduction-band edges for both ZnSe well and ZnS barrier layers in the ZnSe-ZnS SLS. In this calculation, we used -5.4 and -4.0 eV as a hydrostatic band-gap deformation-potential constant (a_c-a_v) for ZnSe and ZnS, respectively.[9] Moreover, we divided the hydrostatic band-gap deformation-potential constant into a hydrostatic conduction-band deformation-potential constant (a_c) and a hydrostatic valence-band deformation-potential constant (a_v), using the calculated ratio (a_c/a_v) given by Camphausen, Connell, and Paul.[10] These values are listed in Table I. As a bulk modulus, we used 6.25×10^5 bar (Ref. 11) and 7.69×10^5 bar (Ref. 12) for ZnSe and ZnS, respectively. Therefore, we obtained the energy shift of the conduction-band edges under hydrostatic pressure by 5.84×10^{-3} P eV and 3.62×10^{-3} P eV for ZnSe and ZnS, respectively. Here P is the hydrostatic pressure in units of kbar. The conduction-band offset under no external hydrostatic pressure is shown as ΔE_c in this figure. The conduction-band edges for both ZnSe and ZnS layers shift toward higher energy with increasing hydrostatic pressure and cross at P_0, as shown in Fig. 1. In this way, our calculation suggests that the con-

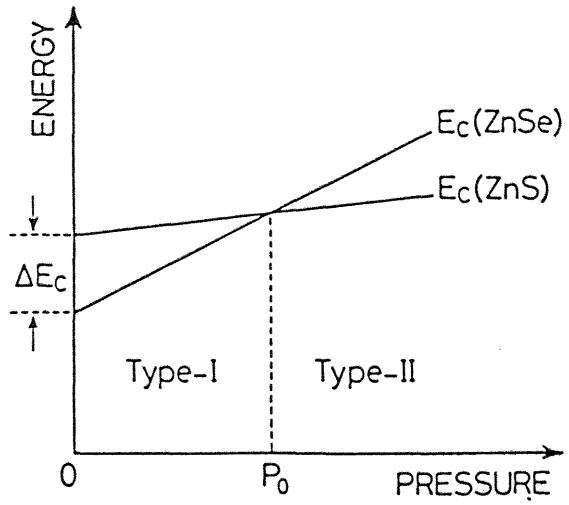

FIG. 1. Schematic changes in the conduction-band edges for both ZnSe well and ZnS barrier layers in a ZnSe-ZnS SLS as a function of hydrostatic pressure. In this figure, ΔE_c denotes the conduction-band offset at atmospheric pressure and P_0 denotes the crossover pressure.

version from type I ($P < P_0$) to type II ($P > P_0$) occurs in the ZnSe-ZnS SLS under hydrostatic pressure.

Figure 2 shows PL and absorption spectra of the ZnSe-ZnS SLS used in this study. Two peaks observed in the absorption spectrum correspond to $n = 1$ heavy-hole (hh) and $n = 1$ light-hole (lh) excitons. The PL peak appears by 28 meV lower-energy side of the $n = 1$ heavy-hole exciton peak in the absorption spectrum, and is located at the tail part of the exciton absorption spectrum. This dominant PL peak, therefore, can be attributed to the intrinsic radiative recombination of the $n = 1$ heavy-hole excitons. The Stokes shift is probably determined by the interface fluctuation. The fundamental optical properties of this SLS have already been reported.[13]

Photoluminescence spectra of the ZnSe-ZnS SLS under atmospheric and various hydrostatic pressures at 77 K are shown in Fig. 3. With the application of hydrostatic pressure, the PL peak position shifts toward higher energy and the linewidth broadening takes place. Especially, the linewidth obtained at 45.8 kbar is 3.3 times as broad as that obtained at atmospheric pressure. The line shape becomes much more asymmetric with increasing pressure because of the decrease of the intrinsic recombination relative to the lower-energy component of the spectrum. This lower-energy component can be attributed to the

TABLE I. The hydrostatic band-gap deformation-potential constants $a_c - a_v$, and the conduction- and valence-band deformation potential constants, a_c and a_v. These values are written in units of eV.

	$a_c - a_v$	a_c	a_v
ZnSe	−5.4	−3.65	1.75
ZnS	−4.0	−2.78	1.22

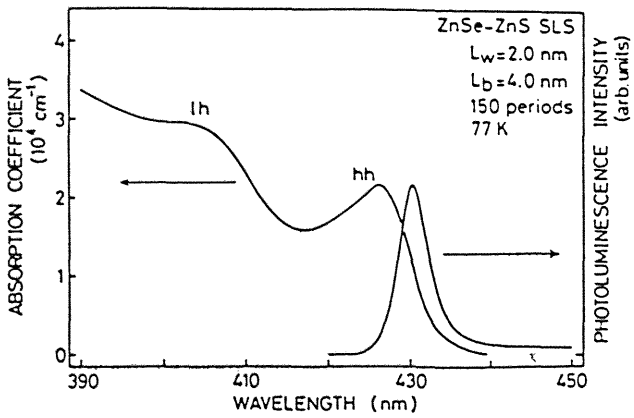

FIG. 2. Photoluminescence and absorption spectra of a ZnSe-ZnS SLS ($L_w = 2.0$ nm and $L_b = 4.0$ nm, 150 periods) at 77 K.

recombination of excitons localized more deeply. The origin of this component has not been understood clearly so far. It is probably ascribed to the recombination of excitons deeply localized at interface defects.

Figures 4(a) and 4(b) show the hydrostatic-pressure dependence of the integrated intensity and the linewidth (the full width at half maximum) of the $n = 1$ heavy-hole exciton emission spectra at 77 K, respectively. In this

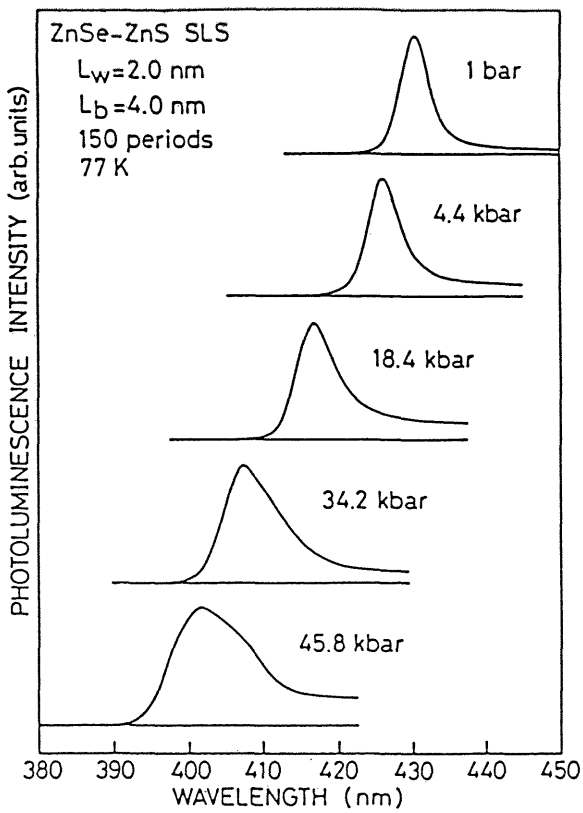

FIG. 3. Photoluminescence spectra of a ZnSe-ZnS SLS ($L_w = 2.0$ nm and $L_b = 4.0$ nm, 150 periods) under atmospheric and various hydrostatic pressures at 77 K. Each spectrum is normalized at the maximum of the peak height.

figure, solid lines are due to linear least-squares fits to the experimental data. The emission intensity in Fig. 4(a) gradually decreases with increasing hydrostatic pressure up to 31 kbar. With further increasing pressure the intensity decreases more rapidly. Therefore, the pressure dependence of the emission intensity is represented by a couple of straight lines with a kink. Parallel to these changes, the linewidth in Fig. 4(b) increases as the hydrostatic pressure increases, and the kink point in these changes appears at the same pressure of 31 kbar. These observations obtained in the changes in the integrated intensity and the linewidth can be explained by considering that the conduction-band edges of ZnSe and ZnS layers cross around 31 kbar and the conversion from type I to type II occurs at this pressure. Conduction electrons are confined to the ZnSe well layers below 31 kbar. However, electrons are confined to the ZnS barrier layers above 31 kbar. Then, the electrons and heavy holes are spatially separated and recombination takes place across the heterointerface. As a result, the intrinsic exciton luminescence intensity decreases. The emission intensity of the intrinsic component is more sensitive to the band structure than that of the lower-energy component of the spectrum, because the lower-energy component is due to excitons localized more deeply and is not sensitive to the change of band lineups from type I to type II. The overlap in the intrinsic and the lower-energy components may influence the linewidth and the PL peak position. However, as shown in Fig. 3, the emission intensity of the lower-energy component does not exceed that of the intrinsic one. Therefore, the influence of the overlap in the intrinsic and the lower-energy components is thought to be very small, especially on the emission intensity. Thus, the appearance of the clear kink point which was observed in the changes in the emission intensity and the linewidth can be explained only by the crossover to type II.

To support our identification, we estimated the luminescence quenching around the crossover. Using the envelope-function approximation, the square of the overlap integral between the $n=1$ electron wave function and the $n=1$ heavy-hole wave function at 50 kbar is about 17% of that at atmospheric pressure. In addition to the above value, we took account of the exciton effect, that is, the lateral spatial extension of the exciton Bohr radius in the direction parallel to the heterointerface.[14,15] As a result, we approximately obtained that the exciton oscilla-

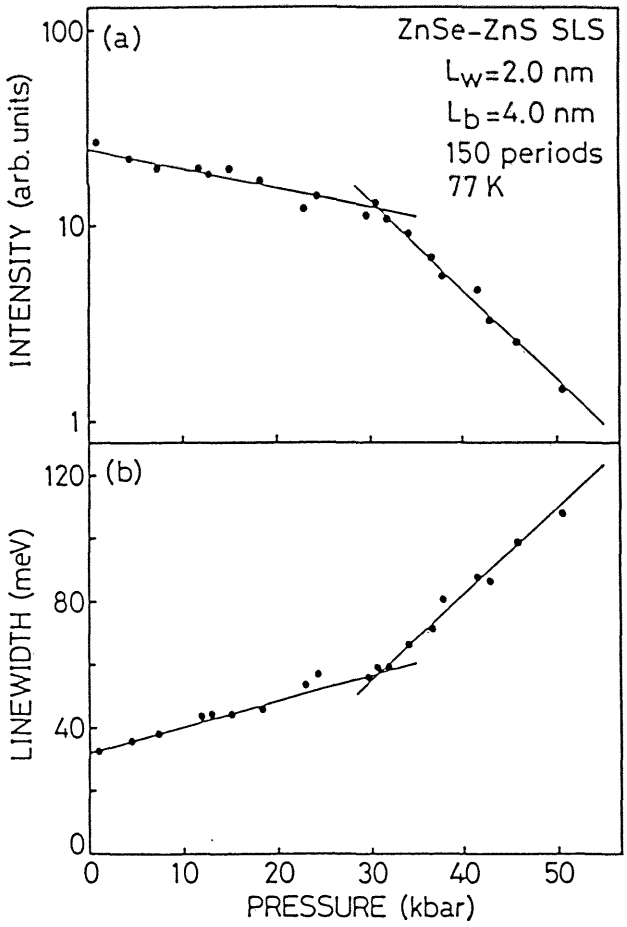

FIG. 4. (a) Hydrostatic pressure dependence of the integrated intensity and (b) the linewidth of the $n=1$ heavy-hole exciton luminescence of the ZnSe-ZnS SLS at 77 K. The solid lines are linear least-squares fits to the experimental data.

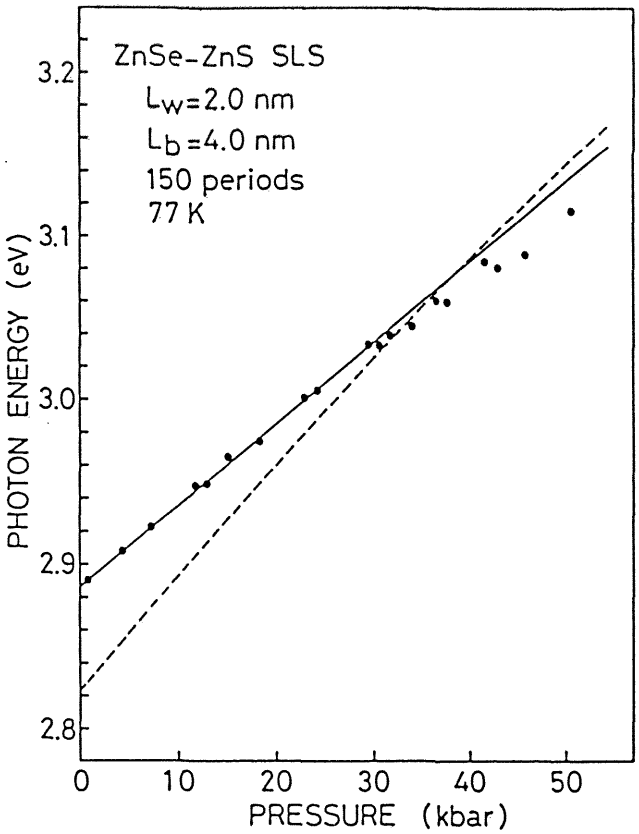

FIG. 5. Hydrostatic-pressure dependence of the peak energy of the $n=1$ heavy-hole exciton luminescence of the ZnSe-ZnS SLS at 77 K. The solid line is a linear least-squares fit to the experimental data below 30 kbar. The dashed line shows the hydrostatic-pressure dependence of the band-gap energy of the ZnSe well layers.

tor strength at 50 kbar decreased to about 4% of that at atmospheric pressure.[16] This calculated result supports the experimental luminescence quenching of about 7% shown in Fig. 4(a).

The pressure-dependent emission peak energies of the $n=1$ heavy-hole exciton at 77 K are shown in Fig. 5. The emission peak energy shifts toward higher energy with increasing hydrostatic pressure. The energy shift below 30 kbar is well fitted by a straight solid line shown in the figure. A dashed line shows the hydrostatic-pressure dependence of the band-gap energy of the ZnSe well layer at 77 K. We calculated it by taking account of the strain effect due to the lattice mismatch[8] and the experimental pressure coefficients of the band-gap energy.[17] Above 31 kbar, the peak energy deviates from the solid line and appears below the band-gap energy of the ZnSe well layer. This observation also supports that the conversion from type I to type II occurs around 31 kbar. Here, we do not take account of the $n=1$ heavy-hole quantum confinement energy and the binding energy of excitons, because these values are found to balance each other around the crossover.

The type conversion we observed is induced by the Γ-Γ conduction-band-edge crossover between ZnSe well and ZnS barrier layers. The crossover takes place because of the small conduction-band offset in this SLS and the difference in the energy shift of the conduction-band edges under hydrostatic pressure between these layers. The Γ-Γ type conversion may give unique characteristics to the system which is not observed in the Γ-X type conversion.

Finally, we consider the conduction-band offset. Recently, Shahzad, Olego, and Van de Walle have reported the empirical approach to derive the band offset in ZnSe-ZnS_xSe_{1-x} ($x<0.30$) SLS's.[18] They indicated that the conduction-band offsets are very small ($\Delta E_c \simeq 5$ meV), and that the experimental observations are in good agreement with the theoretical calculations based on the model-solid approach. On the basis of our hydrostatic-pressure measurements, we can obtain the conduction-band offset in ZnSe-ZnS SLS's shown as ΔE_c in Fig. 1 under no external hydrostatic pressure. Using the calculated energy shifts of both ZnSe and ZnS conduction-band edges as a function of hydrostatic pressure shown above and the crossover pressure obtained experimentally, we estimated the conduction-band offset ΔE_c to be 68.8 meV. If we use 820 meV as the valence-band offset on the basis of Harrison's linear combination of atomic orbitals theory, the conduction-band offset is estimated to be 198 meV without the effects of strain due to the lattice mismatch between ZnSe and ZnS layers. However, the effects of the strain must be considered in this SLS. In order to discuss the propriety of the obtained value of the conduction-band offset, we use the modified model-solid theory[8] as one of the theoretical approaches that can estimate the conduction-band offset. In this calculation, the biaxial strain due to the lattice mismatch can be divided into the uniaxial and the hydrostatic components and the effects of each component can be individually treated. As a result of these calculations, the conduction-band offset was estimated to be 74.7 meV. This calculated value of the conduction-band offset approximately agrees with the experimentally estimated value of 68.8 meV. Moreover, these two values are consistent with the result of Kronig-Penney's analysis of the PLE measurements.[8]

In conclusion, we have obtained direct observations of a conversion from type I to type II in a wide-band-gap ZnSe-ZnS strained-layer superlattice under hydrostatic pressure. This type conversion results from the Γ-Γ conduction-band crossover between ZnSe well and ZnS barrier layers and occurred around 31 kbar at 77 K. This phenomenon was clearly observed in the changes in the integrated intensity, the linewidth, and the peak energy of the $n=1$ heavy-hole exciton emission spectra. From our experimental results, we obtained the conduction-band offset at atmospheric pressure. It is $\Delta E_c=68.8$ meV. This value is close to that obtained by the semiquantitative calculations, and is consistent with our experimental results of the PLE spectroscopy.

This work was partly supported in by a grant-in-aid for Scientific Research on Priority Areas, New Functionality Materials—Design, Preparation, and Control—Grant No. 02205016 from the Ministry of Education, Science and Culture of Japan.

[1]D. J. Wolford, in *Proceedings of the 18th International Conference on the Physics of Semiconductors*, edited by O. Engström (World Scientific, Singapore, 1986), p. 1115, and references therein.

[2]U. Venkateswaran, M. Chandrasekhar, H. R. Chandrasekhar, B. A. Vojak, F. A. Chambers, and J. M. Meese, Phys. Rev. B 33, 8416 (1986), and references therein.

[3]Y. Masumoto, Y. Kinoshita, O. Shimomura, and K. Takemura, Phys. Rev. B 40, 11 772 (1989).

[4]M.-H. Meynadier, R. E. Nahory, J. M. Worlock, M. C. Tamargo, J. L. de Miguel, and M. D. Sturge, Phys. Rev. Lett. 60, 1338 (1988).

[5]X. Liu, A. Petrou, J. Warnock, B. T. Jonker, G. A. Prinz, and J. J. Krebs, Phys. Rev. Lett. 63, 2280 (1989).

[6]E. Deleporte, J. M. Berroir, G. Bastard, C. Delalande, J. M. Hong, and L. L. Chang, Phys. Rev. B 42, 5891 (1990).

[7]C. G. Van de Walle, Phys. Rev. B 39, 1871 (1989).

[8]Y. Yamada, Y. Masumoto, T. Taguchi, and S. Takeda, in *Proceedings of the 20th International Conference on the Physics of Semiconductors*, edited by E. M. Anastassakis and J. D. Joannopoulos (World Scientific, Singapore, 1990), p. 941.

[9]D. W. Langer, R. N. Euwema, K. Era, and T. Kada, Phys. Rev. B 2, 4005 (1970).

[10]D. L. Camphausen, G. A. N. Connell, and W. Paul, Phys. Rev. Lett. 26, 184 (1971).

[11]B. H. Lee, J. Appl. Phys. 41, 2984 (1970).

[12]C. F. Cline and D. R. Stephens, J. Appl. Phys. 36, 2869 (1965).

[13]Y. Yamada and T. Taguchi, J. Cryst. Growth 101, 661 (1990).

[14]Y. Shinozuka and M. Matsuura, Phys. Rev. B 28, 4878 (1983); 29, 3717(E) (1984).

[15]M. Matsuura and Y. Shinozuka, Phys. Rev. B 38, 9830 (1988).
[16]We also calculated the reduction factor of the exciton oscillator strength on the Kronig-Penney model. The reduction factor is found to be about 9%.
[17]S. Ves, K. Strössner, N. E. Christensen, C. K. Kim, and M. Cardona, Solid State Commun. 56, 479 (1985).
[18]K. Shahzad, D. J. Olego, and C. G. Van de Walle, Phys. Rev. B 38, 1417 (1988).

Raman study of disorder and strain in epitaxial ZnS_xSe_{1-x} films on a GaAs substrate

Yoshihiko Kanemitsu, Aishi Yamamoto, Hitoshi Matsue, and Yasuaki Masumoto
Institute of Physics, University of Tsukuba, Tsukuba, Ibaraki 305, Japan

Shigeki Yamaga and Akihiko Yoshikawa
Department of Electrical and Electronics Engineering, Chiba University, Yayoi-cho, Chiba 260, Japan

(Received 12 November 1991; accepted for publication 2 January 1992)

Quantitative characterization of disorder and strain in ZnS_xSe_{1-x}/GaAs lattice-mismatched semiconductor heterostructures was successfully done by means of Raman spectroscopy. The alloy disorder and the phonon coherence length in epitaxial ZnS_xSe_{1-x} films were estimated from the Raman linewidth of the ZnSe-like LO phonon by using a spatial correlation model. The strain due to the lattice mismatch near the interface between ZnS_xSe_{1-x} and GaAs was deduced from the linewidth of the GaAs LO phonon.

Recently, there is much interest in wide band-gap ternary II-VI semiconductor alloys for their potential applications in optoelectronic devices in the blue spectral region.[1] The ternary semiconductor (e.g., ZnS_xSe_{1-x}) have many advantages over binary compounds (e.g., ZnSe) because the lattice constant and optical properties can be varied by changing the composition. The epitaxial thin films of ternary II-VI semiconductors have been usually grown on GaAs substrates with slightly different lattice constants. The alloy disorder (alloy potential fluctuations)[2] of ternary semiconductors and the strain due to the lattice mismatch between the epitaxial films and the substrate[3,4] play a major role in determining electrical and optical properties of epitaxial films. That is why the quantitative characterization of alloy disorder and strain is an important issue in the epitaxial growth and device applications of II-VI ternary semiconductors. In this work, we tried to evaluate quantitatively disorder and strain in ZnS_xSe_{1-x}/GaAs heterostructures by means of Raman spectroscopy.

ZnS_xSe_{1-x} films were grown by atmospheric pressure metalorganic chemical vapor deposition (MOCVD) on the (100) GaAs substrate at 500 °C using dimethylzinc, dimethylselenide, and diethylsulfide. The S composition ranging from $x=0$ to 0.13 was controlled by the flow rate of diethylsulfide. The film thickness of all samples was about 1.3 μm. The lattice constants of epitaxial films were measured by x-ray diffraction. We found that the lattice constant of a ZnS_xSe_{1-x} film at $x=0.07$ was nearly equal to that of the GaAs substrate.

Raman scattering measurements were performed at room temperature in two backscattering configurations: (1) The incident laser direction is normal to the growth plane (configuration I). Raman spectra were obtained by using 488- or 514.5-nm Ar^+ laser light and a double monochromator (Spex 1403). (2) The heterostructure samples were cleaved and the cleavage plane was microprobed (configuration II). Microprobed spectra were obtained by using 514.5-nm laser light and a Raman microprobe measurement system (Japan Spectroscopic Co. Ltd., R-MPS-11) consisting of a 25-cm filter monochromator and a 1-m monochromator. The diameter of the focused beam was about 1 μm. These configurations are illustrated in the insets of Fig. 1.

Figure 1 shows the Raman spectra of the $ZnS_{0.07}Se_{0.93}$/GaAs heterostructure ranging from 160 to 320 cm^{-1} in two different configurations. We used the (100) plane in configuration I [Fig. 1(a)] and the (110) plane in configuration II [Fig. 1(b)]. The selection rule for zinc-blende crystal structures shows that only LO modes are allowed in configuration I. On the other hand, LO modes are forbidden and TO modes are allowed in configuration II. In Fig. 1(a), GaAs LO and ZnSe-like LO modes and also a weak forbidden ZnSe-like TO mode were observed. In Fig. 1(b), a ZnSe-like TO and weak forbidden ZnSe-like LO modes were observed. If the strain due to the lattice mismatch between ZnS_xSe_{1-x} and GaAs is very high in the ZnS_xSe_{1-x} film, the shift of the Raman peak frequency due to high misfit strains[3] and/or the splitting of phonon modes due to biaxial stress[5] may be observed in configuration II. However, over all of the composition range from 0 to 0.13, we were not able to observe a significant difference in the peak frequency between the two configurations.

Figure 2 shows the Raman peak frequency ω and the linewidth Γ_{ZnSe} (full width at half maximum) of the ZnSe-like LO phonon obtained in configuration I as a function of the S composition. With increasing S composition, the peak frequency decreases and the linewidth increases. The composition dependence of Raman spectra in ZnSSe films is considered to be determined by both alloy disorder of the film and the misfit strain. If the strain dominates Raman spectra of the ZnSe-like LO phonon, the composition dependence of Γ_{ZnSe} and ω at $x<0.07$ differs from those at $x>0.07$, because the compressive and tensile stresses due to the lattice mismatch should exist in ZnS_xSe_{1-x} films at $x<0.07$ and $x>0.07$, respectively. However, Γ_{ZnSe} increases monotonically with increasing x. Moreover, the

 0003-6951/92/111330-03$03.00

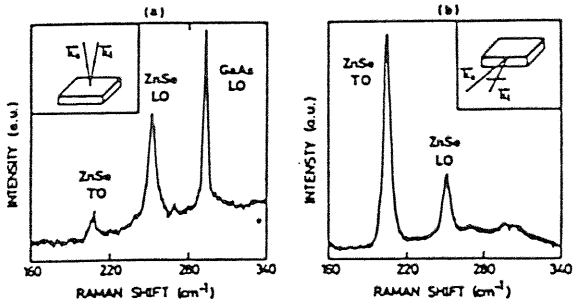

FIG. 1. Raman spectra of the ZnS_xSe_{1-x} ($x=0.07$) films at room temperature in two different configurations. The insets indicate the geometrical configuration: (a) configuration I and (b) configuration II.

composition dependence of Raman peak frequencies of the ZnSe-like LO and TO phonons in epitaxial films agrees very well with that observed in the bulk mixed crystals.[6]

Therefore, the geometrical and composition dependencies of Raman spectra show that the strain in thin films do not play an important role in the composition dependence of Raman spectra.

We have more evidence to deny the strain effect. A small TO phonon peak was observed in configuration I, although it is forbidden by a selection rule in this geometry. Figure 3 shows the composition dependence of the intensity ratio of the forbidden TO to the allowed LO phonons. The intensity ratio increases monotonically with increasing S composition. Monotonical composition dependence of Γ_{ZnSe} and I_{TO}/I_{LO} clearly shows that disorder

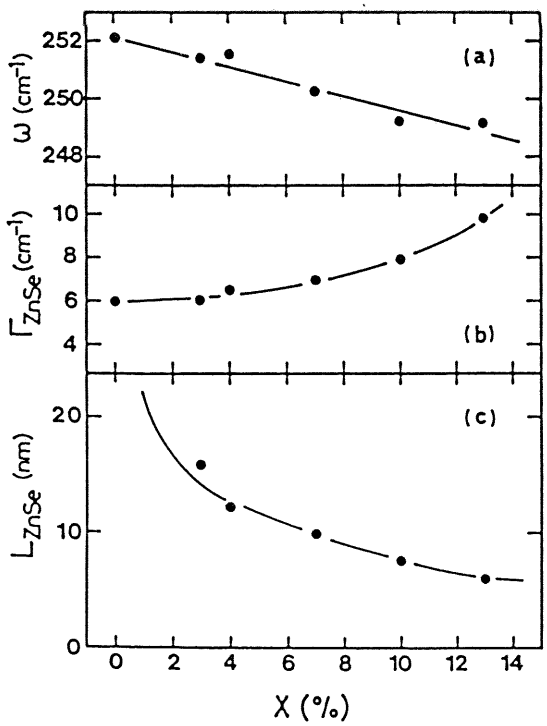

FIG. 2. Peak Raman frequency ω, Raman linewidth Γ_{ZnSe}, and the correlation length L_{ZnSe} of the ZnSe-like LO phonon as a function of molar fraction x in ZnS_xSe_{1-x}. L_{ZnSe} is estimated by using the spatial correlation model with the Gaussian correlation function.

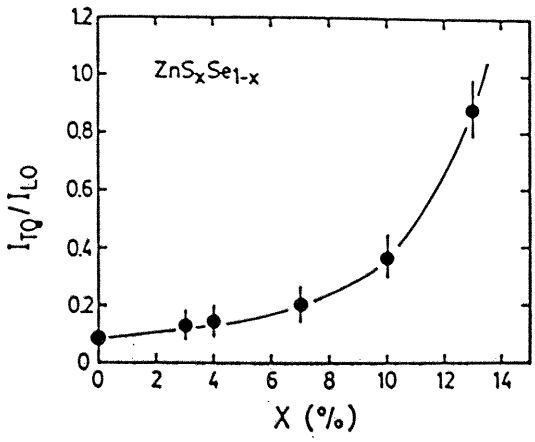

FIG. 3. Intensity ratio of the forbidden TO signal to the allowed LO signal obtained in configuration I as a function of molar fraction x in ZnS_xSe_{1-x}.

rather than misfit strain determines Raman spectra of ZnSSe films on the GaAs substrate.

Here, we discuss the disorder in ZnS_xSe_{1-x} films using a spatial correlation model.[2,7] The alloy disorder causes a relaxation of the q-vector selection rule and the spatial correlation function of the phonon becomes finite. A Gaussian spatial correlation function $\exp(-2r^2/L^2)$ has been used to account for q-vector relaxation related to the alloy disorder, where L is the correlation length. The Raman intensity $I(\omega)$ at a frequency ω can be expressed as[2,8]

$$I(\omega) \propto \int_0^1 \exp(-q^2L^2/4)/\{[\omega-\omega(q)]^2 + (\Gamma_0/2)^2\}d^3q, \quad (1)$$

where q is expressed in units of $2\pi/a$, a is the lattice constant, and Γ_0 is the linewidth of the ZnSe LO phonon in the pure ZnSe film. We take the dispersion $\omega(q)$ of the LO phonon based on a one-dimensional chain model:

$$\omega^2(q) = A + \{A^2 - B[1-\cos(\pi q)]\}^{1/2}, \quad (2)$$

where $A=3.2\times10^4$ cm^{-2} and $B=4.5\times10^8$ cm^{-4} for ZnSe.[9] These parameters were determined for Eq. (2) to describe well the neutron scattering data.[9] By using Eqs. (1) and (2), we can calculate the line shape of the Raman signal as a function of L. We compared the experimental linewidth of the ZnSe-like LO phonon with the calculated one. In this way, the correlation length of the ZnSe-like LO phonon, L_{ZnSe}, was deduced from Γ_{ZnSe}.

Figure 2(c) shows L_{ZnSe} plotted as a function of S composition. In the two-mode behavior alloys such as ZnS_xSe_{1-x},[6,10] we can consider that the ZnSe- and ZnS-like phonon modes are localized in the ZnSe and the ZnS regions, respectively. L_{ZnSe} means the average size of the localized region of ZnSe-like phonons. The phonon coherence length L_{ZnSe} decreases with increasing S composition; the phonon extended region becomes very small. This is caused by the alloy disorder. The intensity ratio of TO to LO phonons in Fig. 3 increases with decreasing L_{ZnSe} and this can be also interpreted by the disorder-induced Raman

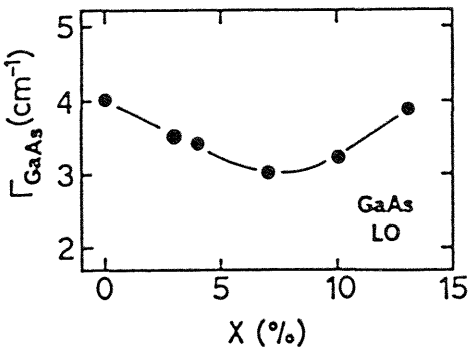

FIG. 4. Raman linewidth Γ_{GaAs} of the GaAs LO phonon as a function of S composition in ZnS_xSe_{1-x}

scattering. Therefore, the correlation length L_{ZnSe} becomes a quantitative parameter reflecting disorder of ZnSSe epitaxial films.

Figure 3 shows that the very weak forbidden ZnSe-TO phonon was observed even in the *pure* ZnSe film. We believe that this is caused by the misfit strain near the interface. Figure 4 shows the Raman linewidth of GaAs LO phonons, Γ_{GaAs}, as a function of S composition of ZnS_xSe_{1-x} films. At $x=0.07$, Γ_{GaAs} exhibits a minimum value, although we were not able to observe the peak frequency shift. Since the lattice constant of ZnS_xSe_{1-x} at $x=0.07$ is nearly equal to that of GaAs, the composition dependence of Γ_{GaAs} is explained by the strain near the interface due to the lattice mismatch. Figure 4 implies that compressive ($x>0.07$) or tensile ($x<0.07$) stress exists in the GaAs substrate near the interface.

If there is homogeneous strain in the penetration depth of the incident laser light (~ 100 nm), the strain ϵ exhibits the maximum value at $x=0$ and 0.13 and is calculated to be about 3×10^{-3}. Here, we used the relationship between Γ_{GaAs} and the strain in GaAs epitaxial films[11] for calculations. However, the strain-induced frequency shift was not clearly observed: It is below our reproducibility limit of about 0.3 cm^{-1}. A phenomenological theory[12] deduces the strain of $\sim 1\times10^{-3}$ from a frequency shift of 0.3 cm^{-1} at most. Raman spectroscopy of the GaAs substrate shows that there exists a small misfit strain of the order of 10^{-3} or less near the interface.

In conclusion, we have successfully examined the disorder and strain in lattice-mismatched ZnS_xSe_{1-x}/GaAs heterostructures by means of Raman spectroscopy. The disorder and the phonon coherence length in epitaxial ZnS_xSe_{1-x} films were deduced from the linewidth of the ZnSe-like LO phonon. The strain at the interface was evaluated from the linewidth of the GaAs LO phonon. The experimental and analytical procedures demonstrated in this work are expected to be useful for the microscopic characterization of semiconductor heterostructures.

Part of this work was done at the Cryogenic Center, University of Tsukuba.

[1] See, for example, Proceedings of the 5th International Conference on II-VI Compounds, Tamano, 1991 (to be published).
[2] P. Parayanthal and F. H. Pollak, Phys. Rev. Lett. 52, 1822 (1984).
[3] A. Krost, W. Richter, and O. Brafman, Appl. Phys. Lett. 56, 343 (1990).
[4] O. Brafman, D. Fekete, and R. Sarfaty, Appl. Phys. Lett. 58, 400 (1991).
[5] A. Yamamoto, Y. Yamada, and Y. Masumoto, Appl. Phys. Lett. 58, 2135 (1991).
[6] O. Brafman, I. F. Chang, G. Lengyel, S. S. Mitra, and E. Carnall, Jr., Phys. Rev. Lett. 19, 1120 (1967).
[7] H. Richter, Z. P. Wang, and L. Ley, Solid State Commun. 39, 625 (1981).
[8] K. Hayashi, N. Sawaki, and I. Akasaki, Jpn. J. Appl. Phys. 30, 501 (1991).
[9] D. J. Olego, K. Shahzad, D. A. Cammack, and H. Cornelissen, Phys. Rev. B 38, 5554 (1988).
[10] A. B. Barber, Jr. and A. J. Sievers, Rev. Mod. Phys. 47, S1 (1975).
[11] Y. Huang, P. Y. Yu, M. N. Charasse, Y. Lo, and S. Wang, Appl. Phys. Lett. 51, 192 (1987).
[12] H. Shen and F. H. Pollak, Appl. Phys. Lett. 45, 692 (1984).

Ultraviolet stimulated emission and optical gain spectra in $Cd_xZn_{1-x}S$-ZnS strained-layer superlattices

Yoichi Yamada and Yasuaki Masumoto
Institute of Physics, University of Tsukuba, Tsukuba, Ibaraki 305, Japan

John T. Mullins and Tsunemasa Taguchi
Department of Electrical Engineering, Faculty of Engineering, Osaka University, Suita, Osaka 565, Japan

(Received 29 April 1992; accepted for publication 24 August 1992)

Stimulated emission at 374.9 nm has been observed in an optically pumped $Cd_{0.22}Zn_{0.78}S$-ZnS strained-layer superlattice at room temperature. Using a pump-and-probe technique with nanosecond excitation pulses, optical gain has also been observed at the tail part of the $n=1$ heavy-hole exciton absorption spectrum in the presence of the clear absorption peak of the exciton. Our experimental results suggest that the stimulated emission originates from excitonic gain.

Much progress has recently been made in the application of wide-band-gap II-VI compound semiconductor heterostructures, especially those based on CdZnSe-ZnSe quantum well systems, for injection laser diodes[1,2] and display devices[3,4] operating in the blue-green region of the spectrum. It is through the successful development of doping techniques for *p*-type conductivity control that these device applications have been achieved. Furthermore, there has been much work on optically pumped laser operation in a variety of wide-band-gap II-VI multiple quantum well (MQW) structures and double heterostructures such as ZnSe-ZnMnSe,[5] CdZnSe-ZnSSe,[6] CdZnSe-CdZnSSe,[7] ZnSe-ZnSSe,[8,9] and CdZnTe-ZnTe.[10] These studies have enabled us to understand the fundamental lasing characteristics of each of these systems.

Among wide-band-gap II-VI compound semiconductors with zincblende structures, ZnS has the largest band-gap energy (3.73 eV at room temperature), so that ZnS-based MQW structures exhibit fundamental absorption edges at the shortest wavelengths. Moreover, ZnS has a relatively large exciton binding energy of about 40 meV. Therefore, quasi-two-dimensional excitons in quantum wells may have very large binding energies due to the effect of the quantum confinement. In this letter, we demonstrate ultraviolet stimulated emission in optically pumped $Cd_xZn_{1-x}S$-ZnS strained-layer superlattices (SLSs) at room temperature (RT). This type of SLS has previously been proposed and fabricated by Endoh *et al.*[11–13] We also present optical gain spectra for this SLS measured by means of a pump-and-probe technique employing nanosecond excitation pulses. These experimental results suggest that the origin of optical gain is different from that of III-V MQW systems in which an electron-hole plasma plays a principal role in providing gain.

Cubic-structured $Cd_xZn_{1-x}S$-ZnS SLSs were grown by low-pressure metalorganic chemical vapor deposition (MOCVD) using all gaseous sources on (100)-oriented GaAs substrates, following the deposition of a 1.5-μm-thick ZnS buffer layer. The MQW structures used in this study consist of 50 periods of 4.1-nm thick $Cd_xZn_{1-x}S$ well layers separated by 8.1-nm thick ZnS barrier layers. The Cd composition ratio in the ternary alloy well layer was varied from $x=0.11$ to $x=0.49$. In this case, the ternary alloy well layers are under biaxial compression and the lattice mismatch between the well and barrier layers varies from approximately 0.8% to 3.8%. The individual well and barrier layers are believed to be within the critical layer thickness because the critical layer thickness of a ZnSe-ZnS SLS with a large lattice mismatch of about 4.5% has been determined to be about 10 nm by transmission electron microscopy.[14]

Figure 1 shows absorption (solid lines) and photoluminescence (dashed lines) spectra at 10 K taken from $Cd_xZn_{1-x}S$-ZnS SLSs with various Cd composition ratios in the ternary alloy well layer (*a*:$x=0.11$, *b*:$x=0.22$, *c*:$x=0.31$, *d*:$x=0.42$, and *e*:$x=0.49$). The absorption spectra were measured after removal of the GaAs substrate by chemical etching. The photoluminescence (PL) spectra were obtained under weak excitation using a continuous-wave He-Cd laser (325 nm). It can be seen from this figure that the effective band-gap energy of this type of SLS varies widely within the ultraviolet spectral region according to the composition x of the $Cd_xZn_{1-x}S$ well layer. Moreover, this type of SLS exhibits a strong excitonic emission band even at room temperature. The band lineup of this type of SLS has been found to always be type I on the basis of our semiquantitative calculations that modify the model-solid theory[15] and photoluminescence excitation (PLE) measurements.[16] The dominant excitonic emission band in each SLS shown in Fig. 1 is attributable to radiative recombination of $n=1$ heavy-hole excitons localized at interface and compositional fluctuations in the ternary alloy well layer. With increasing Cd mole fraction x, the Stokes shift becomes larger as well as the linewidth of both the absorption and emission spectra. This may be due to increases in interface fluctuations, compositional fluctuations, and the lattice mismatch strain. However, the dominant cause is not clearly understood at the present time.

The samples mentioned above were cleaved to approximately 1-mm long resonators with uncoated facets and excited perpendicular to the MQW layer plane. The excitation source was a frequency-tripled *Q*-switched Nd^{3+}:YAG laser (355 nm). The pulse width was approximately 5 ns and the repetition rate was 30 Hz. We also

 0003-6951/92/432190-03$03.00

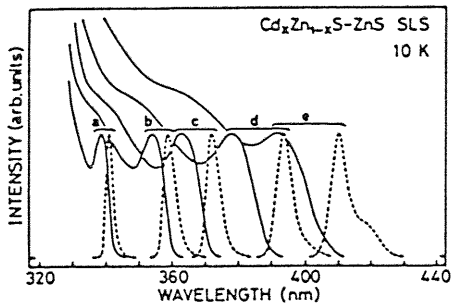

FIG. 1. Absorption (solid lines) and photoluminescence (dashed lines) spectra taken from $Cd_xZn_{1-x}S$-ZnS SLSs at 10 K with various Cd composition rates in the ternary alloy well layer (a:x=0.11, b:x=0.22, c:x=0.31, d:x=0.42, and e:x=0.49).

employed a N_2 pulsed laser (337 nm, 3 ns, and 30 Hz) as the excitation source for the sample labeled *a* in Fig. 1. Edge emission from one of the facets of the sample was detected using an optical multichannel analyzer in conjunction with 1-m or 25-cm single grating monochromators. For the sample with a Cd composition of $x=0.22$ in the ternary alloy well layer, stimulated emission spectra (SE; dotted lines) observed from the cleaved facet at 10 K and RT are shown in Figs. 2(a) and 2(b), respectively. In this figure, absorption spectra (ABS; solid lines) and photoluminescence spectra (PL; dashed lines) observed from the front face of the sample are also shown. The peak position of the stimulated emission is located at 361.2 nm at 10 K and is shifted to 374.9 nm at RT. Figure 3 shows the edge emission intensity at 10 K, 80 K, 150 K, 225 K, and RT as a function of excitation power density. The threshold excitation power density for stimulated emission is about 7 kW/cm^2 at 10 K. This value increases gradually with temperature, and the room-temperature threshold is

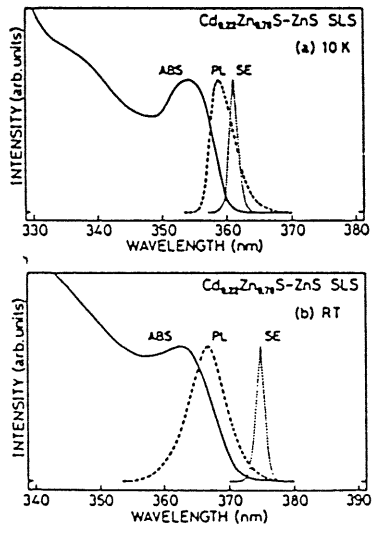

FIG. 2. Stimulated emission spectra (SE; dotted lines) from the edge facet of a $Cd_{0.22}Zn_{0.78}S$-ZnS SLS at 10 K in (a) and at room temperature in (b). Absorption spectra (ABS; solid lines) and photoluminescence spectra (PL; dashed lines) from the front face of the sample at each temperature are also shown.

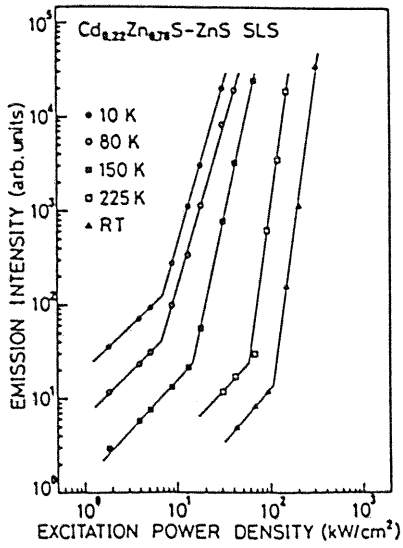

FIG. 3. Edge emission intensity of a $Cd_{0.22}Zn_{0.78}S$-ZnS SLS as a function of the excitation power density at different temperatures.

about 110 kW/cm^2. The conduction and valence band offsets in this sample have been estimated to be $\Delta E_c \approx 240$ meV and $\Delta E_v \approx 107$ meV (heavy-hole band), respectively, including the effects of the strain due to the lattice mismatch (1.7%).[16] These values are thought to be sufficient to confine both electrons and heavy holes in the quasi-two-dimensional potential wells up to room temperature.

Recently, Ding *et al.* have reported that excitons play a central role in the formation of optical gain in the CdZnSe-ZnSe MQW structures.[17] In order to study the mechanism of optical gain in our samples, pump-and-probe experiments with nanosecond excitation pulses were performed. The frequency-tripled Q-switched Nd^{3+}:YAG laser mentioned above was used as a pump source. As a probe source, amplified spontaneous emission from Exalite 376 dye solution, excited by a portion of the pump source, was used. The probe pulse covered the spectral range from approximately 360 to 390 nm. The spot of the probe pulse on the sample was 200 μm in diameter and spatially centered in the excitation spot of the pump pulse which was 2 mm in diameter. The time delay between pump and probe pulses was adjusted to be zero. Figure 4 shows pump-and-probe absorption spectra taken from a $Cd_{0.31}Zn_{0.69}S$-ZnS SLS at 10 K. The dashed line shows the absorption spectrum without the pump pulses while the solid line shows the spectrum with an excitation power density of approximately 253 kW/cm^2. The inset shows enlarged spectra in the tail region of the excitonic absorption peak at excitation power densities of (a) 18, (b) 65, (c) 143, (d) 193, and (e) 253 kW/cm^2. With increasing pump intensity, absorption around 375 nm gradually decreases. Above 143 kW/cm^2, negative absorption is observed and this increases with pump intensity. This observation unambiguously indicates the presence of gain. The stimulated emission observed in this sample was naturally located at 374.9 nm at 10 K, and the threshold excitation power density was es-

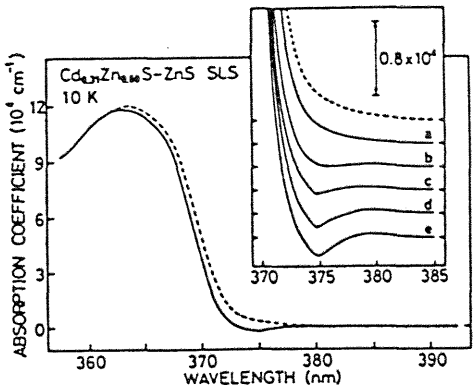

FIG. 4. Pump-and-probe absorption spectra taken from a $Cd_{0.31}Zn_{0.69}S$-ZnS SLS at 10 K. The dashed line shows the absorption spectrum without the pump pulses. The solid line shows the spectrum with an excitation power density of about 253 kW/cm^2. The inset shows the enlarged spectra at the tail part of the excitonic absorption peak at excitation power densities of (a) 18, (b) 65, (c) 143, (d) 193, and (e) 253 kW/cm^2.

timated to be about 31 kW/cm^2. The pump intensity at which negative absorption appears is several times larger than the threshold for stimulated emission. This is due to the inhomogeneous excitation over 50 quantum wells (QWs) along the growth direction. In fact, the transmittance of the excitation pulse through the 50 QWs is estimated to be about 20%. Several QWs near the surface of the sample dominantly contribute to the stimulated emission. On the other hand, all of the 50 QWs, on the average, contribute to the optical gain which is observed in the pump-and-probe configuration.

The main feature of our experimental findings is the observation of optical gain even in the presence of the clear excitonic absorption peak which is slightly bleached at the lower energy side. This result suggests that excitons contribute to the formation of optical gain and, moreover, there is no evidence for the presence of an electron-hole plasma. As for the mechanism of excitonic gain in quantum wells, the contribution of excitons themselves in inhomogeneous broadening,[17] the contribution of localized excitons, or the contribution of excitonic molecules will be adopted. In order to elucidate this mechanism, more detailed experimental and theoretical analyses are required and are currently underway.

In conclusion, ultraviolet stimulated emission has been demonstrated in optically pumped $Cd_{0.22}Zn_{0.78}S$-ZnS SLS at room temperature. The stimulated emission observed in this study is characterized by the shortest wavelength (374.9 nm) reported to date in wide-band-gap II-VI MQW structures. It has also been suggested by pump-and-probe experiments that the mechanism of optical gain is due to the excitonic process.

This work was partly supported by a Grant-in-Aid for Scientific Research on Priority Areas, New Functionality Materials-Design, Preparation, and Control No. 03205014, from the Ministry of Education, Science and Culture of Japan.

[1] M. A. Haase, J. Qiu, J. M. DePuydt, and H. Cheng, Appl. Phys. Lett. 59, 1272 (1991).
[2] H. Jeon, J. Ding, W. Patterson, A. V. Nurmikko, W. Xie, D. C. Grillo, M. Kobayashi, and R. L. Gunshor, Appl. Phys. Lett. 59, 3619 (1991).
[3] W. Xie, D. C. Grillo, R. L. Gunshor, M. Kobayashi, G. C. Hua, N. Otsuka, H. Jeon, J. Ding, and A. V. Nurmikko, Appl. Phys. Lett. 60, 463 (1992).
[4] H. Jeon, J. Ding, A. V. Nurmikko, W. Xie, M. Kobayashi, and R. L. Gunshor, Appl. Phys. Lett. 60, 892 (1992).
[5] R. N. Bylsma, W. M. Becker, T. C. Bonsett, L. A. Kolodziejski, R. L. Gunshor, M. Yamanishi, and S. Datta, Appl. Phys. Lett. 47, 1039 (1985).
[6] Y. Kawakami, S. Yamaguchi, Y.-H. Wu, K. Ichino, Sz. Fujita, and Sg. Fujita, Jpn. J. Appl. Phys. 30, L605 (1991).
[7] K. Ichino, Y.-H. Wu, Y. Kawakami, Sz. Fujita, and Sg. Fujita, J. Cryst. Growth 117, 527 (1992).
[8] K. Nakanishi, I. Suemune, Y. Fujii, Y. Kuroda, and M. Yamanishi, Appl. Phys. Lett. 59, 1401 (1991).
[9] G. Sun, K. Shahzad, J. M. Gaines, and J. B. Khurgin, Appl. Phys. Lett. 59, 310 (1991).
[10] D. Lee, A. M. Johnson, J. E. Zucker, C. A. Burrus, R. D. Feldman, and R. F. Austin, Appl. Phys. Lett. 60, 739 (1992).
[11] Y. Endoh and T. Taguchi, Mater. Res. Soc. Symp. Proc. 161, 211 (1990).
[12] T. Taguchi and Y. Endoh, Jpn. J. Appl. Phys. 30, L952 (1991).
[13] T. Taguchi, Y. Endoh, and Y. Nozue, Appl. Phys. Lett. 59, 3434 (1991).
[14] Y. Kawakami, T. Taguchi, and A. Hiraki, J. Cryst. Growth 89, 331 (1988).
[15] C. G. Van de Walle, Phys. Rev. B 39, 1871 (1989).
[16] Y. Yamada, Y. Masumoto, and T. Taguchi (unpublished).
[17] J. Ding, H. Jeon, T. Ishihara, A. V. Nurmikko, H. Luo, N. Samarth, and J. Furdyna, Surf. Sci. 267, 616 (1992); A. V. Nurmikko, R. L. Gunshor, and M. Kobayashi, J. Cryst. Growth 117, 432 (1992).

Higher order zone-folded modes in ZnSe-ZnS strained-layer superlattices

Aishi Yamamoto, Yoshihiko Kanemitsu, and Yasuaki Masumoto
Institute of Physics, University of Tsukuba, Tsukuba, Ibaraki 305, Japan

Shigeki Yamaga and Akihiko Yoshikawa
Department of Electrical and Electronics Engineering, Chiba University, Inage-ku, Chiba 263, Japan

(Received 26 May 1992; accepted for publication 29 July 1992)

Higher order (up to the 5th order) zone-folded acoustic modes in ZnSe-ZnS strained-layer superlattices (SLSs) were observed by means of Raman scattering. Structural characterization of both periodicity of superlattices and roughness of the interface was done by means of transmission electron microscopy (TEM). The Raman spectrum of zone-folded modes was well explained by the theoretical calculation which takes account of two observed structural characteristics of the sample, the periodicity of the superlattices, and the roughness of the interface. This clearly shows the strain does not matter to the observation of the zone-folded modes.

Raman spectroscopy is a very useful tool to study lattice dynamics in semiconductor low-dimensional structures as well as bulk semiconductors. In the case of superlattices, new behavior of phonons, such as zone folding of acoustic phonons and confinement of optical phonons, are studied extensively.[1] The spectra are sensitive to the periodicity, the roughness of the interface, and the stress. Most of II-VI semiconductors superlattices have a biaxial stress at the heterojunction interface due to the lattice mismatch. For example, stress-induced peak shifts of optical phonons were observed in strained-layer superlattices (SLSs).[2] The spectra of zone-folded acoustic phonons were broad and only the first or second order was observed.[3,4] One speculates that the lattice mismatch makes it difficult to establish high-quality epitaxial layers and to observe zone-folded modes.

The stress comes from two types of lattice mismatch which exists between SLSs and a substrate, and between the alternate layers in the SLSs. In this work, we were able to observe higher order doublet phonon modes, up to the 5th order, in ZnSe-ZnS SLSs whose average lattice constant[5] is equal to that of a GaAs substrate. We tried to answer two questions here. One is why such higher order folded modes were observed. The other is whether or not the stress matters to the zone folding of phonon modes. A model calculation based on the transmission electron microscopy (TEM) data was used to consider these problems and it reproduced our zone-folded spectrum. It was found that our Raman spectrum reflects dominantly both the periodicity of the superlattices and the roughness of the interface rather than the stress.

A sample used in this work was ZnSe-ZnS SLSs grown by metalorganic molecular beam epitaxy (MOMBE) on a (100) GaAs substrate.[5] The designed thickness of ZnSe and ZnS layers were 200 and 10 Å, respectively. The average lattice constant of the SLSs was equal to the GaAs substrate in order to reduce the stress between the SLSs and the substrate. Raman scattering measurements were performed at room temperature with the 4579 Å line of an Ar ion laser in a quasibackscattering configuration. Raman spectrum was obtained by a double monochromator (Spex; 1403) and a photomultiplier.

Figure 1(a) shows the Raman scattering spectrum of zone-folded longitudinal acoustic (LA) modes. The background was subtracted from the spectrum. It is probably originated from Rayleigh scattering and single particle excitations.[6] Figure 1(a) shows zone-folded doublet modes up to the 5th order. To our knowledge, it is the first observation of such higher order modes in II-VI SLSs. In the continuum limit, a phonon dispersion is given by the conventional Rytov model.[7] It is written by

$$\cos(qd)=\cos\left(\frac{\omega d_1}{v_1}\right)\cos\left(\frac{\omega d_2}{v_2}\right)-\frac{1+\kappa^2}{2\kappa}\sin\left(\frac{\omega d_1}{v_1}\right)\sin\left(\frac{\omega d_2}{v_2}\right), \quad (1)$$

where ω and q are the phonon frequency and the superlattice wave vector, v_1 and v_2 are the sound velocities of materials 1 and 2, d_1 and d_2 are the thicknesses of the two constituting layers, and d is the period defined by $d=d_1+d_2$. The coefficient κ is defined by $\kappa=v_1\rho_1/v_2\rho_2$, where ρ_1 and ρ_2 are the corresponding densities. The inset of Fig. 1(a) shows the phonon dispersion calculated by using Eq. (1). We have used $\rho_1=5.266$ g/cm^3 for ZnSe and $\rho_2=4.086$ g/cm^3 for ZnS.[8] The sound velocities used in this calculation were stress-free values in bulk crystals (ZnSe:$v_1=4.054\times10^5$ cm/s, ZnS:$v_2=5.047\times10^5$ cm/s).[8] The solid circles in the inset are observed peak frequencies of the folded modes. When the thicknesses d_1 and d_2 are designed values 200 and 10 Å, the calculated peak energies do not agree well with the observed ones. The period, d was estimated to be 205 Å from the x-ray diffraction measurement,[5] though the constituting layer thicknesses, d_1 and d_2, were not obtained exactly. Therefore, we fixed the period, d, to be 205 Å, and varied the layer thicknesses, d_1 and d_2, to fit the all of the observed frequencies of the zone-folded modes. The fitted values of d_1 and d_2 were 198 and 7 Å, respectively. These values were used to calculate the dispersion shown in the inset of Fig. 1(a). The calculation fits the experimental data satisfactorily.

So far, zone-folded modes were observed in ZnTe-ZnSe[3] and InAs-AlAs[4] SLSs. It was suggested that the observed peak energies of the folded modes do not com-

 0003-6951/92/391700-03$03.00

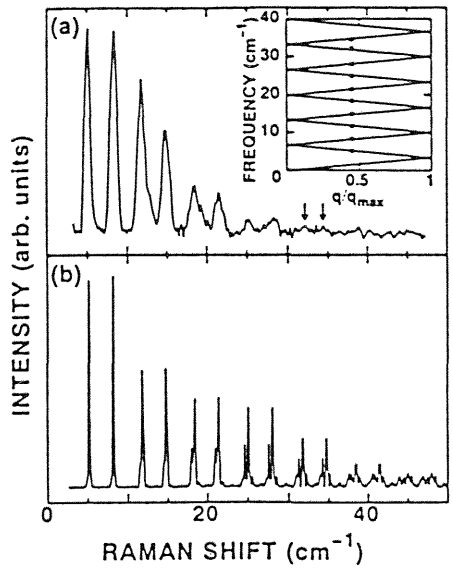

FIG. 1. Observed (a) and calculated (b) Raman spectra of zone-folded modes. The arrows show the peak positions of the fifth-order folded modes. Inset is phonon dispersion using conventional Rytov model, where q_{max} is the zone-edge wave vector π/d and d is the superlattice period.

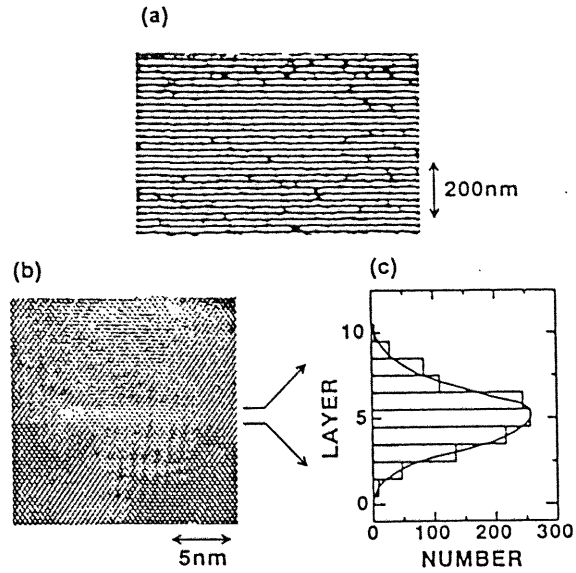

FIG. 2. Low- (a) and high- (b) resolution TEM images. (c) Histogram of the lattice points of ZnS. We obtained the data in the histogram by counting the lattice points of ZnS along the straight arrays of lattice points parallel to the interface plane. The solid line is a guide to the eye.

pletely agree with the calculated ones. This discrepancy was believed to be originated from the strain between the alternate layers. Recio *et al.*[4] considered the effect of the strain on the sound velocities deduced from the stress-induced peak shifts of LO-Raman modes and Grüneisen constants. We tried to include the stress effect on the sound velocities using their method. However, all the estimated peak energies were larger than the observed ones by ~ 0.2 cm^{-1}. The calculation does not fit the experimental data better than the stress-free calculation. Furthermore, it was found that the changing of the thicknesses by a few angstrom induces the peak shift of the folded modes more than the stress.

Figures 2(a) and 2(b) show low- and high-resolution TEM images of our sample, respectively. Figure 2(a) shows good periodicity of each layer. However, a large fluctuation exists near the interface, as shown in Fig. 2(b). Figure 2(c) shows the histogram of the lattice points of ZnS. We obtained each data in the histogram by counting the lattice points of ZnS along the straight arrays of lattice points parallel to the interface plane. The full width at half maximum (FWHM) of the histogram is about four layers and it is a little larger than the fitted values for the thickness of the ZnS layer, 7 Å. The position at the center of the ZnS layers is fluctuated. Therefore, the FWHM of the histogram is larger than the thickness of the ZnS layer.

The intensity of Raman scattering from the folded LA modes can be theoretically calculated by a photoelastic model, where the superlattices have bulk photoelastic coefficients P_1 and P_2.[9] The photoelastic model has been used previously to predict the intensity of the folded modes[10] and to characterize the periodicity and roughness of the interface[11] in GaAs-$Ga_xAl_{1-x}As$ superlattices. According to this model, the modulation of the photoelastic coefficient, $P(z)$, along the growth direction z reflects the modulation in the structure of the SLSs. The mth order folded modes at $\omega_m = |2m\pi/d \pm q| v_{sl}$ has intensity,

$$I_m \propto \omega_m (n_m + 1) |Q_m|^2, \tag{2}$$

where n_m is the Bose factor, v_{sl} is sound velocity of superlattices defined through $d/v_{sl} = d_1/v_1 + d_2/v_2$, and Q_m is the mth order Fourier component of $P(z)$. It is noted that we do not need the absolute values of P_1 and P_2, but need only the line shape of $P(z)$ in order to calculate the intensity of Raman spectrum.

When $P(z)$ is assumed to be a square-wave function, in an ideal case, the higher order Fourier component Q_m decreases very slowly. This means that the higher order I_m decreases very slowly. Since the square-wave assumption cannot reproduce our spectrum at all, we took account of the fluctuation of the periodicity and the interface roughness using the TEM data. The roughness of the interface was directly deduced from the distribution of ZnS layers, as shown in Fig. 2(c). The fluctuation of the periodicity, that is the fluctuation of the ZnSe layer thickness, was deduced from two-dimensional densitometric data of the low-resolution TEM image [Fig. 2(a)]. Thus, the profile of $P(z)$ was obtained by taking account of the fluctuation of the periodicity and the roughness of the interface. Figure 3(a) shows the obtained profile of $P(z)$. The intervals between the peaks, that is the fluctuation of the periodicity, are shown in Fig. 3(a). Figure 3(b) shows the Fourier power spectrum, $|Q(k)|^2$ where k is the wave number defined by $k = 2\pi/z$. Several peaks show the mth order Fourier components. The roughness of the interface and the fluctuation of the periodicity cause the decrease of the higher order Q_m. The fluctuation of the periodicity also causes the broadening of the higher order Q_m. By using Eq. (1) and the Fourier components Q_m, the Raman spectrum

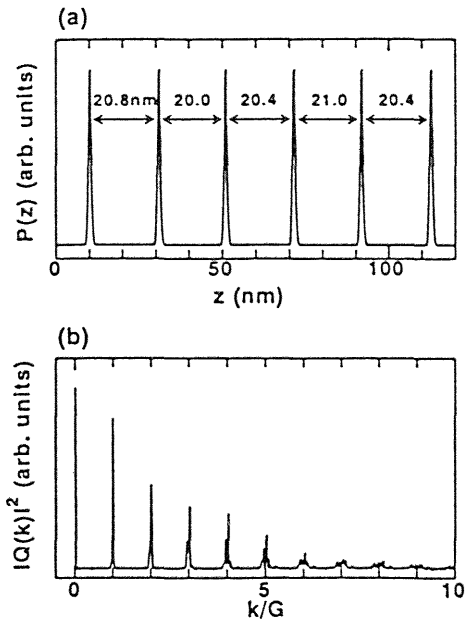

FIG. 3. (a) Photoelastic coefficient $P(z)$ deduced from the TEM images. The intervals between the peak points are shown in the figure, showing the fluctuation of the periodicity. (b) Fourier power spectrum of $P(z)$. G is defined by $G=2\pi/d$, where d is the superlattice period.

of zone-folded modes was calculated, as shown in Fig. 1(b). The Raman spectrum reproduces the experimental data in the following two essential points: the higher order modes become wider and more than 6th order modes reduce their height obviously. In this calculation, we have assumed that the roughness of each layer interface is the same. If the roughness of each layer interface is taken into account, the intensity of the higher order zone-folded modes decreases more and the model calculation reproduces the Raman spectrum more precisely.

In conclusion, we have observed higher order (up to the 5th order) zone-folded acoustic modes in ZnSe-ZnS strained-layer superlattices (SLSs) by means of Raman scattering. We were able to reproduce our zone-folded spectrum using TEM data and a photoelastic model. The agreement between our calculation and the measurement shows that the Raman spectrum reflects dominantly the periodicity of the superlattices and the roughness of the interface.

The authors would like to thank Hitachi Research Laboratory for providing TEM images, and K. Nagao of Fuji Photo Film Co., Ltd. for acquiring two-dimensional densitometric data. Part of this work was done at the Cryogenic Center, University of Tsukuba. This work is partially supported by the Iketani Science and Technology Foundation.

[1] See, for example, *Light Scattering in Solids V*, edited by M. Cardona and G. Güntherodt (Springer, New York, 1989), Vol. 66.
[2] A. Yamamoto, Y. Yamada, and Y. Masumoto, Appl. Phys. Lett. 58, 2135 (1991).
[3] Y. H. Wu, H. Yang, A. Ishida, H. Fujiyasu, S. Nakashima, and K. Tahara, Appl. Phys. Lett. 54, 239 (1989).
[4] M. Recio, G. Armelles, A. Ruiz, A. Mazuelas, and F. Briones, Appl. Phys. Lett. 54, 804 (1989).
[5] H. Oniyama, S. Yamaga, and A. Yoshikawa, Jpn. J. Appl. Phys. 28, L2137 (1989).
[6] M. V. Klein, in *Light Scattering in Solids*, edited by M. Cardona (Springer, New York, 1975), Vol. 8, p. 148.
[7] S. M. Rytov, Akust. Zh. 2, 71 (1956) [Sov. Phys. Acoust. 2, 68 (1956)].
[8] Landolt-Börnstein, *Numerical Data and Functional Relationships in Science and Technology* (Semiconductors-Physics of II-VI and I-VII Compounds, Semimagnetic Semiconductors), edited by O. Madelung, M. Schulz, and H. Weiss (Springer, Berlin, 1989), Vol. 17(b), p. 145.
[9] C. Colvard, T. A. Gant, M. V. Klein, R. Merlin, R. Fischer, H. Morkoç, and A. C. Gossard, Phys. Rev. B 31, 2080 (1985).
[10] M. V. Klein, C. Colvard, R. Fischer, and H. Morkoç, J. Phys. (Paris) Colloq. C 5, C5-131 (1984).
[11] S. K. Hark, B. A. Weinstein, and R. D. Burnham, J. Appl. Phys. 62, 1112 (1987).

Anomalous change of extinction spectra of CuCl-microcrystals

Yasuaki Masumoto, Tetsuro Wamura, and Tomohiro Kawamura
Institute of Physics, University of Tsukuba, Tsukuba, Ibaraki 305, Japan

(Received 3 December 1990; accepted for publication 20 February 1991)

Optical transmission spectra of CuCl microcrystals embedded in NaCl crystals were studied around the Z_3 exciton resonance by varying the annealing time. With the increase in the annealing time, extinction spectra of the Z_3 exciton change anomalously from the absorption-type spectrum to the emission-type spectrum via the dispersion-type spectrum. The Mie theory [Ann. Phys. 25, 377 (1908)] successfully explains the spectral change due to the growth of microcrystals. We report here for the first time an anomalous change of the exciton spectra due to the growth of semiconductor microcrystals.

Recently much interest has been taken in the linear and nonlinear optical properties of semiconductor microcrystals. Quantum confinement of electrons, holes, and excitons have been typically observed in CdS, CdSe, or CuCl microcrystals.[1] Especially, quantum confinement of excitons is well observed in CuCl microcrystals. Quantum confined excitons in CuCl microcrystals show blue shifts in the absorption spectra. In addition, the quantum confined excitons exhibit unique optical nonlinearities.[2] So far, the blue shift or the asymmetric line shape with a high-energy tail of the exciton absorption spectrum has been used to know the microcrystal size or size distribution.[3,4] However, the blue shift is detectable only for microcrystals whose radius is smaller than 10 nm. The all-optical means to estimate the arbitrary size of microcrystals is desirable. For the development of the all-optical means, the full understanding of the exciton absorption spectrum of microcrystals is important. It is also useful for the nonlinear optical study of microcrystals.

In this study, we studied the optical transmission spectra of annealed samples of CuCl microcrystals embedded in NaCl host crystals. We found the anomalous change of Z_3 exciton transmission spectra from the absorption-type spectrum to the emission-type spectrum via the dispersion-type spectrum with the increase of the annealing process time. The anomalous change was successfully explained by the Mie theory. Comparing the transmission spectra with the Mie calculation gives a unique optical method to estimate the microcrystal size. We demonstrated here that our all-optical method is useful to estimate the size of CuCl microcrystals.

Samples were grown from the molten NaCl doped with CuCl by the transverse Bridgman method. Many pieces of platelets were cleaved from a small block which was a part of a grown crystal rod. Their sizes were approximately $4\times4\times0.3$ mm^3. The doped CuCl concentration was determined to be 0.16 mol% by the inductively coupled plasma optical emission spectroscopy. Optical transmission spectrum of a platelet at 77 K is shown in Fig. 1(a). The vertical axis shows the extinction coefficient. It was simply calculated by $\ln(I_{in}/I_{out})/d$, where I_{in}, I_{out}, and d are the incident light intensity, the transmitted light intensity, and the sample thickness, respectively. The spectrum peak shows a blue shift of the Z_3 exciton by 3.6 meV from the bulk crystal. Asymmetric line shape with a high-energy tail is due to the size distribution of the microcrystals. Platelets were annealed for 5, 40, 135, 320, or 625 min at 232 °C in vacuum. Transmission spectra of them at 77 K are shown in Figs. 1(b), 1(c), 1(d), 1(e), and 1(f). The Z_3 exciton structure in Fig. 1(b) is symmetric and is lower in height than that in Fig. 1(a). The Z_3 exciton structure in Figs. 1(c), 1(d), and 1(e) shows the dispersion-type structure. The structure in Fig. 1(f) shows the emission-type structure.

The similar spectral change is also observed around the $Z_{1,2}$ exciton resonance as is seen in Fig. 1. With the increase in annealing temperature, the same change takes place more sensitively depending on the annealing time. Reversely, with the decrease in annealing temperature, the

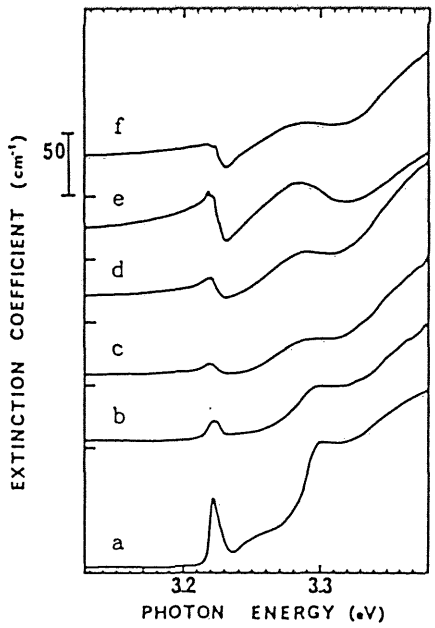

FIG. 1. Extinction spectra of CuCl microcrystals embedded in NaCl host crystals at 77 K. The spectrum *a* is the spectrum of a nonannealed sample. The peak energy shifts by 3.6 meV from the bulk position, which indicates that the radius of the microcrystal is 7 nm. The spectra *b*, *c*, *d*, *e*, and *f* are the spectra of samples annealed at 232 °C. The annealing time is 5 min for *b*, 40 min for *c*, 135 min for *d*, 320 min for *e*, and 625 min for *f*.

 0003-6951/91/202270-03$02.00

change becomes dull. We also measured the transmission spectra at 2 K to check the thermal broadening of the structure at 77 K. However, the structure changes little except an energy shift of 15 meV.

To our knowledge, this observation is the first report about the anomalous change of the exciton extinction structure in semiconductors. However, there are reports about the similar variation of the absorption bands in interstellar grains.[5,6] The phenomena have been interpreted by applying the Mie theory to the extinction spectra around the resonance line of the absorption bands. Therefore, we follow the similar analysis procedure.

We adopted the Lorentz oscillator model to describe the Z_3 exciton dispersion relation for simplicity. It is the one-oscillator model. The dielectric constant ϵ is described by the equation:

$$\epsilon=\epsilon_b[1+E_l^2/(E_t^2-E^2-i\gamma E)]\,, \qquad (1)$$

where $\epsilon_b = 5.0$ is the background dielectric constant, $E_t = 3.2025$ eV is the transverse exciton energy, $E_l = 3.2080$ eV is the longitudinal exciton energy,[7] and $\gamma = 1.49$ meV is the damping constant. The damping constant γ is determined to describe the experimental ϵ_2 (imaginary part of dielectric constant) well.[8]

The mathematical procedures of the Mie calculation are as follows:[5] Suppose a microcrystal sphere is placed in the incident light flux. The electromagnetic fields at all the space points are expanded by the infinite series of Bessel functions. Here the Maxwell boundary condition is imposed on the fields at the boundary between a microcrystal sphere and the surrounding medium. Then, the scattering intensity and the transmission intensity of light are calculated at an imaginary sphere around the microcrystal and the intensities are integrated. In this way, we can calculate the scattering intensity, the extinction intensity and the absorption intensity which is equal to the extinction intensity minus the scattering intensity.

The calculation based on the Mie theory was numerically done by using the subroutine BHMIE.[5] Here, we assumed that CuCl microcrystals are spheres with a radius of a. The ϵ_1 (real part of dielectric constant) of NaCl host crystals is 2.457 around the Z_3 exciton resonance of CuCl and ϵ_2 of NaCl is assumed to be zero. Calculated spectra depending on the CuCl radius a divided by light wavelength λ are shown in Fig. 2. The light wavelength λ is fixed to be 387 nm. The vertical scale shows extinction, scattering, and absorption efficiencies by a CuCl microcrystal. The extinction efficiency is the sum of the scattering and absorption efficiencies. The efficiency is defined as the cross section divided by πa^2. The extinction cross section multiplied by the number density of microcrystals gives the extinction coefficient.

While the condition $a \ll \lambda$ holds, the electrostatic approximation is valid.[5] Then, the absorption efficiency increases in proportion to a with the increase in a. On the other hand, the scattering efficiency increases in proportion to a^4. Such scattering is referred to as Rayleigh scattering. The increase saturates as a/λ approaches to 0.1. When a/λ is 0.01, the line shape of the extinction efficiency spectrum

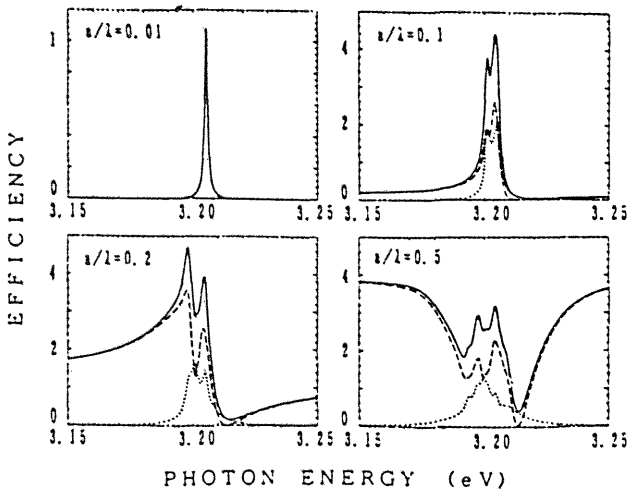

FIG. 2. Calculated extinction, scattering, and absorption efficiency spectra of a CuCl microcrystal embedded in an NaCl host crystal. The extinction, scattering, and absorption efficiency spectra are shown by solid, dashed, and dotted lines, respectively. The upper left, upper right, lower left, and lower right spectra correspond to conditions $a/\lambda = 0.01$, 0.1, 0.2, and 0.5, respectively.

is almost symmetric and most of the extinction comes from the absorption. The extinction spectrum shows a peak at the energy where $-\epsilon_1$ of CuCl is equal to twice ϵ_1 of NaCl. The peak is ascribed to the Fröhlich mode.[5] When a/λ is 0.1, the extinction spectrum becomes somewhat asymmetric and has a double-peak structure. Higher energy peak is ascribed to the Fröhlich mode and the lower energy peak to the low-frequency mode.[9] The scattering overwhelms the absorption. When a/λ is 0.2, the extinction spectrum is the dispersion type. The low-frequency mode overwhelms the Fröhlich mode. The scattering spectrum dominates the extinction spectrum. When a/λ is 0.5, the extinction spectrum is the emission type. The scattering dominates the extinction spectrum. The spectrum consists of multiple peaks which are ascribed to Fröhlich modes and low-frequency modes. The physical origin of the increase of modes is the increasing contribution of the higher-order electric-type and magnetic-type normal modes in the sphere with an increase in the radius.

In reference to the linear and nonlinear optical properties of semiconductor mycrocrystals, the local field effect in the electrostatic approximation has been considered for ultrasmall Rayleigh semiconductor microcrystals.[10,11] However, the treatment is not sufficient for CuCl microcrystals whose radius is larger than 0.1λ, because of the serious contribution of the scattering efficiency and the breakdown of the electrostatic approximation.

The calculated spectral change well explains the experimentally observed spectral change. With the increase in the annealing time, the size of CuCl microcrystals increases. As a result, the extinction spectra around the Z_3 exciton resonance change from the absorption type to the emission type via the dispersion type.

To compare the experimental extinction spectra with the calculated spectra, we took into account a size distri-

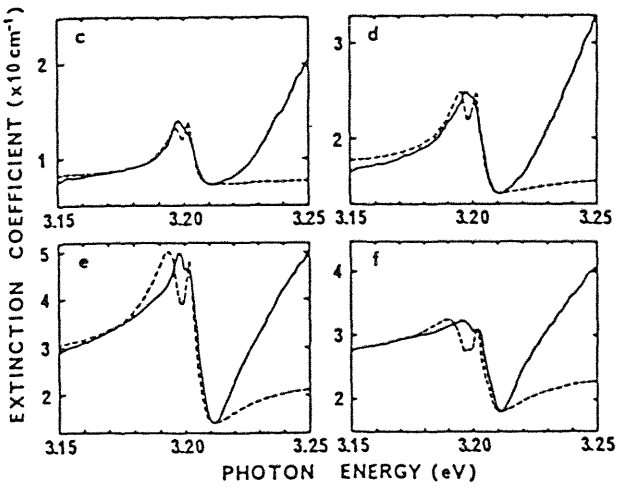

FIG. 3. Experimental (solid line) and calculated (dashed line) extinction spectra of CuCl microcrystals in NaCl host crystals. Figures *c*, *d*, *e*, and *f* correspond to Figs. 1(c), 1(d), 1(e), and 1(f), respectively. The horizontal energy scale is shifted by energy difference 15 meV between the Z_3 exciton resonance energies at 77 and 4.2 K. The vertical scales for the calculated spectra are chosen to be arbitrary to fit the experimental data well. The parameter a/λ values for the best fitting in *c*, *d*, *e*, and *f* are 0.14, 0.17, 0.20, and 0.25, respectively.

bution of the CuCl microcrystals. Larger microcrystals grow through the dissolution process of small microcrystals, the diffusion process and the recondensation process at larger microcrystals. In this case, the size distribution of CuCl microcrystals is considered to follow the Lifshitz–Slezov distribution.[4,12] The extinction spectrum is calculated by the integral

$$\int_0^{3/2} \pi a^2 P(a/\bar{a}) Q(E,a) d(a/\bar{a}) ,$$

where $\bar{a}$ is the average radius of microcrystals, $P(a/\bar{a})$ is the Lifshitz–Slezov distribution, and $Q(E,a)$ is the extinction efficiency spectrum of the microcrystal with a radius of a.

The experimental extinction spectra and fitted spectra are shown in Fig. 3. The experimental extinction spectra and calculated spectra by the Mie theory agree fairly well with each other. Disagreement at the high-energy side of the Z_3 exciton resonance is ascribed to the neglected contribution to ϵ of the $Z_{1,2}$ excitons. We can estimate the approximate size of CuCl microcrystals by comparing the shape of the extinction spectra. The estimated radii of CuCl microcrystals for extinction spectra of Figs. 1(c), 1(d), 1(e), and 1(f) are 54, 66, 77, and 97 nm, respectively. As demonstrated here, the calculation based on the Mie theory is useful to estimate the radius of the CuCl microcrystals. This all-optical method is useful for CuCl Mie microcrystals whose radius a is in an order of 0.1 λ.

In summary, we observed the anomalous change of the extinction spectra of CuCl microcrystals embedded in NaCl host crystals with the increase of the annealing time. The Z_3 exciton structure changes from the absorption type to the emission type via the dispersion type. The Mie theory successfully explains the spectral change due to the microcrystal growth. Comparing the extinction spectra with the Mie calculation gives a unique all-optical method to estimate the microcrystal size. This report presents the first observation of the anomalous change of the exciton spectrum due to the growth of semiconductor microcrystals.

This work is partially supported by Nippon Sheet Glass Foundation for Materials Science.

[1] A. I. Ekimov, Al. L. Efros, and A. A. Onushchenko, Solid State Commun. 56, 921 (1985).
[2] Y. Masumoto, M. Yamazaki, and H. Sugawara, Appl. Phys. Lett. 53, 1527 (1988).
[3] T. Itoh, Y. Iwabuchi, and M. Kataoka, Phys. Status Solidi B 145, 567 (1988).
[4] A. I. Ekimov, A. A. Onushchenko, A. G. Plyukhin, and Al. L. Efros, Sov. Phys. JETP 61, 891 (1985).
[5] C. F. Bohren and D. R. Huffman, *Absorption and Scattering of Light by Small Particles* (Wiley, New York, 1983).
[6] D. R. Huffman, Adv. Phys. 26, 129 (1977).
[7] Y. Masumoto, Y. Unuma, Y. Tanaka, and S. Shionoya, J. Phys. Soc. Jpn. 47, 1844 (1979).
[8] W. Staude, Phys. Lett. A 29 228 (1969).
[9] R. Fuchs and K. L. Kliewere, J. Opt. Soc. Am. 58, 319 (1968).
[10] K. C. Rustagi and C. Flytzanis, Opt. Lett. 9, 344 (1984).
[11] S. Schmitt-Rink, D. A. B. Miller, and D. S. Chemla, Phys. Rev. B 35, 8113 (1987).
[12] I. M. Lifshitz and V. V. Slezov, Sov. Phys. JETP 35, 331 (1959).

Size-dependent homogeneous linewidth of Z_3 exciton absorption spectra in CuCl microcrystals

Tetsuro Wamura, Yasuaki Masumoto, and Tomohiro Kawamura
Institute of Physics, University of Tsukuba, Tsukuba, Ibaraki 305, Japan

(Received 23 April 1991; accepted for publication 8 July 1991)

Size-dependent homogeneous linewidth of Z_3 exciton absorption spectra in CuCl microcrystals was measured at 2 K by the pump-and-probe spectroscopy. Observation of the hole burning gave us the homogeneous linewidth. The size-dependent part of the homogeneous linewidth is inversely proportional to the square of the radius of microcrystals. This dependence is explained by a simple model that a generated exciton dephases through the scattering at the irregular surface of microcrystals.

Recently much interest has been taken in the electronic and optical properties of semiconductor quantum dots, because of their unique properties and potential for device application.[1,2] However, semiconductor quantum dots embedded in crystals or glasses have size inhomogeneity inherent in the preparation processes. The size inhomogeneity gives the scattering of the quantized energy and inhomogeneous broadening of the absorption spectra. Therefore, this obscures the nobel properties of semiconductor quantum dots. The breakthrough of the study of the quantum dots is to make uniform-size quantum dots in a regular array. An alternative approach is to select dot by dot and examine the properties of the dot. The approach we took in this study is the latter, the size-selective laser spectroscopy of quantum dots.[3–7]

The samples we studied are CuCl microcrystals embedded in NaCl crystals where quantum confinement of excitons has been typically observed.[1] Quantum confined Z_3 excitons in CuCl microcrystals show blue shifts and the inhomogeneous size distribution causes broadening in the absorption spectra. We measured homogeneous linewidth of excitons in CuCl microcrystals by the hole-burning experiment. We performed the experiments in the pump-and-probe configuration and picked up the homogeneous linewidth from the inhomogeneously broadened spectrum by observing the burned hole. A very sharp (0.003 nm) dye laser was used to excite resonantly the Z_3 excitons in particular-size CuCl microcrystals. As a result of the size-selective excitation, CuCl quantum dots whose quantized energy of the Z_3 excitons is just equal to the laser energy are excited. Then we can observe a dip, that is, the burned hole in the inhomogeneously broadened Z_3 exciton absorption spectrum. We obtained the size dependence of the homogeneous linewidth Γ_h from the hole burning experiment for the first time. The homogeneous linewidth is an important parameter of excitons because it gives the phase relaxation rate of excitons in CuCl microcrystals. Nevertheless, the previous studies of the homogeneous linewidth are not free from ambiguities.[4,8]

Two samples of CuCl microcrystals embedded in NaCl host crystals (Nos. 1 and 2) were used in this study. Absorption peaks of the Z_3 exciton in the No. 1 and No. 2 samples are 3.223 eV and 3.230 eV at 77 K, respectively. These samples were made from a mixture of NaCl powder and CuCl powder. They were grown by the transverse Bridgman method. After preparing crystals from the melt, samples were annealed in order to control the size distribution of CuCl microcrystals. The molar fraction of CuCl was determined by the inductively coupled plasma optical emission spectroscopy. The volume molar fraction of CuCl is 0.16% for two samples. This low concentration of CuCl is essential to reduce the energy transfer between dots and to give the credible homogeneous linewidth, as shown in the following procedures. These samples have been mainly characterized by absorption spectra at 77 K. The Z_3 exciton lines of both the samples lie at an energetically higher spectral position compared with that of bulk crystals. This energy shift is due to the quantum size effect and expressed by $\hbar^2\pi^2/[2M(a + 0.5a_B)^2]$,[9] where M is the translational mass of exciton, a is the radius of a microcrystal, and a_B is the Bohr radius of the Z_3 exciton. From the spectral position of the peak of Z_3 absorption, we estimated their mean radii. The mean radii of Nos. 1 and 2 are 6.1 and 4.1 nm, respectively. We also observed the broadening of the Z_3 absorption line, compared with bulk CuCl. This is explained by the inhomogeneous broadening due to the size distribution of the microcrystals.

The experiments were performed in a pump-and-probe configuration. An LD390 dye laser, whose wavelength was tunable from 380 to 390 nm, was used as a pump source. This laser was pumped by the excimer laser. The spectral linewidth of 0.003 nm was achieved in this dye laser system. The laser pulse duration was about 10 ns. As a probe source, we used the amplified spontaneous emission from a dye cell filled with BBQ dye solution. The excimer laser pulse also pumped the dye cell through a cylindrical lens. The probe pulse covered the broad spectrum ranging from 380 to 390 nm. The pulse duration was about 10 ns. The probe pulse through an optical delay impinged on the sample at the same time as the pump pulse hit the sample. There was no time delay between pump and probe pulses. In order to attenuate the probe pulse in front of the sample, we inserted a few neutral density filters. The probe beam was focused on the sample into a spot which lied inside a spot of the pump beam. The diameter of the pumped spot was several hundred micrometers. A polarizer was placed in front of the sample across the pump beam and another one behind the sample across the probe beam. Polariza-

 0003-6951/91/391758-03$02.00

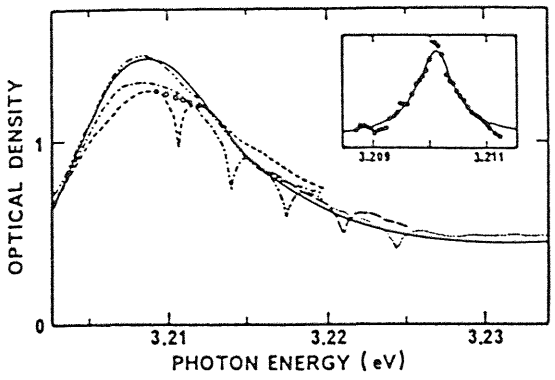

FIG. 1. The absorption spectra of sample 2 obtained by the pump-and-probe experiment at 2 K. Burned holes (A)–(E) correspond to the pump photon energies of 3.2101, 3.2134, 3.2168, 3.2201 and 3.2235 eV, respectively. The excitation density is 146 kW/cm^2. The solid line shows the absorption spectrum without pump. Open circles show the base curve to extract the burned hole (A). The inset shows the fitting of the burned hole (A) by a Lorentzian. Solid circles show the hole. The fitting is shown by a solid line.

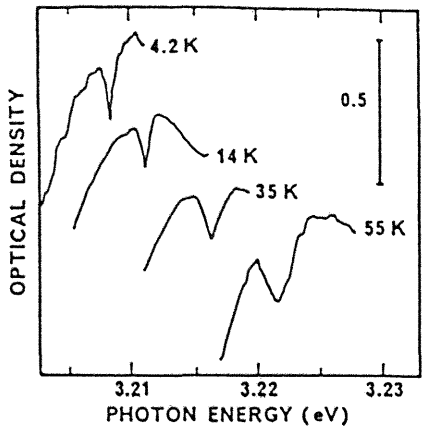

FIG. 2. The absorption spectra of sample 2 taken by the pump-and-probe experiment at various temperatures (from 4.2 to 65 K). The absorption peak is selectively excited in all cases. The excitation density is 490 kW/cm^2.

tions of two polarizers were crossed to each other so that most of the scattering of the pump beam was eliminated. The sample was directly immersed in superfluid helium (2 K) in a double Pyrex cryostat. The probe beam through the sample was analyzed by a double spectrometer and detected by a photomultiplier. The spectral resolution of our experiments was 0.01 nm. It was determined by the resolution of the spectrometer. The signal was amplified 10 times and averaged by means of a wide-band preamplifier and a Boxcar integrator.

Figure 1 shows the absorption spectra of sample 2 under the pump, obtained by the pump-and-probe experiment at 2 K. The photon energy of the pump pulse E_p was varied as 3.2101, 3.2134, 3.2168, 3.2201, or 3.2235 eV. The excitation density was 146 kW/cm^2. We observed the hole-burning around E_p.

The size of a microcrystal determines its quantized Z_3 exciton energy. Accordingly, we can selectively excite particular-size microcrystals by tuning E_p to their energy in the inhomogeneously broadened Z_3 absorption spectrum. Thus, each hole in Fig. 1 is burned out by the size-selective excitation. The pump energies in Fig. 1 correspond to the radii of 4.1, 3.7, 3.3, 3.1, and 2.9 nm, respectively. We also observed the hole-burning around E_p in sample 1 under the pump.

The line shape of the burned hole is well fitted by a Lorentzian as shown in the inset of Fig. 1. Therefore we need not take account of the effect of the energy transfer, in contrast with the previous fluorescence line narrowing measurement of a sample doped with 1% CuCl.[4] This means that the CuCl concentration of 0.16% is low enough to reduce the energy transfer. In this case, the full width at half maximum (FWHM) of the burned hole 2Γ is equal to twice of the homogeneous linewidth Γ_h under the sufficiently weak excitation. Therefore, we should check the power broadening effect. We could not observe the power broadening in the power density range between 28 kW/cm^2 and 540 kW/cm^2. Therefore, FWHM of each burned hole means twice of the homogeneous linewidth Γ_h.

We also measured the temperature dependence of $2\Gamma_h$. Figure 2 shows the absorption spectra of sample 2 taken by the pump-and-probe experiment at various temperatures. The Z_3 exciton absorption band shifts to the higher energy side with the increase in the temperature. Therefore, we tuned the pump photon energy E_p to the absorption peak and tracked the photon energy of certain-size microcrystals. In this experiment, the microcrystals of 4.1 nm in radius was excited at various temperatures under the excitation density of 490 kW/cm^2.

A broadening of the hole was observed with the increase in the temperature. Figure 3 shows the temperature dependence of the FWHM of burned holes $2\Gamma_h$. The broadening is caused by the exciton-phonon interaction. The phonon broadening of $2\Gamma_h$ is phenomenologically fitted by the form,

$$2\Gamma_h(T) = 2\Gamma_0 + CT^2.$$

The homogeneous linewidth at 0 K is $2\Gamma_0 = 0.59$ meV and

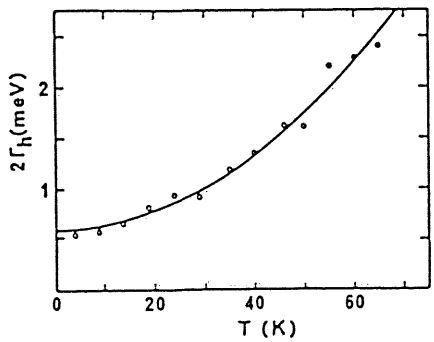

FIG. 3. The homogeneous linewidth of the Z_3 exciton absorption line in the microcrystal, whose radius is 4.1 nm, is plotted as a function of temperature. The solid line shows the result of fitting: $0.59 + 4.6\times10^{-4}\times T\,(\mathrm{K})^2$ (meV).

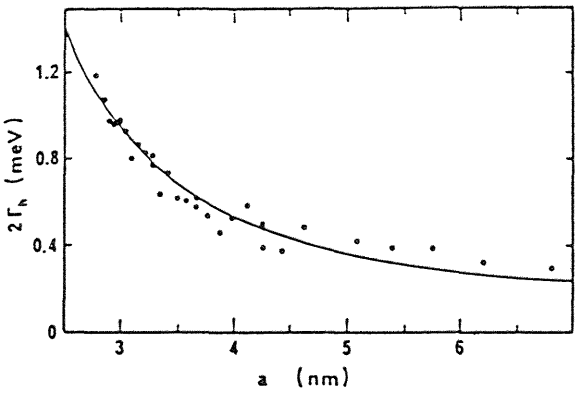

FIG. 4. The homogeneous linewidth of the Z_3 exciton absorption line plotted as a function of the size of the CuCl microcrystal. The solid line shows the result of the fitting; $6.8\times a(\mathrm{nm})^{-2}+0.14$ (meV).

a parameter C is 4.6×10^{-4} meV/K^2. The fitting is shown in Fig. 3 by the solid line.

We have already reported the broadening due to the exciton-optical phonon interaction.[8] It is less than 0.03 meV below 70 K. Therefore, in this temperature range, the exciton-optical phonon interaction is negligible. Below 70-K exciton-acoustic phonon interaction is the dominant phonon broadening in the CuCl microcrystals. However, Fig. 3 shows that the temperature-dependent part of the broadening, phonon broadening, is at most smaller than $2\Gamma_0$ by an order of magnitude at 2 K. Therefore, the homogeneous broadening at 2 K should be explained by the exciton dephasing mechanism other than the exciton-phonon interaction.

Figure 4 shows $2\Gamma_h$ observed at 2 K as a function of the radius of microcrystals. The homogeneous linewidth Γ_h increases with the decrease in the microcrystal radius a. The relation between Γ_h and a is well expressed by the form

$$2\Gamma_h(a)=A\times a^B+2\Gamma_{\mathrm{bulk}},$$

where $2\Gamma_{\mathrm{bulk}}=0.14$ meV is the Z_3 exciton linewidth of bulk CuCl obtained by the two-photon absorption measurement below 10 K.[10] The best fitting was obtained with parameters $A=6.8$ meV nm^2 and $B=-2$ as shown in Fig. 4 by the solid line.

Here, we propose a simple model which explains this result, especially a^{-2} dependence. Theoretical study proved that the exciton quantization is a good picture when a is more than 4 times larger than the exciton Bohr radius a_B($=0.68$ nm).[11] Our study is just limited in this region where a is larger than 2.7 nm. Excitons are going and returning in a microcrystal and the exciton quantization takes place as a result of the interference between the going and returning exciton waves. In our model, the phase relaxation of Z_3 excitons takes place through the collisions at the irregular surface of microcrystals. The time in which the generated exciton moves and collides with the irregular surface of CuCl microcrystals determines the phase relaxation time T_2. In this classical model, the velocity of an exciton v in the lowest quantized state in a sphere whose radius is a is given by

$$v=\pi\hbar/Ma,$$

where M is the Z_3-exciton translational mass of $2.3m_0$ (m_0: electron mass). The phase relaxation time T_2 is given by,

$$T_2=2a/pv=2Ma^2/\pi\hbar p,$$

where p is the dephasing probability of excitons at the surface. Therefore, the size dependence of the homogeneous linewidth is calculated as,

$$\hbar/T_2=\pi\hbar^2p/2Ma^2=52p\times a(\mathrm{nm})^{-2}\ (\mathrm{meV}).$$

Thus, a^{-2} dependence of Γ_h is simply explained on this model. The calculated size dependence of the homogeneous linewidth agrees with that obtained by the experiments, if p is taken as 0.07. This means that an exciton in a CuCl microcrystal dephases at the surface irregularity during several periods of going and returning motion.

In summary, we obtained the size dependence of the homogeneous linewidth of Z_3 exciton absorption structures in CuCl microcrystals for the first time by the pump-and-probe experiment at 2 K. The size-dependent part of the homogeneous linewidth is inversely proportional to the square of the radius of the microcrystal. The size dependence is explained by a simple model that the phase relaxation of excitons takes place through the scattering at the irregular surface of the microcrystal.

The authors express their deep thanks to Dr. K. Era at National Institute for Research in Inorganic Materials for his encouragement and kind experimental facilities. This work is partially supported by the Nippon Sheet Glass Foundation for Materials Science.

[1] A. I. Ekimov, Al. L. Efros, and A. A. Onushchenko, Solid State Commun. 56, 921 (1985).
[2] E. Hanamura, Phys. Rev. B 37, 1273 (1988).
[3] P. Gilliot, J. C. Merle, R. Levy, M. Robino, and B. Hönerlage, Phys. Status Solidi B 153, 403 (1989).
[4] T. Itoh and M. Furumiya, J. Lumin. 48 & 49, 704 (1991).
[5] A. P. Alivisatos, A. L. Harris, N. J. Levinos, M. L. Steigerwald, and L. E. Brus, J. Chem. Phys. 89, 4001 (1988).
[6] N. Peyghambarian, B. Fluegel, D. Hulin, A. Migus, M. Joffre, A. Antonetti, S. W. Koch, and M. Lindberg, IEEE J Quantum Electron. QE-25, 2516 (1989).
[7] M. G. Bawendi, W. L. Wilson, L. Rothberg, P. J. Carroll, T. M. Jedju, M. L. Steigerwald, and L. E. Brus, Phys. Rev. Lett. 65, 1623 (1990).
[8] Y. Masumoto, T. Wamura, and A. Iwaki, Appl. Phys. Lett. 55, 2535 (1989).
[9] T. Itoh, Y. Iwabuchi, and M. Kataoka, Phys. Status Solid B 145, 567 (1988).
[10] M. Kalm and Ch. Uihlein, Phys. Status Solidi B 87, 575 (1978).
[11] Y. Kayanuma, Solid State Commun. 59, 405 (1986).

Biexciton lasing in CuCl quantum dots

Yasuaki Masumoto and Tomohiro Kawamura
Institute of Physics, University of Tsukuba, Tsukuba, Ibaraki 305, Japan

Koh Era
National Institute for Research in Inorganic Materials, Tsukuba, Ibaraki 305, Japan

(Received 29 June 1992; accepted for publication 4 November 1992)

Lasing of CuCl microcrystals embedded in a NaCl single crystal was observed for the first time. The lasing takes place at 77 K in a sample sandwiched between dielectric mirrors under pulsed ultraviolet laser excitation. The lasing transition is that from biexciton to exciton. The lasing is observed up to 108 K. The optical gain of the sample is almost the same as that of a CuCl bulk crystal in spite of the low concentration of CuCl in the NaCl matrix.

Semiconductor low-dimensional quantum structures are expected to be promising semiconductor laser devices.[1-3] As the dimension is lowered, the modified density of states concentrate carriers more in a certain energy range. This concentration is expected to give the system more gain for lasing. Zero-dimensional quantum confinement of carriers turns the density of states into a set of quantum levels. This is most favorable for the semiconductor laser because the gain energy region is ultimately concentrated. Therefore, the quantum dot laser should be realized and its characteristics should be clarified.

CuCl microcrystals are a prototypical system to be studied in the sense that the exciton quantum confinement takes place more strongly than the electron and hole individual quantum confinement.[4] Hence, they are called quantum dots. The large binding energy of the biexciton in a CuCl crystal, 32 meV, makes the biexciton stable and allows us to observe biexciton absorption and luminescence.[5] Biexciton luminescence is observed in CuCl quantum dots, also.[6,7] In the quantum dots, exciton and biexciton translational motions are quantized and a continuous density of states becomes a set of discrete quantum levels. In photopumped bulk CuCl crystals, the optical gain due to the transition from the biexciton to the longitudinal Z_3 exciton is high[8,9] and lasing takes place at this transition.[10] In this letter, we report the first observation of lasing in CuCl quantum dots. We found that the biexciton is lasing in CuCl quantum dots. The optical gain of the CuCl quantum dots is examined and is compared with that of a CuCl bulk crystal.

The samples used in this study were CuCl microcrystals embedded in NaCl crystals. The mean size of the microcrystals were determined by small angle x-ray scattering measurements. It was determined to be 5.0 nm based on the Guinier plot of the scattering data. The molar fraction was determined to be 0.3 mol % by the inductively coupled plasma emission spectroscopy. Three pieces of samples were made by the cleavage of a grown and heat-treated crystal. The thinnest piece, 0.12 mm thick, was used for the optical absorption measurement. The second piece was used for the study of luminescence. The third piece was a rectangular parallelepiped and its size was $3.2\times5.6\times0.58$ mm^3. The laser device was the third piece placed in a cavity composed of two parallel dielectric mirrors whose reflectivity was 90%. The shortest side, 0.58 mm long, was placed perpendicular to the mirror face. The cavity length was 0.62 mm.

The excitation source was a nitrogen laser (337 nm) or a XeF excimer laser (351 nm). The experimental setup was composed of the lasers, a monochromator, and an optical multichannel analyzer. The ultraviolet lasers were used to excite the sample placed in liquid nitrogen or in a temperature-variable cryostat. The pulse width of the nitrogen laser was 10 ns, while that of the excimer laser was 20 ns. The optical multichannel analyzer was used to detect the time-integrated spectra. Excitation intensity was changed by using a calibrated set of neutral density filters. We observed lasing in both longitudinal and transverse pumping geometries.

The optical gain measurement was done by observing the intensity of the stimulated emission as a function of the excitation length.[8] A cylindrical lens was used to focus the output of the excimer laser on a line. The length of the line was cut by a slit and was refocused on the sample surface by using another lens. In this way, the excitation length was varied by the slit. The stimulated emission propagating along the sample surface was observed from the extension of the excited line. The minimum excitation length was measured to be 60 μm which gives the spatial resolution of the experiment. We measured the optical gain of two samples by this method. One sample was the same sample, CuCl microcyrstals in a NaCl crystal (QD sample), that was used in the lasing experiment and another sample was a CuCl bulk crystal (B sample) whose size was $6.5\times5.9\times3.1$ mm^3.

The absorption and luminescence spectra of the sample, CuCl microcrystals in a NaCl crystal at 77 K, are shown in Fig. 1. The Z_3 exciton spectra show a blue shift of 6 meV compared with those of bulk CuCl. The blue shift is ascribed to the quantum confinement of excitons.[4,11] The shift and the mean radius of the CuCl microcrystals deduced from the small angle x-ray scattering experiment are consistent with the relation between the blue shift of the Z_3 exciton energy and the mean size of the CuCl microcrystals which was given by the previous measurements.[11] The luminescence spectra were measured under the excitation of the nitrogen laser. With the increase in the excitation intensity, a lower energy band appears around 391 nm and grows. The lower energy band overwhelms the exciton band around the excitation density of 3 MW/cm^2. The

 0003-6951/93/030225-03$06.00

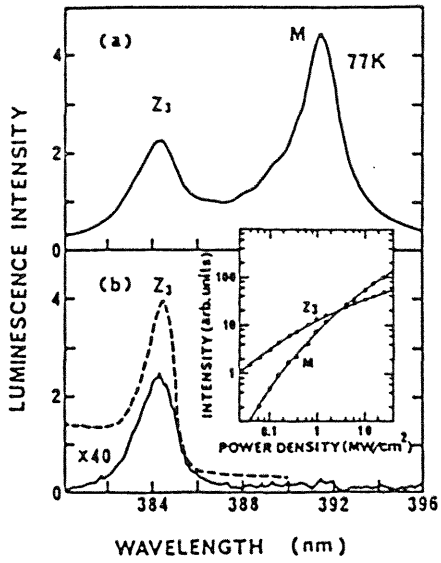

FIG. 1. The luminescence spectra of CuCl microcrystals embedded in a NaCl crystal at 77 K under the nitrogen laser excitation of (a) 24 MW/cm^2 and (b) 39 kW/cm^2. With the increase of the excitation density, the M band appears and grows. Absorption spectrum of the sample at 77 K is shown by the dashed line. In the inset, the excitation density dependence of the Z_3 exciton luminescence and that of the M biexciton luminescence are shown. The excitation density dependence of the Z_3 exciton luminescence is fitted by the expression, $\log_{10} I_{ex}=0.0144(\log_{10} I)^3 -0.0872(\log_{10} I)^2+0.504\ (\log_{10} I)+1.11$, while that of the M biexciton luminescence is expressed by the expression, $\log_{10} I_{bx}=2\log_{10} I_{ex}-1.339$, where I_{ex} is the Z_3 exciton luminescence intensity, I_{bx} the M biexciton luminescence intensity, and I is the excitation density in a unit of MW/cm^2.

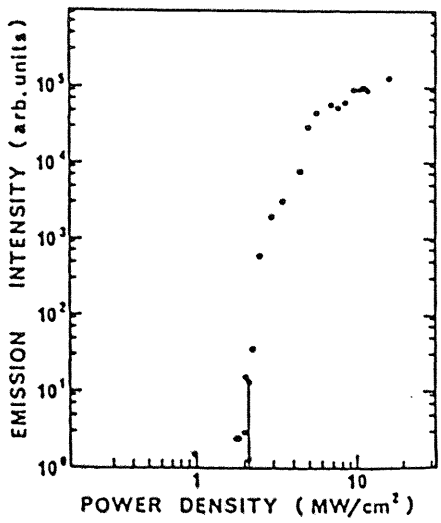

FIG. 2. The log-log plot of the emission intensity of the laser device as a function of the excitation power density for the transverse pumping configuration at 77 K. The arrow shows the threshold for lasing.

luminescence spectra under the low density excitation and the highest density excitation are also shown in Fig. 1. The 391 nm band is ascribed to the so called M band which corresponds to the biexciton recombination leaving an exciton in a crystal.[5–7] The biexciton as well as exciton spectra are considered to be broadened inhomogeneously due to the size distribution of the microcrystals.[6,7,12] The excitation density dependence of the Z_3 exciton luminescence and the M biexciton luminescence is shown in the inset of Fig. 1. Although their dependence is not simply proportional to the excitation density or the square of it, the luminescence intensity of the M biexciton is proportional to the square of that of the Z_3 exciton. This is reasonable because biexcitons are made of two excitons as a result of the attractive interaction.

When the sample placed in a cavity is excited by a nitrogen laser and when the excitation intensity exceeds a threshold, lasing occurs. Figure 2 shows the emission intensity as a function of the excitation power density. At 77 K, the emission intensity grows critically at the threshold power density of 2.1 MW/cm^2 under the transverse pumping condition. The emission spectrum around the lasing threshold is shown in Fig. 3. The broad M band is observed below the threshold. Above the threshold, on the other hand, emission becomes sharp. The sharp emission spectrum having a maximum peak at 391.4 nm is composed of a few longitudinal modes of the laser cavity which are separated by 0.07 nm from each other. The separation almost agrees with the calculated longitudinal mode interval 0.08 nm. It is obtained by using the refractive index of NaCl, 1.567, the spacing between two mirrors, 0.62 mm, and the thickness of a NaCl crystal, 0.58 mm. The emission is directional and the emission solid angle is about 0.03 sr. The photograph of the lasing device under excitation shows halation when we took it from the lasing direction. This observation clearly indicates that the device shows lasing. Lasing is observed up to 108 K.

The quantum size effect of the biexciton in CuCl was studied by Itoh *et al.*[6] The experimental results show that the biexciton state is quantized and the quantum confined energy of the lowest biexciton state, ΔE_{bex}, is described by $\Delta E_{bex}=(\hbar^2/2M_{bex})(\pi/a)^2$, where $M_{bex}=5.3\ m_0$ is the translational mass of the biexciton,[5] m_0 is the electron mass, and a is the radius of microcrystals. The equation holds when a is larger than 3 nm. Below 3 nm, the biexciton binding energy is considered to increase as a result of the squeezing of biexcitons.[13] The energy separation between the lowest biexciton state and the second lowest

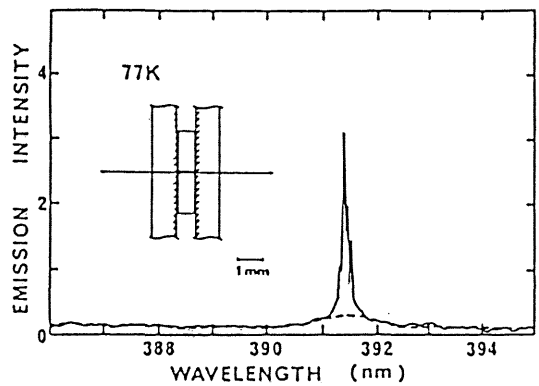

FIG. 3. Emission spectra of the laser device at 77 K below and above the lasing threshold. The threshold I_{th} is about 2.1 MW/cm^2. The solid line shows the spectrum under the excitation of 1.08 I_{th}. The dashed line shows the spectrum under the excitation of 0.86 I_{th}.

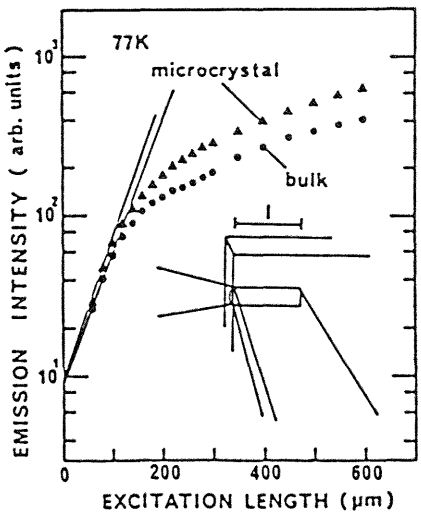

FIG. 4. Stimulated emission intensity of M luminescence as a function of excitation length. The excitation wavelength is 351 nm and its density is 0.8 MW/cm^2. Solid triangles show the data of CuCl microcrystals in an NaCl crystal (QD sample), while solid circles show that of a CuCl bulk crystal (B sample). The small signal optical gains for the QD sample and the B sample are 208 and 192 cm^{-1}, respectively. In the inset, excitation and observation geometries are shown.

biexciton state is equal to $3\Delta E_{bex}=8.5$ meV$=99$ K, when a is equal to 5.0 nm. Thermal energy, 108 K, is almost equal to $3\Delta E_{bex}$. Therefore, we speculate that biexciton lasing takes place when $3\Delta E_{bex}$ is larger than the thermal energy.

In this system, the laser action takes place in three levels, ground, exciton, and biexciton states. Ultraviolet laser light (337 nm) corresponding to the band-to-band transition generates electron hole pairs in CuCl microcrystals. They form excitons and biexcitons quickly. If the excitation density is high enough to generate a biexciton rather than an exciton, the population inversion takes place. The optical gain is formed as a result of this population inversion. The threshold excitation density for lasing and the excitation density where the M luminescence exceeds the Z_3 exciton luminescence almost coincide to each other. This observation is quite reasonable if the population inversion takes place at this excitation density.

It is an interesting test to examine the optical gain of the QD sample in comparison with that of the B sample. We measured the optical gain by using a XeF excimer laser because the output of the laser is intense and has good spatial uniformity. The laser light (351 nm) also corresponds to the band-to-band excitation. We observed a similar luminescence spectra and excitation density dependence, as shown in Fig. 1. However, the excitation density where the M luminescence exceeds the Z_3 exciton luminescence was reduced to 0.7 MW/cm^2. We measured the optical gain under the excitation density of 0.8 MW/cm^2. Although the absorption coefficient of the B sample is much larger than the QD sample,[14] both QD and B samples are thick enough to absorb all of the laser fluence, except the reflection loss. The result of the gain measurement is shown in Fig. 4. Below 120 μm, the emission intensity is proportional to e^{gl}, where g is the small signal optical gain and l is the excitation length. The data show the saturation of the optical gain above 120 μm. The values of g of the two samples are comparable to each other, although the molar fraction of CuCl is 0.3 mol % in the QD sample. The gain value of the B sample, 192 cm^{-1}, under the excitation density of 0.8 MW/cm^2, is consistent with the previous report.[8] The result indicates that the optical gain of the microcrystals per unit volume of active medium for lasing, CuCl, is 300 times larger than that of a bulk crystal.

At present, we cannot explain the reason why the optical gain of CuCl microcrystals is so large. We imagine that the confinement of biexcitons and excitons in CuCl microcrystals makes the large population inversion and that it is probably the origin. Further study is necessary to clarify the reason. Because the homogeneous width of the biexciton recombination transition in CuCl quantum dots is considered to be much narrower than the inhomogeneous broadening, and because the optical gain is inversely proportional to the linewidth of the stimulated emission,[15] we can expect further enhancement of the optical gain with narrowing of the size distribution.

In summary, we observed biexciton lasing in CuCl quantum dots for the first time. Lasing takes place in CuCl microcrystals embedded in a NaCl single crystal sandwiched by 90% reflectivity mirrors under the excitation of a nitrogen laser. The lasing was observed up to 108 K. The optical gain of the sample is almost the same as that of a CuCl bulk crystal in spite of the low concentration of CuCl in the NaCl matrix.

[1] C. Weisbuch and J. Nagle, in *Science and Engineering of One- and Zero-Dimensional Semiconductors* (Plenum, New York, 1990), p. 309.
[2] Y. Arakawa and H. Sakaki, Appl. Phys. Lett. 40, 939 (1982).
[3] M. Asada, Y. Miyamoto, and Y. Suematsu, IEEE J. Quantum Electron. QE-22, 1915 (1986).
[4] A. I. Ekimov, Al. L. Efros, and A. A. Onushchenko, Solid State Commun. 56, 921 (1985).
[5] M. Ueta, H. Kanzaki, M. Kobayashi, Y. Toyozawa, and E. Hanamura, *Excitonic Processes in Solids* (Springer, Berlin, 1986), Chap. 3.
[6] T. Itoh, F. Jin, Y. Iwabuchi, and T. Ikehara, in *Nonlinear Optics of Organics and Semiconductors*, edited by T. Kobayashi (Springer, Berlin, 1989), p. 76.
[7] R. Levy, L. Mager, P. Gilliot, and B. Hönerlage, Phys. Rev. B 44, 11 286 (1991).
[8] K. L. Shaklee, R. F. Leheny, and R. E. Nahory, Phys. Rev. Lett. 26, 888 (1971).
[9] M. Ojima, Y. Oka, T. Kushida, and S. Shionoya, Solid State Commun. 24, 845 (1977).
[10] D. A. Weinberger, N. Peyghambarian, M. C. Rushford, and H. M. Gibbs, 1984 Annual Meeting of Optical Society of America, San Diego, 1984, p. 31.
[11] T. Itoh, Y. Iwabuchi, and M. Kataoka, Phys. Status Solidi B 145, 567 (1988).
[12] T. Wamura, Y. Masumoto, and T. Kawamura, Appl. Phys. Lett. 59, 1758 (1991).
[13] Y. Kayanuma and K. Kuroda, Appl. Phys. A 53, 475 (1991).
[14] The absorption coefficient at 351 nm of the B sample is estimated to be about 6×10^4 cm^{-1} [for reference: Y. Kato, T. Goto, T. Fujii, and M. Ueta, J. Phys. Soc. Jpn. 36, 169 (1974)], and that of the QD sample is 120 cm^{-1}. In both cases, samples are thick enough to absorb all of the laser fluence.
[15] K. Shimoda, *Introduction to Laser Physics* (Springer, Berlin, 1986), Chap. 5.

Visible photoluminescence of Ge microcrystals embedded in SiO_2 glassy matrices

Yoshihito Maeda, Nobuo Tsukamoto, and Yoshiaki Yazawa
Hitachi Research Laboratory, Hitachi, Ltd., Hitachi 319-12, Japan

Yoshihiko Kanemitsu and Yasuaki Masumoto
Institute of Physics, University of Tsukuba, Tsukuba 305, Japan

(Received 16 July 1991; accepted for publication 10 October 1991)

Ge microcrystals embedded in SiO_2 glassy matrices were formed by a radio-frequency magnetron cosputtering technique and then annealed at 800 °C for 30 min. The average radius of the Ge microcrystals in SiO_2 was determined to be about 3 nm by means of Raman spectroscopy and high resolution electron microscope. The annealed sample showed a strong room temperature luminescence with a peak at 2.18 eV. This is consistent with quantum confinement of electrons and holes.

Semiconductor-doped glasses show interesting optical properties as a result of quantum confinement of electron and hole wave functions into the semiconductor microcrystals.[1-3] Recently, visible photoluminescence in Si microcrystal powder[4] and silicon quantum wire array[5] fabricated by electrochemical and chemical dissolution of wafers have been reported. Their visible emission are attributed to three- or two-dimensional quantum size effects.

The quantum size effect due to three-dimensional confinement is obvious when the microcrystal size is less than the exciton effective Bohr radius. Since Ge has smaller electron and hole effective masses and a larger dielectric constant than Si, the effective Bohr radius of the excitons in Ge is larger than that in Si. This implies that the Ge microcrystals show a larger shift of an optical band gap (blue shift) than the Si microcrystals. In fact, Hayashi *et al.*[6] examined the optical absorption spectra of Ge microcrystals embedded in SiO_2 glass films deposited by a radio-frequency (rf)-magnetron cosputtering method and reported the large blue shift to visible wavelength region due to a quantum size effect. However, visible wavelength luminescence has not yet been observed in the Ge microcrystals.

In this letter, we report the first observation of visible photoluminescence of Ge microcrystals embedded in SiO_2 glassy matrices prepared by an rf-magnetron cosputtering method.

The samples were prepared by the rf-magnetron cosputtering method. Some chips of 99.999% purity Ge were set onto a 99.99% purity SiO_2 target of 100 mm in diameter. The cosputtering was performed with an Ar partial pressure of 3 mTorr and rf power of 1.2 kW. The sample was deposited on Si wafers cooled by water, and then annealed in an Ar gas atmosphere at 800 °C for 30 min in order to grow Ge microcrystals in SiO_2 glass matrices. The Ge content of the sample was determined to be 42.7 at. % by an inductively coupled plasma optical emission spectroscopy (ICPS).

Figure 1 shows x-ray photoelectron spectra (XPS) of (a) the as-deposited and (b) annealed samples. The XPS data show that both GeO_2 and Ge exist in SiO_2 in the as-deposited state and that most GeO_2 decomposes into Ge after annealing. We found that in the sputter-deposited sample the formation and growth processes of Ge microcrystals involve the decomposition of GeO_2 into Ge and O_2 and the diffusion process of Ge atoms.[7]

Figure 2 shows Raman spectra for (a) as-deposited and (b) annealed samples obtained using 200 mW of the 514.5 nm Ar ion laser. The as-deposited sample shows a very broad spectrum out to 300 cm^{-1} which is similar to the spectrum of amorphous Ge. The annealed sample showed a sharp Raman peak at 297.5 cm^{-1} with a full width at half-maximum (FWHM) of 6.2 cm^{-1}, indicating the growth of Ge microcrystals with good crystallinity after annealing. Fujii *et al.*[8] reported the relationship between FWHN of Raman peak and average size of the Ge microcrystals. According to their data, the average diameter of our sample is estimated to be about 6 nm.

Figures 3(a) and 3(b) show high-resolution electron microscopic (HREM) images of the as-deposited and annealed samples. In the as-deposited sample, we were able to

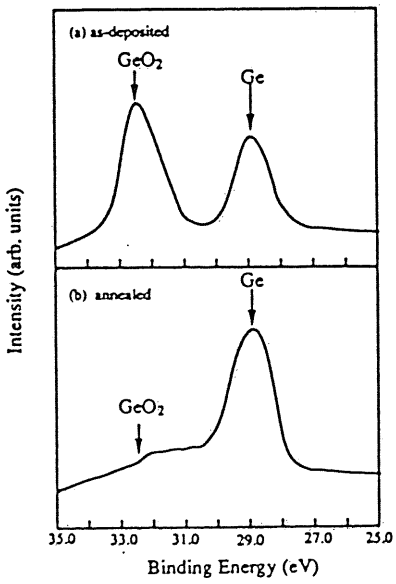

FIG. 1. X-ray photoelectron spectra of (a) as-deposited and (b) annealed samples. We found decomposition of GeO_2 after annealing.

 0003-6951/91/493168-03$02.00

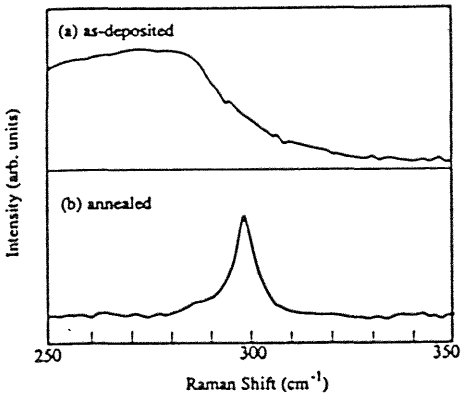

FIG. 2. Raman spectra of (a) as-deposited and (b) annealed samples at room temperature (300 K). The spectra were obtained using a 514.5 nm Ar ion laser, a double monochromator and a photon counter unit through a GaAs(Cs) photomultiplier. We observed Ge microcrystals with good crystallinity.

observe only the glassy structure of SiO_2, while in the annealed sample we found spherical Ge microcrystals. There were less than 6–8 nm in diameter and of good crystallinity. Figure 3(b) shows {111} planes of diamond-structure Ge.

Figure 4 shows photoluminescence spectra excited by 10 mW Ar ion laser at 488 nm at room temperature (300 K). Only in the annealed sample, we observed very broad but pronounced photoluminescence ranging from 500 to 700 nm with the peak at about 570 nm.

We consider three-dimensional quantum confinement of an electron–hole pair in the Ge microcrystal as a possible mechanism for visible photoluminescence. Theoretical calculation of three-dimensional confinement in an infinite spherical potential was treated by Brus.[3] An effective Bohr radius a_B is given by

$$a_B=\kappa\hbar^2/\mu e^2, \tag{1}$$

where κ is a static dielectric constant, $\hbar$ is a reduced Planck constant, μ is reduced mass of an electron–hole pair, and e

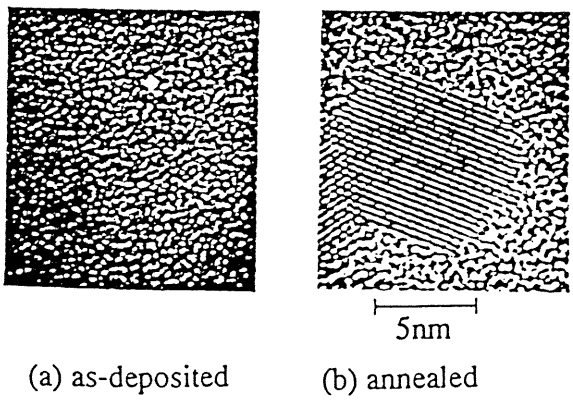

FIG. 3. High resolution electron microscopic images of (a) as-deposited and (b) annealed samples. We observed Ge microcrystals with good crystallinity.

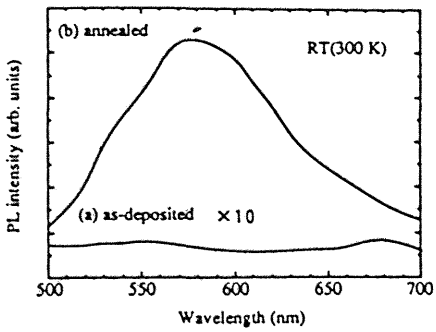

FIG. 4. Room temperature photoluminescence spectra at visible wavelength region of (a) as-deposited and (b) annealed samples. The spectra were obtained using a 488 nm Ar ion laser and a double monochromator.

is electron charge. In the case of Ge bulk, κ is 15.8[9] and μ is reduced mass obtained from $1/\mu = 1/m_e + 1/m_h$. The lightest electron effective mass (m_e) and the lightest hole effective mass (m_h) at L and Γ points are $0.082m_0$ and $0.043m_0$, respectively. We can calculate $\mu = 0.028m_0$ and obtain $a_B = 24.3$ nm. This effective Bohr radius is very large due to the small reduced mass of an electron–hole pair and the large static dielectric constant. In our sample, the average radius of the Ge microcrystal is about 3 nm which is much smaller than the effective Bohr radius of 24.3 nm. Thus electrons and holes can be independently confined into the infinite spherical potential. In this case, the lowest energy of the electron–hole pair E_1 was given by[3]

$$E_1=E_g+(\pi^2\hbar^2/2\mu R^2), \tag{2}$$

where E_g is an optical band gap of bulk crystalline Ge. This Eq. (2) is deduced for the isolated islands of microcrystals (Brus's model). In our case, the Ge microcrystals grow densely in the SiO_2 glassy matrix. The Brus's model is not appropriate to such dense condition. However, we employed the Brus's model in order to analyze our luminescence data.

Using values of $E_g = 0.66$ eV (at 300 K),[10] $R = 3$ nm and $\mu = 0.028\ m_0$, we can obtain $E_1 = 2.15$ eV. Our luminescence peak is located at 2.18 eV, in good agreement with the calculated electron–hole pair energy.[11] The broad spectrum may be associated with the size distribution of Ge microcrystals and complicated band structure of Ge. This result shows that the luminescence can be explained by the Brus's model. This implies that each Ge microcrystal is an isolated island in such dense condition. Furthermore, Rossetti *et al.*[12] suggested that an indirect gap semiconductor material should begin to resemble a direct gap material as the microcrystal size decreases. Visible photoluminescence of Ge microcrystals embedded in SiO_2 glassy matrices can be reasonably explained in this context.

Photoluminescence due to defects[13] in a-SiO_2 could also give rise to the observed spectrum. If such defects are indeed formed in SiO_2 during rf sputter deposition, we should observe luminescence in the as-deposited sample. However, we observed no significant luminescence as

shown in Fig. 4(b). Furthermore, we should pursue the possibility of luminescence due to other defects in a-SiO_2 induced by annealing and decomposition of GeO_2.

In conclusion, we observed visible photoluminescence at room temperature in Ge microcrystals embedded in SiO_2 glassy matrices which were deposited by the rf magnetron cosputtering method. The formation and growth processes of the Ge microcrystals consisted of decomposition of GeO_2 and the diffusion of Ge atoms in SiO_2 glassy matrices. The broad luminescence spectrum with the peak at 570 nm (2.18 eV) was explained by three-dimensional confinement theory (Brus's model).

We would like to acknowledge Dr. Y. Tsunoda, Dr. M. Hanazono, Dr. T. Minemura, and Mr. Y. Sato of Hitachi Research Laboratory for encouragement of this research. We are also indebted to Messrs. M. Wakagi, I. Ikuta, M. Nagai, and Y. Katoh of Hitachi Research Laboratory, and A. Yamamoto and H. Matsue of University of Tsukuba for sample preparation, Raman spectrum measurement, and HREM observation.

[1] A. I. Ekimov and A. A. Onushchenko, Sov. Phys.-Semicond. 16, 775 (1982).

[2] A. I. Ekimov, Al. L. Efros, and A. A. Onushchenko, Solid State Commun. 56, 921 (1985).

[3] L. E. Brus, IEEE J. Quantum Electron. 22, 1909 (1986).

[4] S. Furukawa and T. Miyasato, Jpn. J. Appl. Phys. 27, L2207 (1988); H. Takagi, H. Ogawa, Y. Yamazaki, A. Ishizaki, and T. Nakagiri, Appl. Phys. Lett. 56, 2379 (1990).

[5] L. T. Canham, Appl. Phys. Lett. 57, 1046 (1990).

[6] R. Hayashi, M. Yamamoto, K. Tsunetomo, K. Kohno, Y. Osaka, and H. Nasu, Jpn. J. Appl. Phys. 29, 756 (1990).

[7] I. M. Lifshitz and V. V. Slezov, Sov. Phys. JETP 35, 331 (1959).

[8] M. Fujii, S. Hayashi, and K. Yamamoto, Jpn. J. Appl. Phys. 30, 687 (1991).

[9] C. Kittel, *Introduction to Solid State Physics*, 5th ed. (Wiley, New York, 1976), p. 233.

[10] G. G. Macfarlane, T. P. McLean, J. E. Quarrington, and V. Roberts, Phys. Rev. 108, 1377 (1957).

[11] We can consider several combinations of electrons and holes, for example, electrons at Γ point, heavy and light holes at Γ point, split-off holes and electrons at L point. The observed broad luminescence can be associated with the complicated energy band and various combinations of electrons and holes. However, the blue shift of luminescence is dominated by the electron and hole pair with the lightest reduced mass. Therefore, the outline of our discussion can be considered to be appropriate.

[12] R. Rossetti, R. Hull, J. M. Gibson, and L. E. Brus, J. Chem. Phys. 83, 1406 (1985).

[13] K. Tanimura, C. Itoh, and N. Itoh, J. Phys. C 21, 1869 (1988).

Lifetime of indirect excitons in AgBr quantum dots

Yasuaki Masumoto and Tomohiro Kawamura
Institute of Physics, University of Tsukuba, Tsukuba 305, Japan

Tomoyuki Ohzeki and Shigeji Urabe
Ashigara Research Laboratories, Fuji Photo Film Company, Minami-ashigara, Kanagawa 250-01, Japan
(Received 22 January 1992)

The lifetime of indirect excitons in AgBr quantum dots was studied at low temperature. Indirect-exciton luminescence shows a nonexponential decay. The unique nonexponential decay is well explained by a model that takes into account the discrete number of iodine impurities in a AgBr quantum dot. The obtained radiative lifetime of indirect excitons is 735±50 μs at 2 K and is independent of the radius of microscrystals. The result clearly shows that the L-Γ mixing effect for holes does not work when the radius is larger than 3.5 nm.

I. INTRODUCTION

The optical properties of semiconductor quantum dots have been extensively studied because of their quantum size effect. So far, various phenomena in quantum dots of direct transition semiconductors, such as CdS, CdSe, and CuCl, have been clarified.[1] However, there is no report for quantum dots of indirect transition semiconductors except the previous two experimental reports for AgBr quantum dots.[2,3] AgBr is a well-known indirect-transition semiconductor and basic optical properties including impurity effects have been reviewed.[4,5] This allows us to examine the detailed optical properties of AgBr quantum dots. The preceding work on AgBr quantum dots has found quantum confinement of indirect excitons and isolation of impurities from quantum dots.[3] In this work, we focused our attention on the lifetime of the indirect excitons and found a unique nonexponential decay of indirect excitons. The experimental results are compared with a model which takes into account the discrete number of impurities in AgBr quantum dots.

II. EXPERIMENTAL PROCEDURES

AgBr quantum dots were prepared by the same method that is described in a previous paper.[3] Samples are AgBr microcrystals dispersed in porous gelatin. The mean radius of AgBr microcrystals is determined by the x-ray-diffraction linewidth and the experimentally derived relation between the mean radius and the linewidth, where the radius is measured by electron microscopy.

Samples are directly immersed in superfluid or normal fluid helium below 4.2 K. Above 4.2 K, natural temperature rise is used for the temperature dependence measurement. A photoexcitation source is a nitrogen laser (337.1 nm) or high-pressure mercury lamp. The measurement system is composed of a monochromator, a photomultiplier (Hamamatsu R1477), a boxcar integrator, a lock-in amplifier, and a digital storage oscilloscope (Iwatsu OS-6411; 40 MHz). For the time-resolved measurement, the temporal change of luminescence is taken by the photomultiplier and the digital storage oscilloscope. The temporal resolution is limited by the impedance mismatch between the photomultiplier and the oscilloscope and is experimentally determined to be 3.4 μs.

Excitation density is 160 W/cm^2. At this excitation density, we found that the luminescence exactly coincides with that taken by a high-pressure mercury lamp. We also found the temporal change does not depend on the excitation density between 25 W/cm^2 and 1.6 kW/cm^2.

III. EXPERIMENTAL RESULTS AND DISCUSSIONS

The photoluminescence spectrum of nominally pure AgBr bulk crystals at low temperature is well known.[4-6] It consists of two kinds of luminescence bands near absorption edge. One is phonon-assisted *indirect-exciton* luminescence peaks observed between 2.65 and 2.68 eV. They are classified into two groups, free-exciton peaks and shallow-bound exciton peaks. The second is a strong luminescence band observed at 2.5 eV which is ascribed to the bound exciton at a residual iodine impurity. The 2.5-eV luminescence band is much stronger than the indirect-exciton luminescence observed between 2.65 and 2.68 eV.

In the same manner as AgBr bulk crystals, AgBr microcrystals show two luminescence bands as shown in Fig. 1. The higher-energy band observed at 2.7 eV is ascribed to the indirect-exciton luminescence. The lower-energy band observed at 2.5 eV is ascribed to the bound exciton luminescence at iodine impurities. In contrast to AgBr bulk crystals, the indirect-exciton luminescence is strong compared with the bound exciton luminescence at iodine impurities. The ratio of the indirect-exciton luminescence to the bound exciton luminescence at iodine impurities increases more and more with the decrease in the radius of AgBr microcrystals. Another prominent feature observed in Fig. 1 is the blueshift of the indirect-exciton luminescence. The energy shift of the indirect-exciton luminescence is plotted in Fig. 2. Transverse-optical-phonon-assisted free-exciton luminescence in a bulk AgBr crystal is observed at 2.675 eV.[4-6] The blueshift is explained by the exciton quantization effect. The blueshift is well fitted by Kayanuma's calculation[7] with

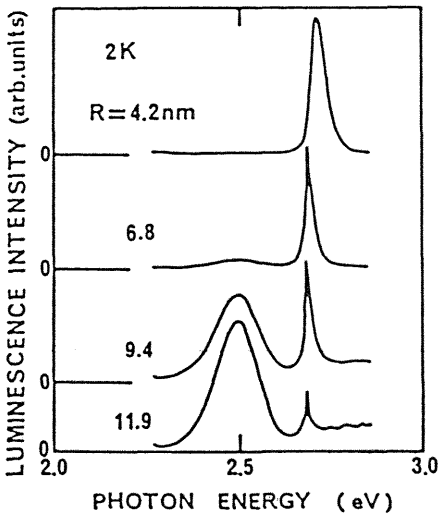

FIG. 1. Photoluminescence spectra of AgBr microcrystals at 2 K. The average radius R of microcrystals is 11.9, 9.4, 6.8, and 4.2 nm. The luminescence spectra are normalized by their respective peak intensities. The 2.7-eV band is indirect-exciton luminescence and the 2.5-eV band is bound exciton luminescence at iodine impurities.

parameters Ry=22 meV,[4] a_B=2.5 nm, $m_e=0.288m_0$, and $m_h=1.02m_0$,[8-10] where Ry is the Rydberg energy of the exciton, a_B the Bohr radius, m_e the electron band mass, m_h the hole band mass, and m_0 the electron mass, respectively. Another prominent feature observed in Fig. 1 are broad luminescence spectra, which are due to the size distribution of microcrystals. Because spectra are broad compared with the energy separation between the free exciton and the shallow-bound exciton, we think the free exciton and the shallow-bound exciton are not distinguishable from each other.

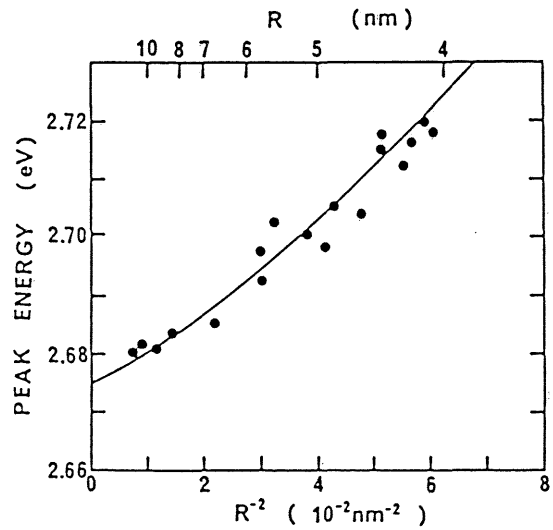

FIG. 2. Peak shift of the indirect-exciton luminescence plotted by solid circles as a function of radius of microcrystals. A solid line shows the fitted result.

Temporal change of indirect-exciton luminescence is shown in Fig. 3. Luminescence intensity is plotted on a semilogarithmic scale. Each curve corresponds to luminescence temporal decay at 2.748, 2.712, 2.700, and 2.689 eV, respectively. These energies correspond to radius of microcrystals of 3.5, 4.5, 5.2, and 6.6 nm, respectively. Luminescence shows nonexponential decays at initial time scale. However, the luminescence decay at the later time scale ranging from 200 μs to 1 ms is well explained by the single exponential decay. We note that the initial decay component increases with the increase in the radius.

We propose the following model to account for the temporal change of the indirect-exciton luminescence. AgBr quantum dots consist of 10^3–10^5 pairs of silver and bromine. The number of iodines in a AgBr quantum dot should be integer and should be 0, 1, 2, 3, or . . . . Usually, ultrahigh-purity AgBr crystals contain iodine impurities whose concentration is on the order of 1 ppm. Therefore a considerable amount of AgBr quantum dots is free from iodine. We assume the Poisson distribution for the number of iodine and other exciton killer impurity distribution for AgBr quantum dots.[3] Therefore the impurity number distribution $p(i)$ is expressed by $p(i)=(\lambda^i/i!)e^{-\lambda}$, where i is the impurity number in AgBr quantum dots, and λ is the expected value of the impurity number. In addition, we simply assume as follows. If a AgBr quantum dot has i impurities, the impurity capture rate of indirect exciton $1/\tau(i)$ is equal to i times of $1/\tau(1)$.[3]

On the basis of the above-mentioned assumptions, the temporal change of the indirect-exciton luminescence $L(t)$ is written by

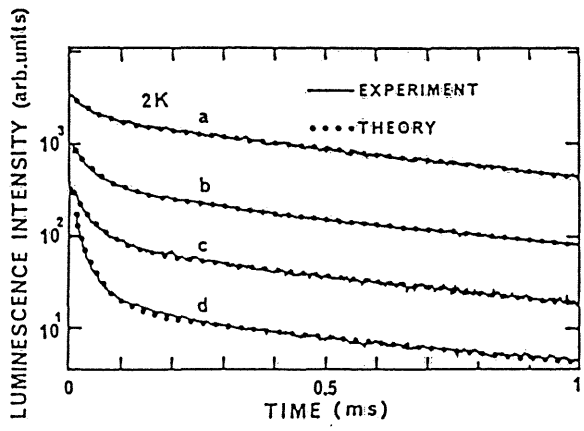

FIG. 3. Temporal change of indirect-exciton luminescence at 2 K. The experimental data a, b, c, and d shown by solid lines are those of microcrystals whose radius is 3.5, 4.5, 5.2, and 6.6 nm, respectively. The calculated results based on Eq. (1) in the text are shown by solid circles. Fitting parameters for curve a are $\tau(0)=719$ μs, $\tau(1)=68$ μs, and $\lambda=0.65$; those for curve b are $\tau(0)=725$ μs, $\tau(1)=54$ μs, and $\lambda=1.15$; those for curve c are $\tau(0)=749$ μs, $\tau(1)=54$ μs, and $\lambda=1.6$; and those for curve d are $\tau(0)=769$ μs, $\tau(1)=46$ μs, and $\lambda=2.7$.

$$L(t)=\sum_{i=0}^{\infty} p(i)e^{-t/\tau(i)}$$

$$=\sum_{i=0}^{\infty}(\lambda^i/i!)e^{-\lambda}e^{-t/\tau(i)}$$

$$=e^{-\lambda}\left[e^{-t/\tau(0)}+\sum_{i=1}^{\infty}(\lambda^i/i!)e^{it/\tau(1)}\right]$$

$$=e^{-\lambda}\{e^{-t/\tau(0)}+e^{\lambda\exp[-t/\tau(1)]}-1\}\ . \qquad (1)$$

In this way, the temporal change of indirect exciton is described by three parameters, $\tau(0)$, $\tau(1)$, and λ. Here, $\tau(0)$ means radiative lifetime of indirect excitons, $\tau(1)$ capture time of indirect exciton by an impurity ion in a AgBr quantum dot, and λ the expected value of the impurity number in a AgBr quantum dot.

The experimental temporal decay of the indirect-exciton luminescence is well expressed by a single exponential decay at the later time stage ranging from 200 μs to 1 ms. Therefore $\tau(0)$ is determined without uncertainty. Fitting the experimental data by Eq. (1), we can derive $\tau(1)$ and λ. The agreement between experimental data and the fitted values is perfect, which suggests the proposed model describes the physical processes of indirect excitons in AgBr quantum dots well. The obtained values of $\tau(0)$, $\tau(1)$, and λ are shown as a function of radius R of microcrystals in Fig. 4. The result clearly shows that $\tau(0)$ and $\tau(1)$ are independent of the radius R, but that λ increases with the increase of R. The value of $\tau(0)$ is about 735±50 μs. The value λ is proportional to $R^{2.1}$. The observation suggests that the impurity number is proportional to the surface area rather than the volume of microcrystals. This implies that the surface defects of microcrystals also work as exciton killer impurities.

So far, lifetime of indirect excitons in bulk AgBr crystals has been studied by several groups. It ranges from 10 ns to 100 ns and depends on impurity concentration, stress, and temperature.[8,11] The lifetime of 735±50 μs we obtained is much longer than values reported previously.

Figure 3 shows that $\tau(0)$ is independent of the radius R of the microcrystals. If the L-Γ mixing takes place in the Brillouin zone as claimed in a previous paper,[3] $\tau(0)$ should decrease with the decrease of the radius. Therefore the experimental data clearly deny the possibility of the L-Γ mixing. Here, we briefly discuss the L-Γ mixing effect in AgBr quantum dots. The wave-vector uncertainty Δk is almost equal to $1/R$, which is deduced from the uncertainty principle. Because the L point and the Γ point are separated from each other by $\sqrt{3}\pi/a$, L-Γ mixing takes place seriously only when Δk reaches $\sqrt{3}\pi/a$, where a is the lattice constant. The radius of the AgBr quantum dots we studied ranges from 3.5 to 13 nm, which is much larger than the lattice constant of $a=0.58$ nm. Therefore the mixing does not work in our case.

The hole mass at the L point m_h is $1.02m_0$.[8-10] The quantum confinement energy of holes at the L point in AgBr quantum dots is $\pi^2\hbar^2/(2m_hR^2)$ which is 30 meV at $R=3.5$ nm. The quantum confinement energy of holes is much smaller than the energy separation between the L point and the Γ point which is equal to 1.7 eV.[4] Therefore resonant L-Γ mixing hardly takes place.[12] Two kinds of the above-mentioned consideration support that the L-Γ mixing for holes does not work in our case.[13]

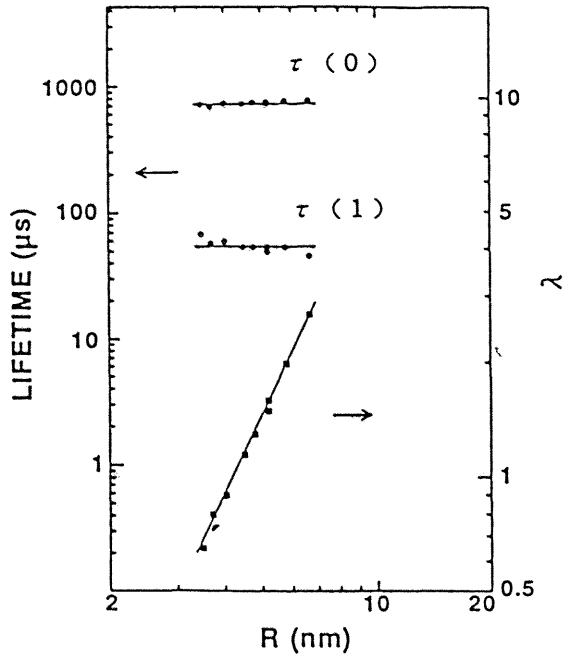

FIG. 4. The obtained parameters $\tau(0)$, $\tau(1)$, and λ as a function of the radius of microcrystals R.

The parameters $\tau(0)$, $\tau(1)$, and λ show weak temperature dependence below 20 K. This weak temperature dependence suggests the coexistence of the free indirect-exciton luminescence and the shallow-bound indirect-exciton luminescence which are observed in nominally pure AgBr bulk crystals. With the decrease of temperature, the shallow-bound indirect exciton becomes more stable. As a result, parameters show weak temperature dependence. With the decrease of temperature, $\tau(0)$ increases gradually. Above 20 K, the indirect-exciton luminescence is quenched, which indicates the increase of the nonradiative decay processes.

IV. CONCLUSIONS

Temporal change of indirect excitons in AgBr quantum dots is studied. Indirect-exciton luminescence shows a unique nonexponential decay which is composed of the initial fast nonexponential decay and the slow exponential decay. The experimental decay curves are well reproduced by a model which takes account of the discrete number of iodine impurities in a AgBr quantum dot. On the model, the slow exponential decay time constant is interpreted as the radiative lifetime of indirect excitons. It is 735±50 μs at 2 K and is independent of the radius of microcrystals. Radius-independent radiative lifetime informs us that the L-Γ mixing effect for holes does not work in our samples.

ACKNOWLEDGMENTS

The authors wish to thank Professor Emeritus H. Kanzaki, Professor Y. Kayanuma, and Dr. T. Takagahara for valuable discussions. They also wish to thank Dr. F. Sakuma at National Research Laboratory of Metrology for the kind loan of a standard lamp. A part of this work is supported by IKETANI Science and Technology Foundation and a Grant for International Joint Research Project from the NEDO, Japan.

[1]A. I. Ekimov, Al. L. Efros, and A. A. Onushchenko, Solid State Commun. 56, 921 (1985).
[2]R. Rossetti, R. Hull, J. M. Gibson, and L. E. Brus, J. Chem. Phys. 83, 1406 (1985).
[3]H. Kanzaki and Y. Tadakuma, Solid State Commun. 80, 33 (1991).
[4]M. Ueta, H. Kanzaki, K. Kobayashi, Y. Toyozawa, and E. Hanamura, *Excitonic Processes in Solids* (Springer, Berlin, 1986), Chap. 6.
[5]H. Kanzaki, Photogr. Sci. Eng. 24, 219 (1980).
[6]H. Kanzaki and S. Sakuragi, J. Phys. Soc. Jpn. 29, 924 (1970).
[7]Y. Kayanuma, Phys. Rev. B 38, 9797 (1988).
[8]T. Baba and T. Masumi, J. Phys. Soc. Jpn. 556, 2549 (1987).
[9]H. Tamura and T. Masumi, Solid State Commun. 12, 1183 (1973).
[10]The hole band mass of $1.02m_0$ is a geometrical average of the longitudinal mass of $1.71m_0$ and the transverse mass of $0.79m_0$.
[11]E. Kawate and T. Masumi, J. Phys. Soc. Jpn. 57, 1814 (1988).
[12]R. A. Faulkner, Phys. Rev. 175, 991 (1968).
[13]Y. Kayanuma (private communication); in his calculation for AgBr, he has shown that the Γ-L mixing takes place when a is smaller than 1 nm.

Quantum size effects and enhancement of the oscillator strength of excitons in chains of silicon atoms

Yoshihiko Kanemitsu, Katsunori Suzuki, Yoshiaki Nakayoshi, and Yasuaki Masumoto
Institute of Physics, University of Tsukuba, Tsukuba, Ibaraki 305, Japan
(Received 28 January 1992)

We have studied the size-dependent optical properties of confined excitons in chainlike Si-backbone polymers with 5–110 Si atoms. The blueshift of the lowest exciton state was observed with decreasing number of Si atoms. In chains having 20 Si atoms or less, the oscillator strength per Si atom for the lowest exciton linearly increases with increasing number of Si atoms. The radiative-decay rate of excitons is in proportion to the square of the number of Si atoms. These results are experimental evidence of the quantum size effect of excitons in chains of Si atoms.

Considerable interest has been focused on the study of low-dimensional semiconductor nanostructures because they exhibit a wealth of quantum phenomena and have a potential as future optoelectronic devices. Recently, many attempts have been made to produce a quasi-direct-gap semiconductor nanostructure made from indirect-gap semiconductors.[1,2] For example, additional photoluminescence lines have been reported in clusters and quantum wires of Si and Ge,[3-5] and clusters and wires of Si and Ge will eventually serve as optoelectronic materials. However, it is difficult to control the number of atoms in clusters and wires, and it is difficult to produce very small clusters and very thin wires. Therefore, optical properties in clusters and wires of Si and Ge are not well understood. In particular, there are few experimental studies of optical properties in small clusters[6] and we have little information on the quantum size effect in small semiconductor clusters. Optical studies of clusters and wires containing a few to several thousand atoms help to understand how molecules evolve into solids.[7]

Natural analogues of clusters and wires are oligomers and/or polymers. Modern organic synthesis and purification techniques allow us to produce materials with controlled molecular weight. These techniques have many advantages over other techniques[3-5] for the production of thin wires. In this paper, we report observation of size-dependent optical properties of confined excitons in chains of Si atoms synthesized by a chemical method.

The chainlike Si-backbone polymers, chains of Si atoms, with molecular structure, EtO-(ϕ-Si-CH_3)$_N$-OEt were synthesized and purified by using the method described in Ref. 8. (Here "ϕ" and "Et" represent, respectively, phenyl and ethyl.) The molecular weight of polymers was checked by using a gel permeation chromatography. The average number of Si atoms in chains, N, was varied as follows: $N=5$, 10, 20, 85, and 110.

The absorption spectra of chainlike Si-backbone polymers solved in tetrahydrofuran (THF) were measured in order to eliminate electronic interactions between chains. The concentration of Si atoms in THF solution was 1.67×10^{-5} mol/dm^3. On the other hand, for photoluminescence spectrum measurements, solid thin films were also prepared on a quartz substrate from THF solution. Photoluminescence spectra were measured by using a 325-nm excitation light from a He-Cd laser or a 313-nm excitation light from a Hg-Xe lamp. The calibration for the spectral sensitivity of the measuring system was performed by using a tungsten standard lamp. Picosecond temporal decay of luminescence under 1-ps and 305-nm laser excitation of ~1 pJ per pulse was measured by using a monochromator of subtractive dispersion and a synchroscan streak camera. The temporal resolution of this system was about 30 ps. We checked that there is no significant difference in the luminescence spectrum and lifetime between solid films and solutions.

Figure 1 shows extinction coefficients per mole of Si atom (ε_{Si}) spectra and normalized photoluminescence spectra of chainlike Si polymers. A sharp absorption peak in a chain of Si atoms of $N=110$ indicates a quasi-one-dimensional electronic system and sharp absorption and emission peaks are due to the lowest one-dimensional (1D) exciton state delocalized in the Si backbone.[9] With a decrease in the number of Si atoms in chains, the absorption peak of the lowest exciton state is shifted to the higher energy (blueshift) and ε_{Si} of the lowest exciton state[10] decreases.

Figure 2 shows the absorption peak of the lowest exciton state and the peak of photoluminescence as a function of the number of Si atoms in chains. The size effect of absorption and photoluminescence spectra are clearly observed in chains having 20 Si atoms or less. It is considered that the blueshift of the absorption peak is explained by a one-dimensional quantum well model. However, simple effective-mass models are not employed to explain the observed blueshift of the absorption spectrum in small semiconductor clusters.[7] The size dependence of the lowest excitation energy E_L of one-dimensional Si-backbone materials is approximately and phenomenologically given by[11]

$$E_L=E_{1D}+[q/(N/2+p)]^2(E_2-E_{1D}),$$

where $p=2/(\pi-2)$ and $q=\pi/(\pi-2)$. E_2 and E_{1D} are the lowest excitation energies of disilane (6.2 eV) and the

quasi-one-dimensional Si-backbone polymer (3.66 eV), respectively. This equation gives interpolated E_L values between disilane ($N=2$) and one-dimensional Si polymer with very large molecular weights ($N \rightarrow \infty$). The calculated curve using the above equation is given by the solid line and roughly agrees with the experimental results. The blueshift of the absorption peak is due to the quantum confinement of the exciton on the Si skeleton.

Figure 3 shows the chain length dependence of the oscillator strength per Si atom for the lowest exciton f_1, calculated from the absorption spectra. The oscillator strength f_1 is directly proportional to the integrated area of the absorption peak in diluted solutions as follows:

$$f_1 = 10^3 \ln(10)(mc/\pi he^2 N_A) \int_{E_1}^{E_2} \varepsilon_{Si} dE ,$$

where m is the mass of electrons, c the velocity of light, e the charge of electrons, h the Planck constant, N_A the Avogadro number. Absorption areas of the lowest exciton, $\int_{E_1}^{E_2} \varepsilon_{Si} dE$ are those surrounded by the solid and dotted lines plotted in Fig. 1, where the high-energy tail of the lowest peak and the low-energy tail of the second peak are estimated by using Gaussian functions and the dotted lines are optimum tails of Gaussian profiles. Thus

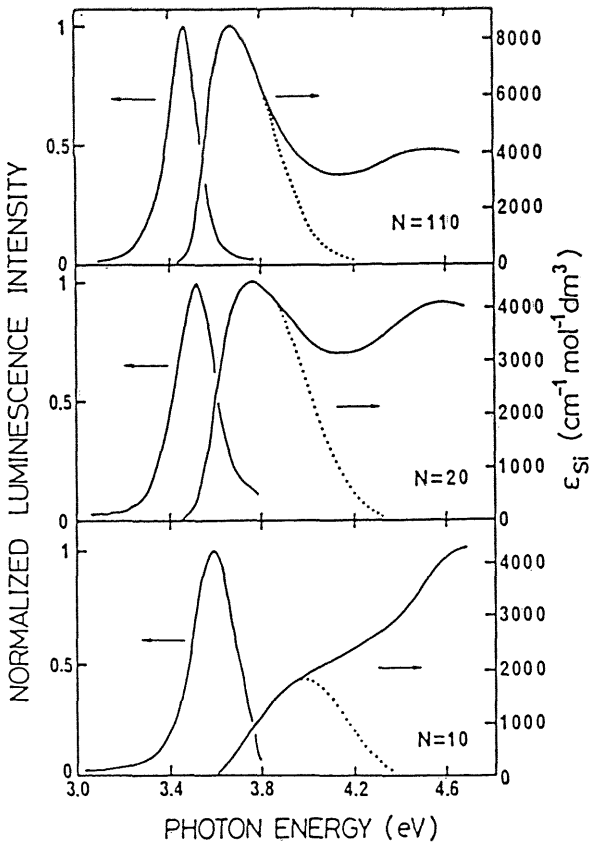

FIG. 1. Extinction coefficients per Si atom (ε_{Si}) spectra and normalized photoluminescence spectra in chainlike Si polymers. N is the average number of Si atoms in chains. Absorption areas of the lowest excitons are those surrounded by solid lines and dotted lines.

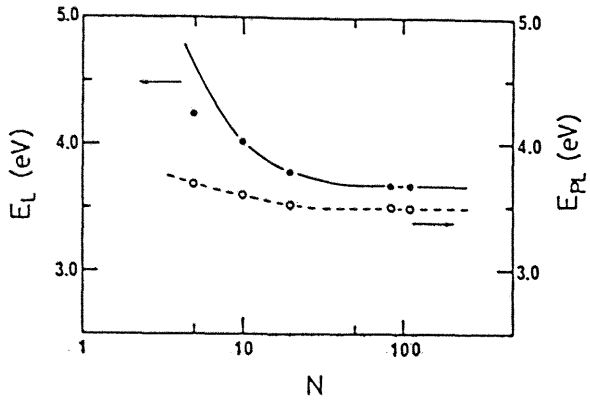

FIG. 2. The absorption peak energy of the lowest exciton state E_L and the peak energy of photoluminescence spectra E_{PL} as a function of the number of Si atoms in chains, N. Solid and open circles correspond to the peak energies of absorption and photoluminescence, respectively. The solid line is calculated by a simple quantum well model discussed in the text. The broken line is a guide to the eye.

we can estimate the oscillator strength of the lowest exciton f_1. The oscillator strength per Si atom, f_1, is linearly proportional to the number of Si atoms and then saturates to a constant value; in Si chains of $N \leq 20$, f_1 is approximately given by $f_1 \propto N$. If chains of Si atoms are solids in nature, the oscillator strength per atom is almost independent of the number of atoms.[12] Therefore, we believe that the size-dependent region is the continuous transition of Si chains from molecular to solid forms and long chains become solidlike in optical properties. To our limited knowledge, there is no theoretical work of the size dependence of the oscillator strength of excitons in small "molecularlike" clusters and chains.

Figure 4 shows picosecond temporal changes in the exciton luminescence at the peak energies. The lumines-

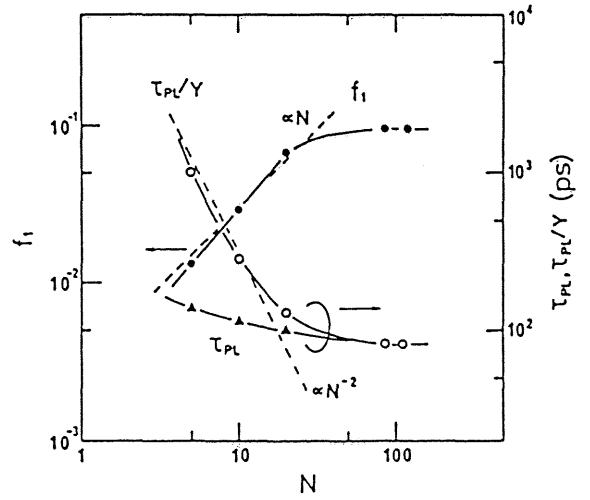

FIG. 3. The oscillator strength of confined excitons f_1, the lifetime of photoluminescence at the peak energy τ_{PL}, and τ_{PL}/Y as a function of Si atoms in chains, N. Y is the relative quantum yield of photoluminescence.

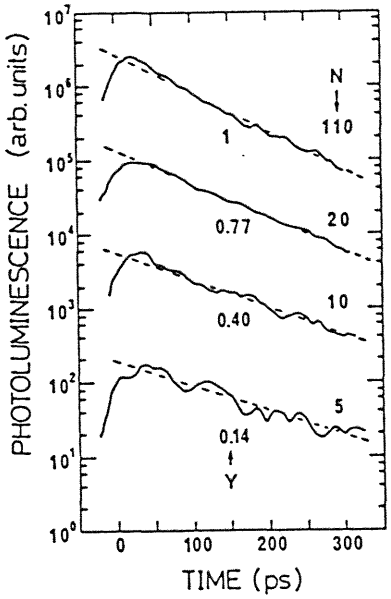

FIG. 4. Picosecond temporal changes in luminescence due to the exciton at peak energies. The luminescence decay is fitted by a single exponential. Y is the relative quantum yield of photoluminescence.

cence decay was approximately described as a single exponential having time constant τ_{PL} and τ_{PL} increases with decreasing N. A single exponential decay of luminescence implies that the luminescence is determined by a simple relaxation process. Here, we assume that the lifetime of luminescence τ_{PL} is determined by two relaxation channels having the radiative decay rate τ_R^{-1} and the nonradiative decay rate τ_{NR}^{-1}. Since the quantum yield of luminescence η is given by $\tau_R^{-1}/(\tau_R^{-1}+\tau_{NR}^{-1})$, the radiative decay rate τ_R^{-1} is given by η/τ_{PL}. Although the absolute values of η in Si polymers were not obtained experimentally, we can use here the relative yield Y for η in order to discuss the size dependence of the radiative decay rate of the exciton and make $Y=1$ for a chain of $N=110$. The values of Y for each Si polymer chain are shown in Fig. 4. The lifetime of photoluminescence τ_{PL} and the radiative decay time τ_{PL}/Y are plotted in Fig. 3. The radiative decay time τ_{PL}/Y increases with the decrease of Si atoms, N. In particular, in chains of $N \leq 20$, τ_{PL}/Y is approximately given by $\tau_{PL}/Y \propto N^{-2}$. The radiative decay time depends on the oscillator strength per chain. If the exciton is a coherent excitation over the Si chain, the radiative decay time is inversely proportional to Nf_1. Since $f_1 \propto N$ in chains of $N \leq 20$, the radiative decay time is in proportion to N^{-2}. The size dependence of radiative decay time τ_{PL}/Y confirms that of the oscillator strength f_1 of the lowest exciton. These size dependences imply that in chains having 20 Si atoms or less, the exciton is coherently excited over the chain of Si atoms.

The above considerations and conclusions are supported by the following discussion. Hochstrasser and coworkers[13] reported that the quantum yield of photoluminescence in a polymethylphenylsilane with very large molecular weight is about 0.1 and the lifetime of luminescence is 73 ps. In our work, the lifetime of photoluminescence is about 76 ps in a Si chain having $N=110$. Using $\eta=0.1$ and $\tau_{PL}=76$ ps, we can estimate the radiative decay rate of excitons delocalized on the Si backbone, τ_R^{-1}. On the other hand, the oscillator strength per Si atom, f_1, directly gives the radiative decay rate based on one Si atom, τ_{abs}^{-1}. The ratio τ_{abs}/τ_R in a Si chain of $N=110$ is about 24, which means that the excitons are delocalized over about 24 Si atoms. Therefore, we conclude that in chains having Si atoms smaller than about 24, the excitons are confined in chains of Si atoms and the size dependence of optical properties of excitons can be observed. In fact, our experiments show that the blueshift of the exciton state energy and the size dependence of the oscillator strength are clearly and experimentally observed in short chains having 20 Si atoms or less. The exciton is coherently excited over about 20 Si atoms on the Si-backbone chain and the exciton has the oscillator strength depending on the number of Si atoms in chains. Our results are experimental evidence of size-dependent optical properties of excitons in chains of Si atoms.[14]

In conclusion, we observed the quantum size effect of the oscillator strength of confined excitons in chainlike Si-backbone polymers. The oscillator strength per Si atom for the lowest excitons is linearly proportional to the number of Si atoms in chains having 20 Si atoms or less and saturates to a value in long chains. This study gives experimental evidence of the continuous transition of a Si chain from molecular to solid form.

The authors would like to thank Professor E. Hanamura for fruitful discussions and Dr. R. Kurata for helpful comments and sample preparations. They also wish to thank Dr. F. Sakuma of National Research Laboratory for Metrology for the kind loan of a standard lamp.

[1]L. Brus, IEEE J. Quantum Electron. QE-22, 1909 (1986).
[2]R. Rossetti, R. Hull, J. M. Gibgon, and L. E. Brus, J. Chem. Phys. 83, 1409 (1985).
[3]S. Furukawa and T. Miyasato, Phys. Rev. B 38, 5726 (1988).
[4]L. T. Canham, Appl. Phys. Lett. 57, 1046 (1990).
[5]Y. Maeda, N. Tsukamoto, Y. Yazawa, Y. Kanemitsu, and Y. Masumoto, Appl. Phys. Lett. 59, 3168 (1991).
[6]For very small clusters of PbI_2, see, Z.-K. Tang, Y. Nozue, and T. Goto, J. Phys. Soc. Jpn. 60, 2090 (1991).
[7]Y. Wang, A. Suna, W. Mahler, and R. Kasowski, J. Chem. Phys. 87, 7315 (1987).
[8]R. D. Miller and J. Michl, Chem. Rev. 89, 1359 (1989); J. P. Wesson and T. C. Williams, J. Polym. Sci. Polym. Chem. Ed. 18, 959 (1989).
[9]L. A. Harrah and J. M. Zeigler, Macromolecules 20, 601 (1987); H. Tachibana, Y. Kawabata, S. Koshihara, and Y. Tokura, Solid State Commun. 75, 5 (1990).
[10]The second peak near 4.6 eV corresponds to the π-π^* transition in the phenyl side chains and the energy and height of the second peak hardly depend on the chain length; K. Take-

da, H. Teramae, and N. Matsumoto, J. Am. Chem. Soc. 108, 8186 (1986).

[11]N. Matsumoto, K. Takeda, H. Terakura, and M. Fujino, in *Silicon-Based Polymer Science*, Advances in Chemistry Series Vol. 224, edited by J. M. Zeigler and F. W. Gordon Fearon (American Chemical Society, Washington, DC, 1990), p. 515.

[12]E. Hanamura, Phys. Rev. B 37, 1273 (1988).

[13]Y. R. Kim, M. Lee, J. R. G. Thorne, R. M. Hochstrasser, and J. M. Zeigler, Chem. Phys. Lett. 145, 75 (1988).

[14]In chainlike Si-backbone polymers (σ-electron conjugated systems), a sharp photoluminescence is observed with essentially no Stokes shift: photoluminescence is due to free-exciton recombination. On the other hand, in π-electron conjugated carbon-backbone polymers, a very large Stokes shift is usually observed: photoluminescence may be caused by the localized exciton recombination. Therefore, in this work, the significant size dependence of optical properties of confined excitons was observed in chains of Si atoms.

On the origin of visible photoluminescence in nanometer-size Ge crystallites

Yoshihiko Kanemitsu, Hiroshi Uto, and Yasuaki Masumoto
Institute of Physics, University of Tsukuba, Tsukuba, Ibaraki 305, Japan

Yoshihito Maeda
Hitachi Research Laboratory, Hitachi Ltd., Hitachi, Ibaraki 319-12, Japan

(Received 13 May 1992; accepted for publication 19 August 1992)

We have studied the origin of visible photoluminescence of Ge nanocrystals in SiO_2 glassy matrix. Spectroscopic analyses of Ge nanocrystals indicate that the room-temperature photoluminescence comes from Ge nanocrystals of diameter of 4 nm or less. High-resolution electron microscopic studies imply that the structure of Ge nanocrystals of diameter <4 nm differs from the diamond structure. These data suggest that new nanostructure crystalline Ge having a character of direct optical transition exhibits the visible photoluminescence.

Optical and electronic properties of semiconductor nanocrystallites, often called quantum dots, have attracted much attention, because they exhibit new quantum phenomena and have potentials for becoming novel and future photonic devices.[1] Most of the previous works have been studied on nanocrystals or quantum dots made from direct-gap semiconductors such as CdS, CdSe, CuCl, etc., experimentally[1] and theoretically.[2] Very recently, optical properties of nanostructures made from indirect-gap semiconductors such Si,[3,4] Ge,[5] etc. have been reported. The discovery of luminescence in nanocrystals of Si and Ge is an extremely important scientific breakthrough with enormous technological implications, since it opens a new possibility for group IV semiconductors as new materials for optoelectronic applications. The origin and mechanism of strong visible luminescence in Si and Ge nanocrystals at room temperature are currently under discussion.[6] In this letter, we present an origin of strong visible photoluminescence of Ge nanocrystals in SiO_2 glassy matrix. Spectroscopic and electron microscopic studies show that a new Ge nanostructure of diameter <4 nm in SiO_2 glassy matrix exhibits the strong room-temperature photoluminescence.

The samples were prepared by a method of rf-magnetron cosputtering of Ge and SiO_2, as previously reported.[5] The Ar pressure and the rf power were 3×10^{-3} Torr and 1.2 kW, respectively. Thin films of the mixture of Ge and SiO_2 were deposited onto Si substrates, and then annealed in an Ar gas atmosphere for 30 min at 300, 600, or 800 °C in order to grow Ge nanocrystals in SiO_2 glassy matrix and to control the size of Ge nanocrystals. The concentration of chemical elements except Ge, Si, and O were less than 0.1 ppm, which were measured by an inductively coupled plasma emission spectroscopy. The crystallinity and size of Ge nanocrystals in SiO_2 matrix were studied by using a high-resolution electron microscopy (HREM).

The photoluminescence (PL) spectra of Ge nanocrystallites were measured by using 454.5–514.5 nm excitation light from an Ar ion laser. The calibration for the spectral sensitivity of the measuring system was performed by using a tungsten standard lamp. The temperature was varied from 10 to 300 K by controlling the flow rate of cold gas of He in a cryostat. Excitation spectra of PL at the peak photon energy were measured by using a Xe lamp and a monochromator. Picosecond PL decay under a 200 ps and 514.5 nm laser excitation was measured using a monochromator of subtractive dispersion and a synchroscan streak camera.

The size distribution of Ge nanocrystals in samples used in this work are shown in Fig. 1. The size distribution of Ge nanocrystals in two samples (solid lines in Nos. 2 and 3) is characterized by a log-normal function given in Ref. 7. In samples (Nos. 2 and 3), the volume-average diameter d_v is calculated using the log-normal function. However, in the sample No. 1, the size distribution of Ge nanocrystals is highly asymmetric and d_v is directly evaluated from the size distribution of Ge nanocrystals in Fig. 1. Sample parameters are summarized in Table I.

Figure 2 shows typical HREM images of Ge nanocrystals in SiO_2 glassy matrix. In Ge nanocrystals larger than 5 nm in diameter, the interplane spacing is 0.326 nm and the surface of the Ge crystals consists of the (111) planes of the diamond structure. However, in Ge nanocrystals of diameter <4 nm, the spacing is 0.298 nm and this spacing cannot be derived from the diamond structure

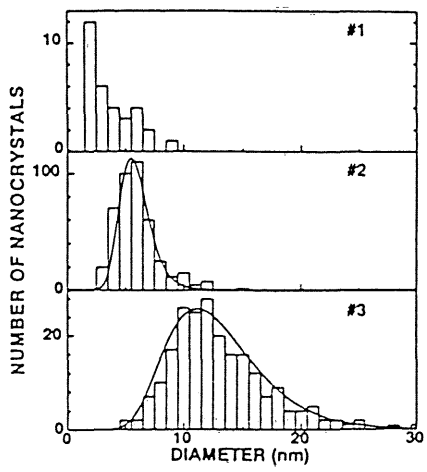

FIG. 1. The size distribution of Ge nanocrystals in SiO_2 matrix. The solid lines are log-normal functions.

 0003-6951/92/432187-03$03.00

TABLE I. Sample parameters including the annealing temperature T_A, the volume-average diameter d_v, the PL peak energy E_p, the volume fraction of Ge nanocrystals with diameter <4 nm V_4, the PL intensity I_{PL}, and the time constant of the PL decay τ.

Sample No.	T_A °C	d_v (nm)	E_p (eV)	V_4[a]	I_{PL}[a]	τ (ns)
1	300	4.2	2.3	100	100	0.85
2	600	6.0	2.2	9.8	7.6	0.90
3	800	14.4	2.3	<0.1	0.8[b]	0.86

[a]Normalized values.
[b]The PL intensity of the sample No. 3 is comparable to that of the as-deposited sample.

of bulk Ge. This fact implies that the structure of nanocrystalline Ge changes critically at the size of about 4 nm. The volume fraction of Ge crystals of diameter <4 nm to total Ge crystals, V_4 are shown in Table I. This volume fraction, V_4, is a very important parameter in the understanding of the origin of the visible photoluminescence from Ge nanocrystals.

Figure 3 shows the PL spectra from Ge nanocrystals at room temperature under 488 nm laser excitation and the excitation spectra of the PL peak. Broad PL spectra exhibiting the peak of 2.2–2.3 eV were observed in all samples. The quantum efficiency as high as about 0.5% was obtained in the sample No. 1 and the relative PL intensity in three samples are summarized in Table I. The peak energy of the PL spectrum scarcely depends on the average diameter of Ge nanocrystals in the sample, d_v. The peak energy of the excitation spectrum near 530 nm also does not depend on the sample and the excitation spectrum differs from the absorption spectrum of bulk Ge of the diamond structure. However, it was found that the PL intensity of the sample is proportional to the volume fraction V_4. Therefore, it is concluded that Ge nanocrystals in the <4 nm size regime exhibit the strong visible photoluminescence.

The PL decay at the peak photon energy was approximately described as a single exponential having a time

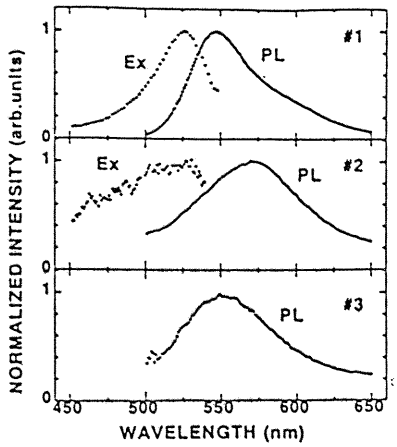

FIG. 3. PL spectra under 488 nm laser excitation and excitation spectra at the peak of the PL spectrum in three different samples.

constant τ and τ is summarized in Table I. The PL lifetime τ does not depend on the photon energy in the broad PL band. No temperature dependence of τ was observed between 10 and 300 K. Since τ is about 40 μs near 4 K in bulk Ge,[8] the PL decay rate is enhanced in Ge nanocrystals. Table I shows that τ does not depend on the average diameter of Ge nanocrystals. The fast PL decay implies that the indirect-gap semiconductor Ge begins to have a character of direct optical transition as size decreases.

Figure 4 shows the temperature dependence of PL intensity and spectrum in the sample No. 1. The PL spectrum does not depend on the temperature, but the PL intensity, I_{PL}, slightly depends on the temperature in all samples. If the radiative transition is excitonic and controls τ and I_{PL}, the temperature dependence of I_{PL} in the ln I_{PL} $-1/T$ plot gives the dissociation energy (or binding en-

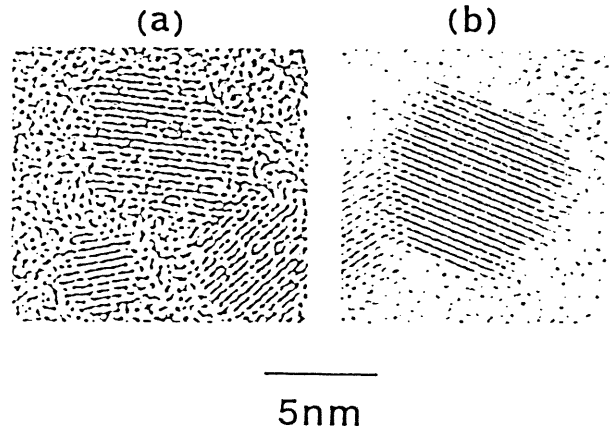

FIG. 2. HREM images of Ge nanocrystals with the diameter of (a) <4 nm and (b) 6.7 nm. The spacing in Ge nanocrystals of diameter <4 nm is 0.298 nm. The spacing of the larger nanocrystals is 0.326 nm.

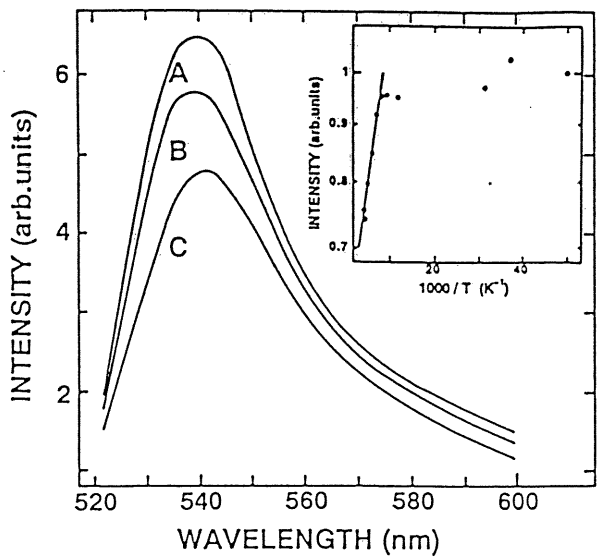

FIG. 4. Temperature dependence of the PL spectrum in the sample No. 1:A;18 K, B;85 K, and C;230 K. The inset shows the temperature dependence of the PL intensity at the peak.

ergy) of excitons in Ge nanocrystals. This energy does not depend on the samples (Nos. 1, 2, and 3) and is about 7 meV. Since the binding energy of excitons is 4.7 meV in the bulk diamond structure Ge,[8] the significant enhancement of the binding energy of excitons due to quantum confinement effects[9] is not observed in Ge nanocrystals. On the other hand, if τ and I_{PL} are controlled by the nonradiative processes, the above experimental results mean that the nonradiative recombination rate scarcely depends on the temperature. Since the nonradiative recombination rate strongly depends on the temperature in bulk Ge, the nonradiative processes in Ge nanocrystals are entirely different from those in bulk Ge. Therefore, we consider that the radiative and nonradiative processes in Ge nanocrystals are very complicated. The insensitivity of the PL intensity and the PL spectrum to temperature suggests that Ge nanocrystals in the <4 nm size regime resemble isolated molecules rather than an indirect-gap semiconductor.[10]

Now we discuss the mechanism of the room-temperature photoluminescence from Ge nanocrystals. An important issue is the role of momentum conservation in optical transitions in the indirect-gap Ge. Bulk crystalline Ge has a conduction-band minimum at the L point and the valence-band maximum at the Γ point in the Brillouin zone. It is expected that the blue shift of the L-Γ indirect transition occurs as size decreases. Takagahara and Takeda[9] calculated the quantum confinement effect on the L-Γ radiative transition using the effective mass approximation and the Luttinger Hamiltonian in Ge quantum dots. They showed that the blue shift of the peak of PL spectrum from infrared to visible region occurs as the diameter decreases: The Ge quantum dots of 14.4, 6.0, and 4.2 nm in diameter show the peaks of 0.9, 1.3, and 2.2 eV in PL spectra, respectively. The radiative lifetime varies from microseconds to nanoseconds. However, the peak energy of the PL spectrum, the PL lifetime, and the activation energy of the PL intensity do not depend on the average diameter of Ge nanocrystals. Therefore, our experimental results do not favor the model of the visible luminescence due to the confinement-induced blue shift of the L-Γ transition in diamond structure Ge.

On the other hand, our HREM studies show that the crystal structure of Ge having 4 nm or less in SiO_2 glassy matrix does not favor the diamond structure, as previously reported.[11,12] Saito[11] pointed out that smaller Ge nanocrystals have a new structure of tetragonal system ($a=0.537$ nm and $c=0.904$ nm). The observed spacing of 0.298 nm as shown in Fig. 2 is nearly equal to 0.292 nm spacing consisting of the (112) plane of the tetragonal unit. However, at the present stage, we cannot identify a new structure of Ge nanocrystals in SiO_2 glassy matrix, because we cannot obtain the electron diffraction pattern of Ge nanocrystals with diameter <4 nm only. We consider that the structure of crystalline Ge changes critically at about 4 nm in diameter and that the origin of the visible photoluminescence is Ge nanocrystals of <4 nm in diameter. In very small nanocrystals, the state mixing occurs for different k states.[10] The transition acquires some allowed character from the k state admixture and k is not a good quantum number. Therefore, we consider that crystalline Ge of diameter <4 nm in SiO_2 glassy matrix has a new nanostructure exhibiting visible luminescence and has the character of direct optical transition due to hybrid electronic properties between the molecular and solid state limits.

In conclusion, we studied the origin and mechanism of visible photoluminescence in Ge nanocrystals in SiO_2 matrix. As the diameter of Ge crystals decreases below about 4 nm, the strong visible photoluminescence is observed and the nanocrystal structure seems to differ from the diamond structure Ge. We consider that visible photoluminescence of Ge nanocrystals in SiO_2 matrix arises from Ge nanocrystals of diameter <4 nm with a new structure and a molecularlike character. The small Ge quantum dot probably has a character of direct optical transition.

The authors would like to thank Dr. T. Takagahara for sending their manuscript prior to publication and for fruitful comments.

[1] See, for example, L. Brus, IEEE J. Quantum Electron. QE-22, 1909 (1986); L. Brus, Appl. Phys. A 53, 465 (1991); and references therein.
[2] See, for example, E. Hanamura, Phys. Rev. B 38, 1288 (1988); Y. Kayanuma, Phys. Rev. B 38, 9772 (1988); and references therein.
[3] S. Furukawa and T. Miyasato, Phys. Rev. B 38, 5726 (1988).
[4] A. G. Cullis and L. T. Canham, Nature 353, 335 (1991).
[5] Y. Maeda, N. Tsukamoto, Y. Yazawa, Y. Kanemitsu, and Y. Masumoto, Appl. Phys. Lett. 59, 3168 (1991).
[6] See, for example, Abstract Book of Fall Meeting of the Materials Research Society, Symposium AA (Boston, Dec. 1991); Symposium on Luminescence from Indirect Semiconductors, the 1992 March Meeting of the American Physical Society, Indianapolis, 1992.
[7] See, for example, K. Tsunetomo, A. Kawabuchi, H. Kitayama, Y. Osaka, and H. Nasu, Jpn. J. Appl. Phys. 29, 2481 (1990).
[8] C. D. Jeffries, Science 189, 955 (1975); and references therein.
[9] T. Takagahara and K. Takeda, Phys. Rev. B (in press).
[10] R. Rossetti, R. Hull, J. M. Gibgon, and L. E. Brus, J. Chem. Phys. 83, 1409 (1985); Y. Wang, A. Suna, W. Mahler, and R. Kasowski, J. Chem. Phys. 87, 7315 (1987).
[11] Y. Saito, J. Cryst. Growth 47, 61 (1979).
[12] S. Hayashi and H. Abe, Jpn. J. Appl. Phys. 23, L824 (1984).

Visible photoluminescence of silicon-based nanostructures: Porous silicon and small silicon-based clusters

Yoshihiko Kanemitsu, Katsunori Suzuki, Hiroshi Uto, and Yasuaki Masumoto
Institute of Physics, University of Tsukuba, Tsukuba, Ibaraki 305, Japan

Takahiro Matsumoto
Electronics Research Laboratories, Nippon Steel Corporation, Sagamihara, Kanagawa 229, Japan

Soichiro Kyushin, Koichi Higuchi, and Hideyuki Matsumoto
Department of Chemistry, Gunma University, Kiryu, Gunma 376, Japan

(Received 10 June 1992; accepted for publication 16 September 1992)

We have studied and compared the optical properties of both porous Si and the chemically synthesized planar and cubic Si skeleton clusters. Broad photoluminescence with large Stokes shifts were observed at the visible region in both samples. Spectroscopic analysis suggests that the surface of porous Si is similar to a condensation of Si clusters. Small Si clusters play a key role in the strong room-temperature photoluminescence in porous Si.

Optical and electronic properties of nanometer-size semiconductor crystallites have attracted much attention, because they exhibit new quantum phenomena and have potential for becoming novel and future photonic devices.[1,2] Very recently, a great deal of research effort is focused on low-dimensional nanostructures made from indirect-gap semiconductors such as Si[3–5] or Ge.[6] Especially, the discovery of the strong luminescence from Si nanostructures fabricated by electrochemical anodization, often called porous Si, is an extremely important scientific breakthrough with enormous technological implications, since it opens up new possibilities for Si as a material for optoelectronic applications.

The origin and mechanism of strong visible luminescence in porous Si are currently under discussion[7] and the possibility of quantum confinement effects in Si wires or dots is suggested by the following observations; (a) the blue shift of the photoluminescence (PL) spectrum of porous Si was observed when the Si column size was reduced by increasing the etching time in HF solutions,[5,8] (b) the temperature dependence of the PL intensity[9] suggests the enhancement of the exciton binding energy, and (c) Raman studies[10,11] show that porous Si maintains the crystalline character of Si and typical crystalline size of about 3 nm.

On the other hand, the importance of the localized states at the surface of nanostructures was pointed out by several authors.[7] With a large surface-to-volume ratio in the highly porous structure, the influence of surface effect on luminescence processes is enhanced and the surface of porous Si is responsible for the origin of luminescence. The studies of luminescence degradation in various ambient gases[12] and x-ray photoelectron spectroscopy[13] suggest that the electronic properties at the surface in porous Si play a key role in the strong luminescence. Moreover, silicon based compounds, especially, siloxene ($Si_6O_3H_6$) derivates are also proposed as an origin of the strong luminescence of porous Si.[14] If the surface of Si crystallites is terminated by hydrogen atoms, siloxene, or other silicon compounds, the electronic properties of the near-surface region are different from the inside of Si crystallites. In this case, it is natural to consider that the surface is formed with a new nanometer-size material.

In this letter, we have studied and compared the optical properties of both porous Si and the chemically synthesized Si skeleton clusters. PL and absorption spectra and picosecond PL decay measurements show that optical properties of porous Si are similar to those of planar and cubic Si skeleton clusters. The rough surface of porous Si is regarded as a condensation of small Si clusters and the clusterlike surface region plays a key role in the strong visible luminescence.

Porous silicon was prepared as follows. The substrates were (100)-oriented 3.5–4.5 Ω cm resistivity *p*-type silicon. Thin Al films were evaporated on the back of the wafers to form a good ohmic contact. The anodization was carried out in HF-ethanol solution ($HF:H_2O:C_2H_5OH=1:1:2$) at a constant current density of 10 mA/cm^2 for 5 min. Furthermore, photochemical etching of the wafer was carried out for 2 min in HF-ethanol solution under illumination with a 500 W tungsten lamp for a distance of 20 cm.[15] After the photochemical etching, the wafers were rinsed in deionized water for 2 min. These etching treatments cause an increase of the PL intensity and a blueshift of the PL peak. Figure 1(a) shows a typical image of a porous Si sample by transmission electron microscope (TEM) analysis. The local structure of the porous silicon is a network of interconnected crystalline silicon islands. The shape of the islands is spherelike rather than wirelike. The size of Si crystallite islands ranges from several nm to 20 nm. Our TEM observations are similar to the report by Cullis and Canham.[8]

A planar Si skeleton cluster (syn-tricyclooctasilane) and cubic Si skeleton cluster (octasilacubane) were synthesized and used as model Si-based materials consisting of a small number of Si atoms. The structures are illustrated in Figs. 1(b) and 1(c). Synthetic and purification methods were described in Ref.16.

The PL spectra of porous Si and Si skeleton clusters were measured in a vacuum by using 325 nm excitation

 0003-6951/92/452446-03$03.00

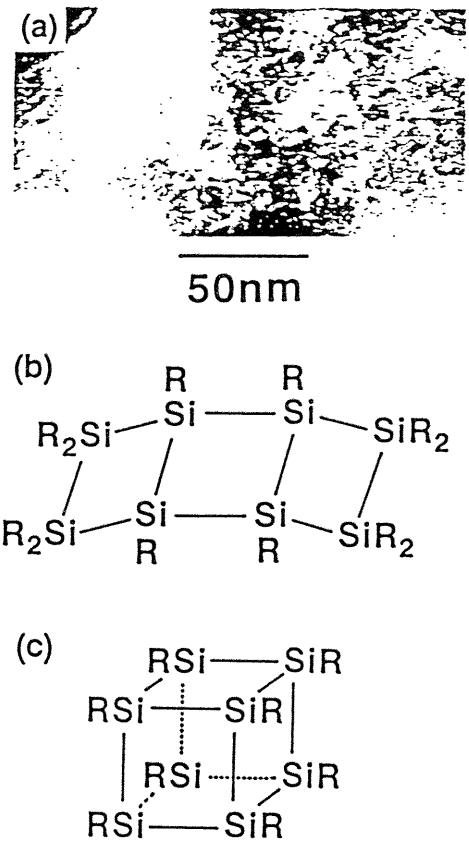

FIG. 1. (a) TEM image of porous Si, (b) a planar Si skeleton cluster, syn-tricyclooctasilane (R=isopropyl), and (c) a cubic Si skeleton cluster, octasilacubane (R=t-butyldimethylsilyl).

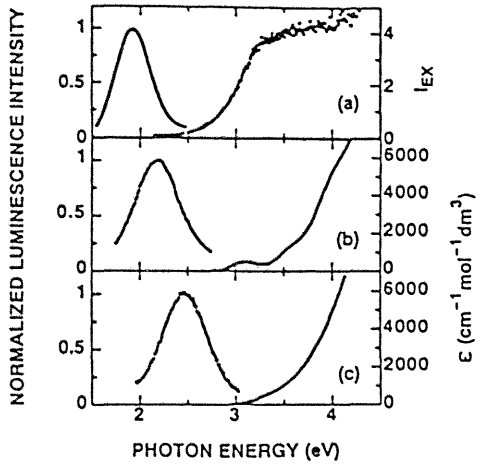

FIG. 2. (a) Excitation (I_{EX}) and PL spectra in porous silicon. Molar extinction coefficients ϵ and PL spectra in a planar Si skeleton cluster (b) and in a cubic Si skeleton cluster (c).

light from a He-Cd laser. Excitation spectra of the PL at the peak photon energy were measured by using a Xe-lamp and a monochromator. Picosecond PL decay under a 1 ps and 300 nm laser excitation was measured using a monochromator of subtractive dispersion and a synchroscan streak camera. The calibration of the spectral sensitivity of the whole measuring system was performed by using a tungsten standard lamp. Spectroscopic data were measured at room temperature.

Figure 2(a) shows the excitation and PL spectra in porous Si. A gradual rise in the excitation spectrum is observed at photon energies above 2 eV. An excitation edge exists near ~3.2 eV, and broad PL spectrum is observed at the peak value of 1.98 eV. There exists a large Stokes shift of ~1 eV between the PL peak and the edge of excitation spectrum. Ren and Dow[17] theoretically calculated the size dependence of the band gap of Si crystallites with hydrogenated surfaces. According to their calculations, the band gap of crystallites of 3 nm diam which is a characteristic size of porous Si[8,10,11] is ~1.5 eV. The observed edge energy of ~3 eV and PL peak of ~2 eV are larger than the theoretical band gap (~1.5 eV) of 3 nm crystallites. These imply that a region containing a small number of Si atoms (e.g., clusterlike surface region in Si crystallites) exhibits the strong luminescence.

Figures 2(b) and 2(c) show the absorption and PL spectra in planar and cubic Si skeleton clusters, respectively. The absorption spectra of Si skeleton clusters solved in tetrahydrofuran (THF) were measured and the molar extinction coefficients are plotted in this figure. In a planar Si cluster, the lowest excitation state is observed at 3.09 eV and a broad PL spectrum is observed with the peak of 2.25 eV, thus, the Stokes shift is 0.84 eV. In a cubic Si cluster, the absorption edge is observed at ~3.2 eV and a broad PL spectrum is also observed with the peak of 2.50 eV. Both the broad PL spectra and the large Stokes shifts in planar and cubic Si clusters are different from those in one-dimensional chainlike Si clusters with a direct gap nature.[18] We note that even in very small Si clusters the shape of the cluster plays an important role in determining optical properties. The effect of dimensionality on electronic structures in small Si skeleton clusters is discussed elsewhere.[19] Although we were not able to obtain the absolute PL quantum efficiencies of both porous Si and Si clusters, we estimated that there is no significant difference of the relative PL quantum efficiency between porous Si and Si clusters. The characteristics of PL and excitation spectra of porous Si are similar to those of Si clusters.

Figure 3 shows the picosecond PL decay at peak energies in porous Si and planar and cubic Si skeleton clusters. The picosecond decay is clearly observed in porous Si. Many researchers[7] reported that the PL decay shows a nonexponential behavior with typical time constants ranging from nanoseconds to milliseconds. This behavior is primarily caused as a consequence of the inhomogeneous size distribution of Si nanostructures as shown in Fig. 1. The PL decay exhibits nonexponential behavior even in picosecond time scale. On the other hand, in planar and cubic clusters fast PL decay is also observed in picosecond timescale. The rate of radiative recombination determined by the intrinsic lifetime of excited states is reflected by the initial fast component of the PL decay in an inhomogeneous system such as porous Si, since the long PL decay components are caused by spatial tunneling, thermally ac-

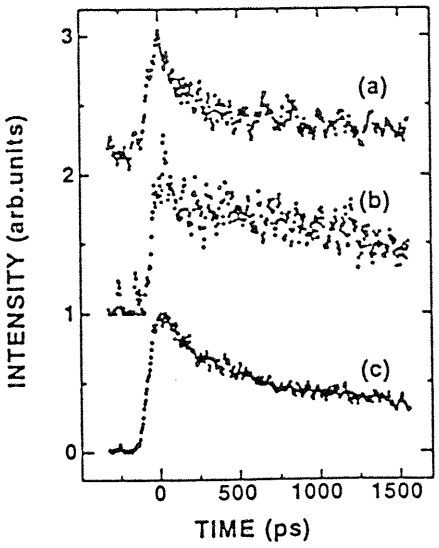

FIG. 3. Picosecond PL decay at the peak photon energies; (a) porous Si, (b) a planar Si skeleton cluster, and (c) a cubic Si skeleton cluster.

tivated carrier diffusion, and so on.[20] Therefore, the essential agreement of the picosecond PL decay between porous Si and Si clusters implies that the luminescent properties of porous Si are similar to those of small planar and cubic clusters.

From our experimental findings of the quantitative agreement of optical properties between porous Si and Si clusters, it is concluded that the substance causing the luminescence in porous Si shows similar optical characteristics to the Si-based clusters. The rough surface of porous Si is considered as a condensation of Si skeleton clusters. The near-surface region consisting of small clusters plays an essential role in determining the strong luminescence properties. Moreover, Brandt *et al.*[14] pointed out that the electronic properties of siloxene compounds with sixfold Si rings are similar to those of porous Si and that small Si skeleton clusters also play an essential role in the luminescence process of these siloxene compounds. The notion of a small Si skeleton cluster gives a better understanding of the luminescent mechanism of porous Si. At present, it is considered that the near-surface region consists of small Si clusters and the clusterlike near-surface region contributes the strong room-temperature luminescence.

In conclusion, we have studied and compared the optical properties of porous silicon and chemically synthesized Si skeleton clusters. Optical properties of planar and cubic Si clusters are similar to those of porous silicon. Spectroscopic analysis suggests that the near-surface region of porous Si consists of small Si clusters and that this origin plays a key role in the strong room-temperature photoluminescence.

The author would like to thank Dr. F. Sakuma of National Research Laboratory of Metrology for the kind loan of a standard lamp.

[1] See, for example, L. Brus, IEEE J. Quantum Electron. QE-22, 1909 (1986); L. Brus, Appl. Phys. A 53, 465 (1991); and references therein.
[2] See, for example, E. Hanamura, Phys. Rev. B 38, 1288 (1988); Y. Kayanuma, Phys. Rev. B 38, 9772 (1988); and references therein.
[3] S. Furukawa and T. Miyasato, Phys. Rev. B 38, 5726 (1988).
[4] V. Lehmann and U. Gosele, Appl. Phys. Lett. 58, 856 (1991).
[5] L. T. Canham, Appl. Phys. Lett. 57, 1046 (1990).
[6] Y. Kanemitsu, H. Uto, Y. Masumoto,and Y. Maeda, Appl. Phys. Lett. 61, 2187 (1992); Y. Maeda, N. Tsukamoto, Y. Yazawa, Y. Kanemitsu, and Y. Masumoto, Appl. Phys. Lett. 59, 3168 (1991).
[7] See, for example, Abstract Book of Fall Meeting of the Materials Research Society, Symposium AA (Materials Research Society, Boston, 1991).
[8] A. G. Cullis and L. T. Canham, Nature 353, 335 (1991).
[9] S. Gardelis, J. S. Rimmer, P. Dawson, B. Hamilton, R. A. Kubiak, T. E. Whall, and E. H. Parker, Appl. Phys. Lett. 59, 2118 (1991).
[10] R. Tsu, H. Shen, and M. Dutta, Appl. Phys. Lett. 60, 112 (1992).
[11] Z. Sui, P. P. Leong, I. P. Herman, G. S. Higashi, and H. Temkin, Appl. Phys. Lett. 60, 2086 (1992).
[12] M. A. Tischler, R. T. Collins, J. H. Stathis, and J. C. Tsang, Appl. Phys. Lett. 60, 639 (1992).
[13] R. P. Vasquez, R. W. Fathauer, T. George, A. Ksendzov, and T. L. Lin, Appl. Phys. Lett. 60, 1004 (1992).
[14] M. S. Brandt, H. D. Fuchs, M. Stutzmann, J. Weber, and M. Cardona, Solid State Commun. 81, 307 (1992).
[15] N. Koshida and H. Koyama, Jpn. J. Appl. Phys. 30, L1221 (1990).
[16] H. Matsumoto, H. Miyamoto, N. Kojima, and Y. Nagai, J. Chem. Soc. Chem. Commun. 1316 (1987); H. Matsumoto, K. Higuchi, Y. Hoshino, H. Koike, Y. Naoi, and Y. Nagai, J. Chem. Soc. Chem. Commun. 1083 (1988).
[17] S. Y. Ren and J. D. Dow, Phys. Rev. B 45, 6492 (1992).
[18] Y. Kanemitsu, K. Suzuki, Y. Nakayoshi, and Y. Masumoto, Phys. Rev. B 46, 3916 (1992).
[19] Y. Kanemitsu, K. Suzuki, Y. Masumoto, K. Sato, S.Kyuushin, and H. Matsumoto (unpublished).
[20] R. A. Street, in *Semiconductors and Semimetals*, edited by J. I. Pankove (Academic, Orlando, 1984), Vol. 21, Part. B, p. 197.

Disorder-induced transition from Gaussian to dispersive carrier transport in molecularly doped polymers

Yoshihiko Kanemitsu, Hiroshi Funada, and Yasuaki Masumoto
Institute of Physics, University of Tsukuba, Tsukuba, Ibaraki 305, Japan

(Received 12 February 1991; accepted for publication 6 May 1991)

Dynamics of hopping charge transport in a polymer matrix doped with two different charge-transport molecules was studied by means of time-of-flight (TOF) photoconductivity measurements. In polymers doped with two molecules of little different ionization potential, the Gaussian (near-rectangular) TOF signal was observed over all compositions and the tail of the Gaussian TOF signal is broadened by a wide distribution of hopping time among molecules due to off-diagonal disorder. On the other hand, in polymers doped with two molecules of different ionization potential, the transition from the Gaussian to the dispersive TOF signal was observed and this is mainly caused by diagonal disorder. It is found that the energetic and spatial distribution of hopping sites play a key role in carrier transport in molecularly doped polymers.

Charge transport in amorphous organic photoconductors has been the subject of much theoretical and experimental interest in recent years.[1–12] A variety of systems has been studied: charge-transfer complex,[3] pure polymers,[4,5] and molecularly doped polymers (MDPs).[6–12] Amorphous organic MDPs become particularly attractive because of their importance as photoconductors in electrophotography and the construction of transport theories in amorphous solid. It is recognized that charge transport in MDPs is a hopping process among doped molecules.

Hopping charge transport depends on both the wave function overlap between hopping sites and the energy difference between hopping sites. In amorphous solids, there exist the fluctuation of hopping site energies (diagonal disorder) and the fluctuation of the wave function overlap between hopping sites (off-diagonal disorder).[2,4,6,9] It is theoretically pointed out that hopping charge transport in MDPs is affected by diagonal and off-diagonal disorder.[9] However, the effects of disorder in MDPs on hopping charge transport are not clarified experimentally.[12] On the other hand, very weak van der Waals interaction between molecules leads to very narrow energy bands, although the width of the energy band is inhomogeneously broadened by the disorder matrix. It is therefore considered that in an inert polymer matrix both diagonal and off-diagonal disorder can be controlled by mixing two charge-transport molecules of different ionization potential and different hopping rate. This advantage of MDPs is not easily used in inorganic amorphous systems. In this letter, we report the experimental observation of effects of the spatial and energetic distribution of hopping sites on hopping transport in MDPs by measuring the time-of-flight photocurrent pulse shape and the drift mobility of holes in an inert polymer doped with two different molecules.

Hole-transporting molecules used in the work were PRA [1-phenyl-3-(*p*-diethylaminostyryl)-5-(*p*-diethylaminophenyl)-2-pyrazoline], HD (1-phenyl-1,2,3,4-tetrahydroquinoline-6-carboxyaldehyde-1,1'-diphenyl hydrazone), OX [2-(*p*-dipropyl-aminophenyl)-4-(*p*-dimethylaminophenyl)-5-(*o*-chlorophenyl)-1,3-oxazole], DEH (*p*-diethylaminobenzaldehyde-1, 1'-diphenyl hydrazone), MPS [4-*N*,*N*-bis(4-methylphenyl)amino-α-phenylstilbene], PS (4-*N*,*N*-diphenylamino-α-phenylstilbene), and OXD [2,5-bis(4'-diethylaminophenyl)-1,3,4-oxadiazole]. The ionization potential, I_p (the threshold energy for the ionization of the solid), was determined by using an ultraviolet photoelectron spectroscopy system (RIKEN, AC-1), and I_p is shown in Table I. The hole-transporting molecules were dispersed in bisphenol-A-polycarbonate. These in methylene chloride were coated onto the aluminum substrate. The dry film thickness was 12 μm. The total concentration of two different molecules in solid polycarbonate film was 50 wt %, and the concentration ratio of one molecule to another molecule was varied between 0 and 100 wt %. The semitransparent gold electrode was finally deposited by vacuum evaporation. In the time-of-flight (TOF) photoconductivity experiment, the sandwich structure sample was connected in a circuit containing a voltage source and a resistance. The MDPs were excited through the gold electrode by a 0.3 ns, 337 nm pulse from a N_2 laser. The current transients were displayed on a digital storage oscilloscope interfaced to a computer. In some experiments, the 0.2 μm charge generation films of metal-free phtalocyanine or amorphous selenium were attached to MPDs films. These two structures were excited by a 0.5 μs, 600 nm pulse from a xenon flash lamp. At high applied field above 1×10^5 V/cm, there was no significant TOF waveform difference between single-layer and two-layer structures. In Gaussian (near-rectangular) pulse shape, the transit time, t_T, is determined by the shoulder in the TOF shape.[11] In dispersive pulse shape, t_T is determined from a double log plot.[11] The hole drift mobility μ is given by $\mu = L^2/t_T V$, where L is the sample thickness and V is the applied voltage.

First, we show TOF results in polymers doped with two molecules of little different ionization potential. Figure 1 summarizes the drift mobility of holes and TOF signal shapes in OXD and PS doped polycarbonate at 2.0×10^5 V/cm and 298 K as a function of the relative weight ratio of OXD to PS. Over all compositions, the Gaussian (near-

 0003-6951/91/310697-03S02.00

TABLE I. The ionization potential and the hole mobility of charge-transporting molecules.

	I_p (eV)	μ ($cm^2/V\,s$)[a]
PRA	5.0	9.1×10^{-7}
HD	5.1	4.2×10^{-6}
OX	5.2	7.5×10^{-7}
DEH	5.3	2.8×10^{-6}
MPS	5.5	6.1×10^{-5}
PS	5.5	3.9×10^{-5}
OXD	5.5	1.7×10^{-7}

[a]Drift mobility of holes in 50 wt % doped polycarbonate measured at 2.0×10^5 V/cm and 298 K.

rectangular) TOF shapes were observed. In the OXD-PS system, the hopping rate among PS molecules is much larger than that among OXD molecules, because the mobility of holes in PS doped polycarbonate is two orders of magnitude more than that in OXD doped polycarbonate as shown in Table I. As the OXD concentration increases, the drift mobility of holes decreases and the wave function overlap among PS-OXD and OXD-OXD molecules increase. Since the hopping rate among OXD-PS pairs is larger than that among OXD-OXD pairs, the hopping among OXD-PS molecules dominates the charge transport in the OXD-PS mixed doped system. The drift mobility in the OXD-PS mixed system is estimated by the simple scaling of the mobilities of OXD and PS molecules.

Moreover, in PS and OXD mixed doped systems, the Gaussian TOF signal becomes "dispersive" with decreasing the hole mobility. The "dispersive" Gaussian TOF signal is characterized by the tail broadening of the Gaussian TOF signal, d, and d is defined as the following relation:

$$d=\Delta t_T/t_T=(t_{1/2}-t_T)/t_T, \tag{1}$$

where $t_{1/2}$ is the time when the photocurrent drops to one-half of the value at t_T. In Fig. 1, d is plotted as a function

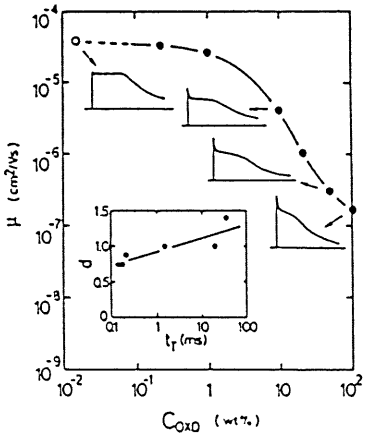

FIG. 1. Hole drift mobility and typical time-of-flight photocurrent pulse shapes in the PS-OXD system at 2.0×10^5 V/cm and 298 K as a function of relative OXD concentration, C_{OXD}. The open circle denotes the drift mobility of holes at 0 wt % OXD. There is little ionization potential difference between PS and OXD molecules. The inset shows the tail broadening of the Gaussian time-of-flight signal, d vs the transit time t_T.

of the transit time in the PS-OXD system. The conventional Gaussian nature of the carrier packet moving through the material shows that the ratio of diffusive spread to displacement is given by, $\Delta x/x=(kT/eE)(2Dt)^{-1/2}$, where D is the carrier diffusion constant. Using the Einstein relation, $D=(kT/e)\mu$, this relation yields a relative standard deviation of the carrier at the transit time,

$$\Delta t_T/t_T=(2kT/eV)^{1/2}. \tag{2}$$

According to the conventional Gaussian model, $\Delta t_T/t_T$ is therefore independent of the transit time. However, the inset of Fig. 1 shows that the tail broadening increases with increasing transit time. A theoretical work[9] suggests that superimposing off-diagonal disorder to the array of energetically ordered hopping sites increases the carrier diffusivity. In the OXD-PS system, the fluctuation of charge transfer rate among hopping sites and the increase in diffusional route due to the mixture of two molecules affect the time-dependent tail-broadening of the Gaussian signals.

Next, we discuss charge transport in polymer matrices doped with two molecules of different ionization potential. If the ionization potential difference between doped molecules is larger than 0.2 eV,[13] the dramatic transition between the Gaussian and featureless dispersive TOF signals was observed as has been reported before.[14] As an example, Fig. 2(a) shows the hole mobility and TOF signals in the PS-DEH mixed doped system at 2.0×10^5 V/cm and 298 K. It is noted from Fig. 2 that at low DEH concentrations, the TOF signal becomes dispersive and the drift mobility of holes decreases with increasing DEH concentration. Since the ionization potential of the DEH molecule is lower than that of the PS molecule, the DEH molecule acts as a trap for holes: carriers occasionally become localized on DEH molecules. At low DEH concentrations, the wave function overlap among DEH molecules is so small that holes localized at DEH molecules are excited thermally to PS molecules for charge transport. The energy distribution of hopping sites in the mixed doped system causes dispersive transport. On the other hand, Fig. 2 shows that at DEH concentrations higher than 10 wt %, the charge transport is determined only by the hopping among DEH molecules and the TOF signal is Gaussian again. At sufficient high DEH concentrations, the overlap among the DEH molecules becomes large, and so that the DEH-DEH hopping begins to compete with the hopping among PS-PS and PS-DEH molecules: the drift mobility depends on the DEH concentration only and the TOF signal becomes the Gaussian type.

Figure 2(b) shows that the activation energy for hole transport at 2.0×10^5 V/cm, Δ, as a function of the relative DEH concentration in the PS and DEH mixed doped system. The temperature dependence of the drift mobility of holes is usually given by the Arrhenius law: $\mu\propto\exp(-\Delta/kT)$. On the other hand, Bässler *et al.*[5] predicted that the temperature dependence of the mobility is given by $\mu\propto\exp[-(T_1/T)^2]$, where T_1 is a constant. However, we cannot distinguish whether T^{-1} or T^{-2} is a better descrip-

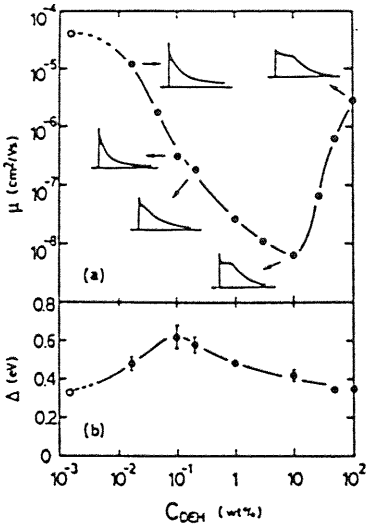

FIG. 2. (a) Hole drift mobility and typical time-of-flight photocurrent pulse shapes in the PS-DEH system at 2.0×10^5 V/cm and 298 K as a function of relative DEH concentration, C_{DEH}. The open circle denotes the drift mobility of holes at 0 wt % DEH. The ionization potential difference between PS and OXD molecules is about 0.2 eV. (b) Activation energy for the hole mobility in the PS-DEH system at 2.0×10^5 V/cm, Δ, as a function of relative DEH concentration, C_{DEH}.

tion. In this work the activation energy is determined by the Arrhenius plot. The activation energy for the mobility characterizes the hopping among molecules. It is seen from Fig. 2 that the activation energy for the hopping among molecules increases at the range of dispersive TOF shape. The activation energy reflects the TOF pulse shape rather than the magnitude of the mobility. In trap-controlled hopping, the charge transport is limited by the hopping from the low-trap state to the high-mobile state. The activation energy characterizes the energy depth of trap states.[15] According to this model, the activation energy of hole mobility in the PS-DEH system Δ_{P-D} is given by

$$\Delta_{P-D}\simeq\Delta_{D-D}+\Delta I_p, \tag{3}$$

where Δ_{D-D} is the activation energy of the hopping among DEH molecules, and ΔI_p is the ionization potential difference between DEH and PS molecules. Since the activation energy Δ_{D-D} is independent of the concentration of DEH molecules in polycarbonate,[10] one expects that in the mixed doped system Δ_{P-D} does not depend on the DEH concentration. However, the experiments show that Δ_{P-D} is very sensitive to the concentration of DEH molecules. We believe that the spatial and energetic fluctuation of hopping sites cause the dispersion of carriers and increase the activation energy for charge transport. If the energetic fluctuation of hopping sites (ΔI_p in this case) is not negligible compared with the activation energy in a polymer doped one molecule, the transition from Gaussian to dispersive TOF signal occurs. The nature of hopping charge transport in MDPs is considered to be clarified by the addition of disorder concept to the conventional trap-controlled[14] or polaron transport models[12].

In summary, we have studied the effect of disorder on diffusion and drift of carriers in a polymer matrix doped with two different molecules. The anomalous tail broadening of Gaussian TOF signal is caused by a wide distribution of hopping rate among molecules. The dramatic transition between Gaussian to dispersive TOF signal is caused by the energetic distribution of hopping sites. A wide distribution of hopping time among molecules due to diagonal and off-diagonal disorder leads to dispersion of transiting charge packet and plays a key role in determining the feature of TOF signals.

[1] G. Pfister and H. Scher, Adv. Phys. 27, 747 (1978).
[2] J. Mort and G. Pfister, *Electronic Properties of Polymers*, edited by J. Mort and G. Pfister (Wiley, New York, 1982), p. 215.
[3] W. G. Gill, J. Appl. Phys. 43, 5033 (1972).
[4] F. C. Bos and D. M. Burland, Phys. Rev. Lett. 58, 152 (1987).
[5] M. A. Abkowitz, M. J. Rice, and M. Stolka, Philos. Mag. B 61, 25 (1990).
[6] H. Bässler, G. Schönherr, M. Abkowitz, and D. M. Pai, Phys. Rev. B 26, 3105 (1982).
[7] M. Stolka, J. F. Yanus, and D. M. Pai, J. Phys. Chem. 88, 4707 (1984).
[8] H. J. Yuh and M. Stolka, Philos. Mag. B 58, 539 (1988).
[9] R. Richert, L. Pautmeier, and H. Bässler, Phys. Rev. Lett. 63, 547 (1989); L. Pautmeier, R. Richert, and H. Bässler, Synth. Met. 37, 271 (1990).
[10] J. X. Mack, L. B. Schein, and A. Peled, Phys. Rev. B 39, 7500 (1989).
[11] Y. Kanemitsu and J. Einami, Appl. Phys. Lett. 57, 673 (1990).
[12] L. B. Schein, D. Glatz, and J. C. Scott, Phys. Rev. Lett. 65, 472 (1990).
[13] If the ionization potential difference is about 0.1 eV (for example, the OX-HD system), the TOF signal is Gaussian over all compositions.
[14] H. J. Yuh, D. Abramsohn, and M. Stolka, Philos. Mag. Lett. 55, 277 (1987).
[15] G. Pfister, S. Grammatica, and J. Mort, Phys. Rev. Lett. 37, 1360 (1976).